AN ABSTRACT OF THE DISSERTATION OF

John J. Osborne V for the degree of Doctor of Philosophy in Oceanography presented on March 12, 2014.

Title: Interactions of Wind-Driven and Tidally-Driven Circulation in the Oregon Coastal Ocean.

Abstract approved:

_____

Alexander L. Kurapov

Influences of tidal and slower (subtidal) oceanic flows over the continental shelf and slope off Oregon are studied using a high-resolution ocean circulation model and comparative model-data analyses. The model is based on the Regional Ocean Modeling System (ROMS), a fully nonlinear, three-dimensional model (using hydrostatic and Boussinesq approximations). The model horizontal resolution is 1 km. The study period is summer 2002.

Variability in the semi-diurnal internal (three-dimensional, baroclinic) tidal flows is influenced by the background conditions associated with coastal wind-driven summer currents. Our analyses reveal areas of intensified semidiurnal tide on the Oregon slope and the shelf and how these vary with change in the background conditions. Hot spots of barotopic-to-baroclinic energy conversion found on the slope occupy 1% of the slope area produce about 20% of the internal tide energy. At these locations, generation is well balanced by radiation of the internal tide energy away from the generation location.

Intensity of the diurnal K1 and O1 tidal currents on the Oregon shelf is also influenced by the background stratification and alongshore currents associated with summer upwelling. Tidal currents are stronger in stratified conditions (as compared to an unstratified case). Intensity of the diurnal surface current is influenced by the advection of the alongshore wind-driven coastal current by cross-shore tidal current and also diurnal wind forcing. Analyses in this part are corroborated by comparisons with the high-frequency (HF) radar surface currents. Diurnal flows may dominate variability around Cape Blanco, a prominent geographical feature on the Oregon coast, where the surface diurnal currents may be in excess of 0.3 m/s.

Analyses of the slope flows using a passive tracer released continuously at the bottom at the 300 m depth show the presence of the continuous undercurrent between Cape Blanco and Heceta Bank. In this area, the Reynolds-averaged term $\langle v'q' \rangle$ is computed, where v' and q' are the high-pass filtered (tidal) velocity across the 200-m isobath and the tracer concentration, respectively, and $\langle \cdot \rangle$ denotes the 40-hour half-amplitude low-pass filter. The Reynolds term contributes appreciably to the on-shelf tracer transport on subtidal scales.

Interactions of Wind-Driven and Tidally-Driven Circulation in the Oregon Coastal Ocean

by
John J. Osborne V

A DISSERTATION

submitted to

Oregon State University

in partial fulfillment of
the requirements for the
degree of

Doctor of Philosophy

Presented March 12, 2014
Commencement June 2014

Doctor of Philosophy dissertation of John J. Osborne V presented on March 12, 2014.

APPROVED:

Major Professor, representing Oceanography

Dean of the College of Earth, Ocean, and Atmospheric Sciences

Dean of the Graduate School

I understand that my dissertation will become part of the permanent collection of Oregon State University libraries. My signature below authorizes release of my dissertation to any reader upon request.

John J. Osborne V, Author

ACKNOWLEDGEMENTS

I am deeply thankful for the guidance given my advisor, Dr. Alexander Kurapov. He has an infectious and relentless enthusiasm for science and I hope that a little has rubbed off on me. I am thankful to my parents, Mom, Dad, Ron, and Rosemary (and my two newest ones, Sue and Bill!), for their unwavering belief in me. I wouldn't have gotten this far without them. My friends have been great supporters, knowing exactly what I am feeling (sometimes because I wouldn't be quiet about it), especially Rob, Matt, and Ashley. Finally, my wife Angela has been with me every step of the way, and I am forever thankful.

CONTRIBUTION OF AUTHORS

Dr. Alexander L. Kurapov was involved in all aspects of the development all chapters. Drs. Gary D. Egbert and P. Michael Kosro were involved in all aspects of the development of Chapters 2, 3, and 4. Additionally, Dr. Kosro provided the NH10 mooring data analyzed in chapter 2 and the high-frequency radar data analyzed in Chapter 3. Dr. John A. Barth assisted in the development of Chapter 3 and 4.

TABLE OF CONTENTS

TABLE OF CONTENTS (Continued)

Page

LIST OF FIGURES

LIST OF FIGURES (Continued)

Figure Page

LIST OF FIGURES (Continued)

LIST OF FIGURES (Continued)

Figure Page

LIST OF FIGURES (Continued)

Figure Page

LIST OF TABLES

Interactions of Wind-Driven and Tidally-Driven Circulation in the Oregon Coastal Ocean

1. Introduction

Internal tide circulation is important for several reasons. On a global scale, internal tides (e.g., Baines 1982) may contribute a large portion of the energy necessary to mix the ocean and maintain meridional overturning circulation, as suggested by Munk and Wunsch (1998) and subsequently investigated from theoretical, observational, and numerical modeling perspectives (e.g., Egbert and Ray 2000, Niwa and Hibiya 2001, Merrifield and Holloway 2002, Althaus et al. 2003, St. Laurent et al. 2003, Llewellyn Smith and Young 2001, 2003, Simmons et al. 2004, Di Lorenzo et al. 2006). In coastal environments, internal tides increase spatial and temporal variability in currents, impacting transport, mixing, and biological productivity, seen in both observations (e.g., Hayes and Halpern 1976, Torgrimson and Hickey 1979, Petruncio et al. 1998,) and models (e.g., Cummins and Oey 1997, Kurapov et al. 2003). Other processes, occurring on different spatio-temporal scales (e.g., coastal upwelling, jet separation, eddy formation and propagation, and undercurrents) alter the background hydrographic structure internal tides propagate through, varying internal tide generation and propagation. Historically, observations of the coastal ocean are too sparse in space and time to resolve internal tides over the entire slope and shelf at more than a few latitudes for more than a few days, making it difficult to understand how internal tides influence and/or are altered by other coastal ocean phenomena. This leaves many unresolved questions: Are internal tides

predictable, and if so, to what degree (e.g., seasonally? Daily?) How sensitive are internal tides to up- and downwelling variability in the wind? Does the internal tide significantly impact cross-shelf undercurrent transport? In what ways is mixing on the shelf impacted by internal tides?

Modern numerical models offer a practical approach to investigating internal tides in the coastal ocean, as recent developments in turbulence parameterizations are able to describe both wind-driven (e.g., Allen et al. 1995, Federiuk and Allen 1995, Oke et al. 2002c) and tidally-driven circulation (e.g., Cummins and Oey 1997, Merrifield and Holloway 2002, Pereira et al. 2002). Numerical models have been successfully used to describe transport in the coastal ocean and also to offer dynamical insight on circulation. However, many modeling studies have focused on either wind-driven circulation or tidally-driven circulation alone, with few studies combining the dynamics of both. Given the questions above, a wide-open research field is present.

Here, the Regional Ocean Modeling System (ROMS; Shchepetkin and McWilliams 2005) is used to study interactions of tidal and subinertial circulation in the Oregon coastal ocean during summer 2002. Summer 2002 is picked as it was extensively observed via the GLOBEC project (Batchelder 2002), giving a large data set for model validation and process comparison. In chapter 2, the M2 (12.42 hour period) internal tide is modeled in combination with wind-driven upwelling circulation. Only one tidal constituent is forced in this initial work as multiple constituents would make it difficult to separate their effects. The M2 constituent is used because it is the strongest constituent over the slope region. Areas of internal

tide generation and propagation are mapped, but no connections with 3-5 day variability in winds are found.

In chapter 3, previous claims by Erofeeva et al. (2003) of strong diurnal tides (approximately 24 hour period) over the wide portion of the Oregon shelf (43.9°N-44.5°N) are confirmed via high-frequency radar. They are also investigated using the ROMS model, now forced with 8 tidal constituents (4 semi-diurnal and 4 diurnal). The ROMS model solution qualitatively agrees with Erofeeva et al. (2003) and the observations. It also reveals relatively strong tides near Cape Blanco (42.8°N). The strong diurnal tides at these two locations are partially explained as coastal trapped waves at diurnal frequency, which are also found to be sensitive to stratification and topography, and also cross-shore tidal excursion of the wind-driven along-shore jet.

In chapter 4, tidal effects on cross-shelf transport of the California Undercurrent (CUC, e.g., Hickey 1979) are investigated. This investigation is done by releasing a passive tracer in two models, one forced with the tide and wind, and one forced by winds alone. More tracer, and ostensibly CUC water, is brought on-shore in the tide and wind forced case. Using a Reynolds decomposition, the tide is found to significantly contribute to on-shelf tracer flux.

2. Spatial and temporal variability of the M2 internal tide generation and propagation on the Oregon shelf

J. J. Osborne, A. L. Kurapov, G. D. Egbert and P. M. Kosro

Journal of Physical Oceanography

45 Beacon Street

Boston, MA 02108-3693

November 2011

2.1 Abstract

A 1-km horizontal resolution model based on the Regional Ocean Modeling System is implemented along the Oregon coast to study average characteristics and intermittency of the M2 internal tide during summer upwelling. Wind-driven and tidally-driven flows are simulated in combination, using realistic bathymetry, atmospheric forcing and boundary conditions. The study period is April through August 2002, when mooring velocities are available for comparison. Modeled subtidal and tidal variability on the shelf are in good quantitative agreement with moored velocity time series observations. Depth-integrated baroclinic tidal energy flux (EF), its divergence, and topographic energy conversion (TEC) from the barotropic to baroclinic tide are computed from high-pass filtered, harmonically analyzed model results in a series of 16-day time windows. Model results reveal several “hotspots” of intensive TEC on the slope. At these locations, TEC is well balanced by EF divergence. Changes in background stratification and currents associated with wind-driven upwelling and downwelling do not appreciably affect TEC hotspot locations, but may affect intensity of internal tide generation at those locations. Relatively little internal tide is generated on the shelf. Areas of supercritical slope near the shelf break partially reflect baroclinic tidal energy to deeper water, contributing to spatial variability in seasonally-averaged on-shelf EF. Despite significant temporal and spatial variability in the internal tide, the alongshore-integrated flux of internal tide energy onto the Oregon shelf, where it is dissipated, does not vary much with time. Approximately 65% of the M2 baroclinic tidal energy

generated on the slope is dissipated there and the rest is radiated toward the shelf and interior ocean in roughly equal proportions. An experiment with smoother bathymetry reveals that slope-integrated TEC is more sensitive to bathymetric roughness than on-shelf EF.

2.2 Introduction

In summer, currents over the Oregon shelf (U.S. west coast) are predominantly wind-driven, varying on the temporal scale of several days. The wind-driven alongshore current is predominantly to the south, is vertically sheared, and is associated with upwelling of cold waters near the coast (Allen et al. 1995). At the surface, summer-average magnitude of the wind-driven jet is near 0.5 m s^{-1}. Tides are relatively moderate. The dominant barotropic tidal constituent off Oregon is M2 . Although the M2 tidal depth-averaged currents are rather small, less than 0.05 m s^{-1} (Erofeeva et al. 2003), they flow over variable bathymetry and generate vertical baroclinic motions near the M2 tidal period (12.4 h; Baines 1982), resulting in an internal tide that can be 0.1-0.15 m s^{-1}, based on mooring observations (Hayes and Halpern 1976; Torgrimson and Hickey 1979; Erofeeva et al. 2003). The internal tide thus can be an important contributor to current variability at the surface. Near the bottom, where the wind-driven current is weaker, internal tide currents can potentially dominate.

The characteristic horizontal length scale of the M2 internal tide over the shelf is *O*(10 km). Internal tide generation and propagation are sensitive to variability in background currents and hydrographic conditions associated with wind-driven

upwelling and mesoscale eddies (Mooers 1970, 1975a,b; Chavanne et al. 2010; Chen et al. 2003; Park and Watts 2006; Pereira et al. 2007; Hall and Davies 2007; Xing and Davies 1997, 1998, 2005, see Kurapov et al. (2010) for a brief review). In particular, Xing and Davies (1997), using an idealized model, demonstrated that background changes associated with upwelling can increase the transfer of tidal energy to higher harmonics. Xing and Davies (2005) showed that a cold water dome can trap energy of propagating internal waves. Observations available in the coastal area are generally too sparse to resolve the resulting spatial and temporal intermittency of the internal tide. To describe this variability, provide estimates of the M2 tidal energetics on the slope and shelf, and ultimately understand how the wind-driven and tidal flows influence each other, high-resolution model simulations seem to be the most promising approach.

In modeling studies off Oregon, wind-driven currents and internal tides have traditionally been studied separately (e.g., Kurapov et al. 2003; Allen et al. 1995; Federiuk and Allen 1995; Kurapov et al. 2005; Oke et al. 2002b,a; Springer et al. 2009; Koch et al. 2010). Recently, Kurapov et al. (2010) used the hydrostatic Regional Ocean Modeling System (ROMS; www.myroms.org) to study influences of the wind-driven upwelling and internal tide in an idealized, two-dimensional (2D, cross-shore and vertical coordinates) set-up. They found that internal tides with magnitudes comparable to those measured off Oregon affect subtidal cross-shore and along-shore transports. The utility of this 2D approach is limited, however, as the M2 internal tidal motions are superinertial and freely propagate in three dimensions.

Besides, the 2D approach may provide a misleading picture since internal tides in such a model are only generated by the cross-shore barotropic tidal current flowing up and down the continental slope. In fact, off Oregon and in many other coastal environments, the M2 barotropic tide propagates as a shelf-modified Kelvin wave, in which the M2 tidal current is strongly polarized and aligned with the continental slope bathymetry. Alongshore small-scale bathymetric variations can thus be important for internal tide generation, potentially resulting in an internal tide of greatly varying intensity along the coast.

In this chapter, we analyze the output of a 3D model (described in section 2.3) that realistically represents both wind-driven and M2 tidal flows over the Oregon shelf and slope (as verified against observations in section 2.4). We demonstrate strong non-uniformity of the M2 internal tide generation along the Oregon slope and describe its intermittency (section 2.5). Some effects of bathymetry on model estimates of internal tide generation and on-shelf propagation are discussed in section 2.6. Section 2.7 provides a summary.

2.3 Model Description

We use the Regional Ocean Modeling System (ROMS), a free-surface, hydrostatic, Boussinesq, terrain-following primitive equation model featuring advanced numerics (Shchepetkin and McWilliams 2005). The model domain is approximately 300 km by 540 km (Figure 2.1). The study period is April 1 through August 31, 2002. A thoroughly verified model solution of subtidal circulation off Oregon is available

during the same period of time (Koch et al. 2010). It provides boundary conditions for our higher-resolution study. Data from the Global Ocean Ecosystem Dynamics (GLOBEC) field study (Batchelder et al. 2002) are available during this period, including mooring velocity profile measurements on the shelf. Note that internal tides on the Oregon shelf are generally stronger during summer than winter (Erofeeva et al. 2003) since the winter waters are well-mixed due to seasonal downwelling and storms.

The model horizontal resolution is approximately 1 km. Forty terrain-following *s*-layers are used in the vertical, with an emphasis on resolving the surface and bottom boundary layers (using ROMS terminology, $\theta_s = 5$, $\theta_b = 0.4$, thermocline = 50 m). Subgrid-scale turbulence is handled using the Mellor-Yamada 2.5 scheme (Mellor and Yamada 1982) modified by Galperin et al. (1988). The horizontal eddy diffusion and viscosity coefficients are set to 2 $m^2 s^{-1}$ in the interior and increase over a 40-km sponge layer (via a sinusoidal ramp) to 15 $m^2 s^{-1}$ at the three open boundaries. Bathymetry is a combination of the 5' resolution ETOPO5 (NOAA 1988) and the higher-resolution 12" NOAA-National Geophysical Data Center bathymetry datasets. To investigate the effects of bathymetric resolution on internal tide energetics, cases using different degrees of bathymetric smoothing (Figures 2.1a,b) have been considered. Smoothing is performed solving a pseudo-heat equation with fixed values along the boundaries to preserve the shape of the coastline (Bennett 1992, Chapter 2). The minimum depth is set to 10 m along the coast. Unless specifically mentioned, results for the case with rougher bathymetry are presented.

Subtidal boundary values (free surface elevation, velocities, temperature and salinity) are obtained by interpolation between snapshots from a larger scale, 3-km horizontal resolution ROMS simulation forced by winds and heat fluxes, but not tides (Koch et al. 2010). These boundary fields are provided every 48 hours. Initial conditions are obtained from the same model. Flather (1976) and Chapman (1985) boundary conditions are used for normal barotropic velocities and the free surface, respectively. Passive/active radiation boundary conditions are applied for baroclinic velocities, temperature and salinity (Marchesiello et al. 2001). Tidal forcing is added to the subtidal boundary conditions every time step using M2 harmonic constant estimates of sea surface elevation amplitude and depth-averaged currents from a data-assimilating 1/30◦-resolution barotropic tidal model (Egbert et al. 1994; Egbert and Erofeeva 2002). While this adds barotropic tides to the boundary (which then propagate into the domain), data for internal tides at the boundary are unavailable and their omission is a potential source of error. To simplify analysis, only the dominant M2 tidal constituent is included in tidal forcing. Atmospheric momentum and heat flux are computed using the bulk flux formulation adapted in ROMS (Fairall et al. 1996a,b). The daily-averaged wind speed is obtained from the Coupled Ocean/Atmosphere Mesoscale Prediction System (COAMPS; Hodur 1997) and inputs for heat flux computations (air temperature and pressure, relative humidity and solar short-wave radiation; all monthly-averaged) from the National Centers for Environmental Prediction reanalysis (NCEP; Kalnay et al. 1996). The meridional wind stress is well-correlated along the Oregon coast, e.g., as can be seen in the time series at two midshelf locations near 44.7°N and 42.4°N (near the NH10 and Rogue

River moorings, described below; Figure 2.3). The wind stress is substantially stronger south of Cape Blanco (42.8°N) due to orographic effects (Samelson et al. 2002).

2.4 Model Verification

We first verify the accuracy of the subinertial wind-driven circulation and the tidally-forced flows. To separate subinertial (mostly wind-driven) and superinertial (mostly tidal) variability for this analysis, a 40-hour half-amplitude low-pass filter is applied to both observed and modeled time series. To describe tidal intermittency, high-pass filtered time series are harmonically analyzed in a series of relatively short overlapping time windows. In each window, the high-pass filtered signal is assumed to be harmonic, e.g., $u(x,y,z,t) = \mathrm{Re}[\tilde{u}(x,y,z)e^{i\omega t}]$, where ω is the M2 angular frequency (1.405×10^{-3} rad s^{-1}) and $\tilde{u}$ is a complex harmonic constant. In our case, the windows are chosen to be 16 days long to allow separation of the M2 and S2 tidal constituents in the data and thus facilitate model-data comparisons. Also, for the purposes of this study, we define barotropic current as depth-averaged current and baroclinic current as the deviation from the depth average. Note that separation of the flow into barotropic and baroclinic components over varying bathymetry is not trivial. For instance, the bottom boundary layer would introduce vertical variability in barotropic tidal flows. Variability in the bottom boundary layer associated with wind-driven processes can introduce some intermittency in estimates of barotropic (depth-averaged) tidal currents. The definition adopted here allows clear separation of

equations for the barotropic and baroclinic tidal energy, but is not without shortcomings (see Kurapov et al. (2003) for further details).

2.4.1 *Wind-driven Circulation*

Maps of monthly-averaged SST from the 5.5-km resolution Geostationary Operational Environmental Satellite (GOES; Maturi et al. 2008), the 1-km model solution, and the 3- km solution that provided subtidal boundary conditions are compared in Figure 2.2. In both models, the geometry of the SST front is approximately correct, in particular, the location of the coastal jets separated from the coast near 45°N and 42°N in July and August.

To verify the accuracy of the alongshore shelf currents, we utilize Acoustic Doppler Current Profiler (ADCP) velocity data at three mid-shelf locations on the Oregon shelf (NH10, 124.31°W, 44.66°N, Kosro, 2003; Coos Bay, 124.57°W, 43.16°N, Hickey et al., 2009; Rogue River, 124.57°W, 42.44°N, Ramp and Bahr, 2008). The depths of these three moorings are 81 m, 100 m and 76 m, respectively, and their locations are shown in Figures 1 and 2. Time series of depth-averaged, 40-hour low-pass-filtered meridional velocities at each location are shown in Figure 2.3b-d, including observed velocities (solid black) and model velocities from the smoother (solid half-tone) and rougher (dashed half-tone) bathymetry solutions. Table 2.1 shows the mean and standard deviation of each time series as well as model-data root mean square difference, complex correlation amplitude CC and complex phase angle α (Kundu 1976):

$$\mathrm{CC} = \frac{\langle w_1^*(t) w_2^*(t) \rangle}{\langle w_1^*(t) w_1\ (t) \rangle^{1/2} \langle w_2^*(t) w_2\ (t) \rangle^{1/2}}$$

$$= |\mathrm{CC}| e^{i\alpha}$$

Here, $w_k(t) = u_k(t) + iv_k(t)$; *u* and *v* denote zonal and meridional velocity components, respectively, and $\langle \cdot \rangle$ denotes time-averaging. To compute correlations, time-averaged values are subtracted. The phase angle is a measure of the average veering between the two vector time series. Based on these comparisons, both models reproduce velocity variability on temporal scales of several days and longer qualitatively correctly at all three locations. One aspect of the observed flow at the Rogue River site, south of Cape Blanco, is large-amplitude variability on time scales of 3 to 5 days, particularly during the first half of the study period (see Figure 3d). This is not reproduced in the 1-km model runs, nor is it reproduced in the 3-km model used to provide subtidal boundary conditions. Koch et al. (2010) note that this variability may be due to remote forcing south of the 3-km model domain (40.6°N). Model-data discrepancies over days 210-230 (Coos Bay, Figure 3c) and 185-210 (Rogue River, Figure 3d) can be associated with large-scale eddies in the adjacent interior ocean affecting the offshore displacement of the upwelling front.

2.4.2 *Tidally-forced flows*

To ensure that the forcing of baroclinic flow is correct, barotropic tides from the three- dimensional 1-km model are compared to the solution from the shallow-water tidal model used to provide boundary conditions. The M2 sea surface elevation tidal

amplitude and phase in both models are consistent over the entire 1-km model domain (Figure 2.4a,b). The barotropic M2 tide propagates from south to north along the coast as a shelf-modified Kelvin wave. It takes approximately 1 hour for the barotropic M2 tide to propagate along the Oregon coast. The sea surface elevation amplitude increases from about 0.6 m in the south to 0.85 m in the north. Figure 2.4c shows a close-up of the amplitude and phase map over a part of the shelf region and also includes barotropic tidal current ellipses. Here, and throughout the entire chapter, shaded (clear) ellipses indicate counterclockwise (clockwise) rotation. In the deep water, the tidal current ellipses are strongly polarized and roughly parallel to the coast, with a maximum current velocity of about 0.05 m s^{-1}. Over the slope and shelf (defined here as areas shallower that 200 m, see black contour in the figure), the current ellipses can cross isobaths. In particular, the barotropic current flows over the southern flank of Heceta Bank (43.8°N), suggesting this might be an area of intensified internal tide generation.

Next, we verify the accuracy of the modeled baroclinic M2 internal tide. A point-by-point match between observed and modeled internal tide phase and amplitude can be hard to achieve because of the short horizontal scales associated with internal waves and sensitivity to many model aspects. Here, we are primarily interested in whether modeled internal tide current amplitudes and vertical structures are comparable to the observations on average over the season. For the 2002 study period, 1-hour temporal resolution velocity profiles, suitable for tidal analysis, are available from the NH10, Coos Bay and Rogue River moorings. To provide additional evidence about baroclinic tidal variability, we will also use ADCP data

from the 2001 Coastal Ocean Advances in Shelf Transport (COAST; Boyd et al. 2002) field program. Data are not available at distances of 10 - 20 m from the surface and the bottom due to ADCP limitations. For consistency with the observations, model currents are sampled at the same depths and the barotropic velocity is computed as the average over these depths. Tidal harmonic constants are estimated in a series of overlapping 16-day windows offset by four days and results are presented as horizontal baroclinic tidal current ellipses (Figures 2.5, 2.7, 2.9 and 2.11). The upward (rightward) direction in the plots corresponds to the northward (eastward) velocity direction; the line from an ellipse center shows velocity direction at zero phase.

At NH10 (Figure 2.5), observed and modeled horizontal baroclinic tidal ellipses are plotted every four meters in the vertical, at every other observation depth. Barotropic currents are plotted at the top of each panel. They vary in time, but not as much as baroclinic currents. Means and standard deviations of modeled and observed barotropic tidal flow are similar (Table 2.2). First mode baroclinic structure is apparent in both the observations (Figure 2.5, top) and the model (Figure 2.5, bottom), with relatively larger currents and opposite phases near surface and bottom. The largest observed (modeled) baroclinic current is 0.10 m s^{-1} (0.06 m s^{-1}). Both the modeled and observed series exhibit similar intermittency. There could be several reasons for our model estimates of baroclinic tides to be smaller than those observed. For instance, observed current variability in the tidal frequency band may be partially driven by high-frequency atmospheric forcing, which was filtered in the model

forcing. Also, the model does not account for the internal tide possibly propagating into our domain.

To further investigate the strength of the baroclinic tide near NH10, a series of surface maps of model baroclinic tidal current ellipses are shown in Figure 2.6. For clarity, the ellipses are plotted every 4 km. The black diamond symbol near the center of each panel marks the NH10 mooring. The time period analyzed (days 189-237) corresponds to a period of intensified observed internal tide at NH10 (cf. Figure 2.5). During this time period, a region of intensified baroclinic surface tide (with surface current amplitudes > 0.10 m s^{-1}) is found in the model at distances of only 4–10 km north and west of NH10. It is possible that small changes in bathymetry or other model details could bring the area of the intensified internal tide closer to the NH10 location.

To see if the internal tide in the region of intensification is similar to observations at NH10, baroclinic tidal ellipses from a location ten kilometers north of NH10 (marked with a star in Figure 6e) are shown in Figure 7. The depth of this location (83 m) is close to that of NH10 (81 m). During days 200-240, both modeled and observed baroclinic currents show first mode structure with tidal velocities of similar magnitude, roughly 0.10 m s^{-1}. Overall, we conclude that the model solution produces internal tide currents in the NH10 region at magnitudes similar to those observed at the mooring (up to 0.10 m s−1), though not necessarily at the same time.

Analysis of tidal currents at the Coos Bay mooring leads to similar conclusions about the strength of internal tides on the Oregon shelf. In Figure 2.8, horizontal tidal ellipses at the Coos Bay mooring are plotted every six meters in the

vertical, one-third the observed resolution. Observed and modeled depth-averaged currents are similar (Table 2). The largest observed (0.12 m s^{-1}) and modeled (0.10 m s^{-1}) internal tide currents are also similar. First mode baroclinic structure is apparent.

Observed and modeled baroclinic tidal ellipses at the Rogue River mooring location are shown in Figure 2.9. Ellipses are plotted every four meters in the vertical, at the observed resolution. Modeled M2 internal tide currents (maximum amplitude of 0.06 m s^{-1}) are also generally a bit stronger than observed (maximum amplitude of 0.04 m s^{-1}), though both are weak compared to barotropic currents (Table 2). Figure 2.10 shows model baroclinic surface tidal current ellipses in the region around the Rogue River mooring. The mooring location, marked with a black diamond symbol, is in a region of generally weak surface baroclinic M2 tides, while regions of stronger baroclinic tide activity (with currents > 0.10 m s^{-1}) are found to the north and south. Explanations for this pattern are given later, in section 2.6a.

To develop better understanding of internal tide energetics in the area, we also provide additional analysis of mooring observations from the 2001 COAST experiment (Boyd et al. 2002, Figure 2.11). Mooring locations are shown in Figure 2.6 as black diamonds along 45°N. At the shallowest and mid-depth moorings, observed currents are predominately first mode and surface-intensified, reaching 0.15 m s^{-1}. At the deepest mooring, first mode structure is occasionally observed. Measured currents reach 0.10 m s^{-1} at that location. While background conditions in 2001 and 2002 are likely different, this additional data does provide further evidence that M2 internal tide currents with magnitudes above 0.10 m s^{-1} are not uncommon on the Oregon shelf.

Based on these comparisons, we conclude that the magnitude and variability of the modeled internal tide are qualitatively similar to the observed internal tide. At the same time, the exact timing and location of areas of intensified internal tide are difficult to predict. Further, conclusions about the strength and variability of the M2 internal tide in a given area based on data from a single mooring may be inaccurate. For a rigorous, point-by-point analysis of the internal tide, a large number of observations are needed over both the shelf and slope. Analysis of high-frequency radar surface currents (O'Keefe 2005; Kurapov et al. 2003) may provide additional insights and is planned for the future.

2.5 Baroclinic M2 Tide Energetics

2.5.1 *Stable and Intermittent Features of M2 Internal Tide Energetics*

In the description below, barotropic (depth-averaged) quantities are given subscript 1 and baroclinic quantities subscript 2. Based on the linear theory (Kurapov et al. 2003), the depth-integrated, tidally-averaged energy balance for the harmonically-varying ocean is approximately

$$\mathrm{TEC} \approx \boldsymbol{\nabla} \cdot \mathbf{EF} + \mathrm{Residual} \tag{1}$$

where

$$\mathrm{TEC} = \frac{1}{2}\mathrm{Re}\{\tilde{p}_2^*|_{z=-h}\tilde{w}_1\} \text{ and} \tag{2}$$

$$= \frac{1}{2}\mathrm{Re}\{\tilde{p}_2^*|_{z=-h}\tilde{\mathbf{u}}_1\} \cdot \nabla h \tag{3}$$

is the topographic conversion of barotropic to baroclinic tidal energy and

$$\mathbf{EF} = \frac{1}{2}\int_{-h}^{0} \mathrm{Re}\{\tilde{\mathbf{u}}_2\, \tilde{p}_2^*\}\, dz$$

is the depth-integrated baroclinic tidal energy flux (**EF**) vector. In (2) - (4), the tilde denotes complex harmonic constants, the asterisk complex conjugates, $w_1 = \mathbf{u}_1 \cdot \nabla h$ is the bottom vertical velocity associated with barotropic tidal flow over bathymetry, $\mathbf{u}_1 = (u_1, v_1)$ is the depth-averaged horizontal current vector, $h(x,y)$ bottom topography, and p_2 baroclinic tidal pressure, computed as the deviation from the depth-averaged pressure associated with tidal motions. The residual term accounts for the effects of bottom friction, eddy dissipation throughout the water column, and nonlinear advection effects. In our study, it is not directly computed, but rather estimated as TEC $-\nabla \bullet$ **EF**.

Tidal harmonic constant estimates of $\tilde{u}$, $\tilde{v}$, and $\tilde{p}$ are obtained in 16-day time windows offset by 4 days, resulting in 34-point (148-day) time series of **EF** and TEC at each horizontal location. To provide an illustration of M2 internal tide intermittency, EF vectors are shown over a portion of the Oregon shelf from three partially overlapping time windows, yeardays 193–225 (Figure 2.12). The onshore flux near 45°N increases over this period. The rectangle shown in each panel of Figure 12 marks the computational domain in Kurapov et al. (2003). In that study, the M2 internal tide was modeled using a linear baroclinic model and variational assimilation of high frequency radar surface currents, with correction of baroclinic tidal fluxes along the open boundary. Both studies find that the M2 baroclinic tidal energy flux into the smaller domain is from the northwest on average and is $O(10\ \mathrm{W\ m^{-1}})$. Note that internal tides in the 2003 study were driven by the assimilated

data, and the sources of the internal tide propagating into this area were unknown. Here we can identify the sources within our larger study area.

Stable features and intermittency in **EF**, TEC, $\nabla \bullet$ **EF**, and the residual are described next using their time-mean and standard deviation maps. Over the slope, the magnitude of the depth-integrated M2 baroclinic energy flux is $O(100\ \mathrm{W\ m^{-1}})$ (Figure 2.13a, vectors shown every 6 km). Zones of strong EF divergence are apparent. At (124.75°W, 42.6°N), in the area near Cape Blanco, the EF magnitude approaches 700 W $\mathrm{m^{-1}}$.

To better see small **EF** vectors over the shelf (h < 200 m), the scale in Figure 2.13b is adjusted and vectors are shown every 4 km. At the shelf break (h = 200 m), the time-averaged **EF** is directed onshore everywhere, reaching 40-60 W $\mathrm{m^{-1}}$ in some places and decreasing toward the coast. Areas of relatively larger onshore EF occur near Cape Blanco (42.8°–43°N), along the southern flank of Heceta Bank (43.5°–44°N) and over a wider shelf portion north of 45.2°N. The shelf between 44.2°–45°N, studied by Kurapov et al. (2003), turns out to be an area of relatively weak onshore **EF**. **EF** standard deviation ellipses over the shelf are shown at 8-km resolution (Figure 2.13c). They are polarized, showing maximum variability in the direction of the mean flux. Standard deviation maxima are close to the mean values at the corresponding locations, indicating that the baroclinic tidal flux (mean ± standard deviation) is mostly onshore. We also find that EF over the shelf is weak within about 20 km of the Rogue River mooring (42.44°N), but is much stronger north and south of this shadow zone, similar to the pattern of baroclinic surface tides in Figure 2.10.

The map of seasonally-averaged TEC (Figure 2.14a; colorbar limits set at ±0.04 W m^{-2}) reveals a few hotspots of strong positive TEC. Several small areas of relatively weak negative TEC can also be seen. Formally, this implies that energy is transferred from baroclinic to barotropic tides, although areas of negative TEC may also reflect the difficulty in choosing appropriate definitions of barotropic and baroclinic motions (see Kurapov et al. 2003). Contrary to our expectations, the area south of Heceta Bank (43.8°N), where bathymetry is nearly perpendicular to the general direction of barotropic tide propagation (cf. Figure 2.4), is not the largest hotspot of TEC. Comparison of Figures 2.14a and 2.13a suggests that the increased onshore **EF** in that area is partially due to the **EF** propagation from the hotspot at 44.4°N, going around the southern flank of Heceta Bank.

To estimate the contribution of the few TEC hotspots to the total TEC, we compute $P_{\mathrm{TEC}}(v)$, the proportion of the total area-integrated TEC generated by grid points with 0 < TEC < v. The total TEC is determined by integration over the area of Figure 2.14a, with negative TEC spots excluded. More formally,

$$\overline{\mathrm{TEC}}(v) = \int_{A(v)} \mathbf{TEC}(\boldsymbol{x})\, dA$$

where $A(v) = \{\mathbf{x} = (x, y) | 0 < \mathrm{TEC}(\mathbf{x}) < v\}$, and

$$P_{\mathrm{TEC}}(v) = \frac{\overline{\mathrm{TEC}}(v)}{\overline{\mathrm{TEC}}(\infty)} \qquad (5)$$

We find that the hotspots with values greater than 0.04 W m^{-2} contribute approximately 20% of the total TEC (Figure 2.15). Interestingly, the combined area of grid cells with TEC≥0.04 W m^{-2} is only 1.2% of the area of the continental

slope (200 < h < 1800 m). At the same time, about 50% of total TEC is provided by low energy areas with mean values between 0 and 0.015 W m^{-2}. In Figure 2.14b, colorbar limits are adjusted to ±0.01 W m^{-2} to emphasize these lower TEC areas. TEC is still patchy, and even at this adjusted scale, it is concentrated over selected portions of the slope, with very little baroclinic tidal energy generated over the shelf. TEC standard deviation (Figure 2.14c) is also largest over the slope, although its magnitude is generally smaller than the mean. Areas of large TEC standard deviation over the slope are typically associated with large mean values.

To provide further insight about what contributes to spatial variability of TEC, we examine the factors in (2), namely the time-averaged amplitudes of barotropic tidal vertical velocity at the bottom $\widetilde{w}_1$ and (Figure 2.16a) and the bottom baroclinic tidal pressure, $\tilde{p}_2 \mid_{z=-h}$ (Figure 2.16b). Both factors are elevated at TEC hotspots (contoured in gray at 0.02 W m^{-2}). The bottom vertical velocity is affected by fine-scale bathymetric variations and exhibits spatial variability on smaller scales than the bottom baroclinic pressure. The latter can be associated not only with generation, but also with propagation of the internal waves. The horizontal wave lengths on the slope are generally larger than the scales of bathymetric variations resolved by the 1-km model, yielding a smoother baroclinic pressure amplitude field. In particular, the amplitude of $\tilde{p}_2 \mid_{z=-h}$ is elevated in the area west and south of Heceta Bank (43.6–44.5°N), consistent with the average path of the internal wave energy propagation (see Figure 2.13a).

Maps of M2 baroclinic energy flux divergence ($\nabla \cdot \mathbf{EF}$; Figure 2.17) are analyzed in similar ways. Time-averaged $\nabla \cdot \mathbf{EF}$ has a few hotspots over the slope (Figure 2.17a), typically collocated with the TEC hotspots. At the adjusted scale (Figure 2.17b), areas of large divergence on the slope coincide with areas of large TEC (Figure 2.14b). The adjusted scale also reveals areas of energy flux convergence (negative divergence), found both over the slope and shelf, which can be associated with internal tide dissipation.

The residual TEC $- \nabla \cdot \mathbf{EF}$, which we would like to interpret as dissipation, is predominately positive. Maps of the season-averaged residual (Figure 2.18a) reveal that the TEC hotspots (with their edges shown as white contours at the 0.02 W m^{-2} level) are well balanced by $\nabla \cdot$ EF. The map at the adjusted color scale (Figure 2.18b) shows vast areas of increased residual over the slope and some over the shelf.

2.5.2 *Reasons for Internal Tide Intermittency*

Internal tide intermittency can result from a number of local and remote factors, including focusing of internal tide rays in a non-uniform medium (Chavanne et al. 2010), variability in TEC associated with changes in stratification around the hotspots (Kurapov et al. 2010) and constructive/destructive interference of remotely generated internal waves (Kelly and Nash 2010). Chavanne et al. (2010) used a ray tracing technique to consider internal wave energy propagation from an underwater ridge in the Hawaiian archipelago and found that a mesoscale eddy can create zones of ray focusing, resulting in areas of larger internal tide signal near the surface. Without a doubt, variability in background conditions affects internal wave propagation in our

study area. However, in our case, not only internal tide propagation, but also generation varies with time. Since along the Oregon coast major TEC hotspots are located in close proximity, it is hard to interpret whether changes in TEC over a given spot are due to local changes in stratification or remote influence of nearby spots. This remote influence (constructive interference mentioned above, see Kelly and Nash (2010)) can be explained using (2). While w_1 and is determined by the local topography and barotropic tide and is relatively steady, near-bottom p_2 can be influenced by both local generation processes and the baroclinic waves propagating into the area (e.g., from neighboring hotspots). The incoming wave can modify the phase and amplitude of p_2 such that the product $\widetilde{w}_1^* p_2$ becomes smaller or larger.

Additional analysis in smaller areas shows that the range of change of TEC can be comparable to the change in the onshore **EF** in the vicinity. However, it would not be the only factor determining the amount of onshore **EF**. For illustration, Figure 2.19a,b shows maps of **EF** and the near-bottom p_2 amplitude in the area south of Heceta Bank in two windows, centered on days 193 and 230. Figure 2.20 shows the time series of TEC and residual integrated over the slope area (bounded by the edges of the map in Figure 2.19 and the 200-m isobath), as well as the integrated EF across the 200-m isobath and the net EF through the southern, western, and northern boundaries of this small area. Values corresponding to the selected time windows are marked with circles. The first (second) time window selected in Figure 2.19 corresponds to a relatively smaller (larger) onshore **EF**. The onshore **EF** is increased by 2.5 MW between days 193 and 230. This increase is comparable to that in TEC over the same period. A change in the strength of the internal tide is also clearly seen

in surface horizontal baroclinic tidal ellipses (Figure 2.19c,d). Figure 2.19a,b suggests that the influence of the hot spot at 44.3°N on p_2 south of Heceta Bank (43.7°N) is smaller in the first time window, 185-201, than the second window, 221-237. Remarkably, the residual (dissipation) in the pictured area increases sharply after day 200 (by more than 5 MW), while the net outward **EF** through the outer boundaries is reduced during the same period. So, despite TEC and onshore **EF** changing by similar amounts over days 193-230, we cannot claim that local increases in internal tide generation are solely responsible for the increase in the onshore **EF**. Influences of remotely generated internal tide complicate analysis of tidal intermittency, making it difficult to establish a definitive relationship with wind-driven conditions.

2.6 Bathymetric Effects on M2 Internal Tide Energy Fluxes

2.6.1 *Bathymetry Criticality*

Internal wave energy propagates along wave characteristics (Wunsch 1975; Baines 1982). The angle φ that a characteristic makes with the horizontal is determined by

$$\tan\varphi = (\omega^2 - f^2)^{1/2}(N^2 - \omega^2)^{-1/2}$$

where ω is the tidal frequency, f the inertial frequency and N the buoyancy frequency. Internal wave beams incident on a supercritical slope (where the bottom slope $\nabla h = \tan\theta$ is steeper than the characteristic slope, $\tan\varphi$) reflect towards deeper water, while those incident on subcritical bathymetry ($\tan\theta < \tan\varphi$) will propagate into shallower water.

To calculate φ, the buoyancy frequency is estimated 20 m above the ocean floor using density profiles computed from temperature and salinity averaged over the entire model run. Figure 2.21 shows a map of the angle difference $\theta - \varphi$. On the offshore side of the 200-m isobath, bathymetry varies from subcritical ($\theta - \varphi < 0$; blue) to near-critical ($\theta - \varphi \approx 0$; green) and supercritical ($\theta - \varphi > 0$; red). Seasonally-averaged **EF** vectors across the 200-m isobath are also plotted in Figure 2.21, repeated from Figure 2.13. Sections with relatively larger onshore baroclinic tidal EF are generally found near areas where bathymetry is subcritical or near-critical on the offshore side of the 200-m isobath, e.g., such as between 41.7°N–42.2°N and 43.5°N–43.9°N. Sections with low onshore energy flux in places where bathymetry is supercritical at the shelf break are also easily identified, e.g., between 41.0°N–41.7°N, 42.3°N–42.5°N, 42.9°N–43.1°N, and 43.9°N–44.5°N.

To provide a more quantitative assessment, we consider the correlation between the magnitude of the onshore **EF** across h = 200 m and bathymetric criticality in the 10-km band offshore of this isobath. This relationship is complicated by non-uniformity of internal tide energy generation along the slope. For instance, between 44.5°N and 45°N, bathymetry is mostly subcritical just offshore of the 200-m isobath, but EF here is relatively low, since little baroclinic energy is generated offshore near this area (see Figure 2.14b). In contrast, at 42.7°N, where bathymetry is supercritical just offshore of the 200-m isobath, the onshore EF is larger than anywhere else along the 200 m isobath, because there is an extremely powerful source nearby, in the deep water at 42.3°N. To account for alongshore variation in generation, the EF magnitude at each point on the 200-m isobath is compared to the

value at a point 10 km offshore, in the direction normal to the 200 m isobath. Dividing the two values, we obtain the percent ratio of propagated **EF**, which is then compared to the mean of $\theta - \varphi$ over the 10-km distance between the two points. Results (Figure 2.22, where $\theta - \varphi > 0\circ$ corresponds to supercritical bathymetry) suggest that in general, relatively less energy propagates onshore through areas of stronger supercritical bathymetry along the shelf break rim. Two aspects of the plot necessitate further explanation. First, percentages exceed 100% at several locations where substantial internal tide energy is generated in the 10-km band. Second, strips of the supercritical bathymetry do not reflect all the internal tide energy into the deeper water. It is possible that some internal tide energy can propagate over narrow regions of supercritical bathymetry along characteristics that do not touch the slope (e.g., along characteristics that reflect off the surface in those areas).

An example of how bathymetric criticality affects the onshore **EF** and resulting tidal currents is seen in the region surrounding the Rogue River mooring. Between 42°N and 43°N, the mean onshore **EF** (Figure 2.21) and M2 tidal currents (Figure 2.10) are relatively large, except around 42.4°N. Bathymetry offshore of the 200-m isobath at 42.4°N is supercritical in a 35-km wide region next to the 200-m isobath. While this region of steep bathymetry is generating a large amount of baroclinic tidal energy (Figure 2.14a), the energy is either reflected offshore or propagated to the north and the south of 42.4◦N (Figure 13a), creating a "shadow" zone (Figure 13b) surrounding the Rogue River mooring.

It also appears that regions of relatively large TEC are frequently associated with supercritical bathymetry. 99.75% of TEC hotspots (> 0.04 W m^{-2}) are on

supercritical bathymetry. 87.67% the area with TEC greater than 0.015 W m^{-2} (the threshold separating the upper 50% of area-integrated positive TEC activity from the bottom 50%, see Figure 2.15), are also found over supercritical bathymetry.

2.6.2 *Bathymetry Roughness and Area-Integrated Energy Balance*

Figure 23 shows time-averaged, depth-integrated baroclinic **EF** vectors and standard deviation ellipses over the slope and shelf for the smoother bathymetry case. **EF** in the smoother bathymetry case is somewhat weaker, although the spatial distribution of **EF** over the 200-m isobath is similar to that in the rougher bathymetry case (cf. Figures 2.13b and 2.23b). These results are consistent with those of Jachec et al. (2007), who studied tidal circulation in Monterey Bay, California, using models of different resolution.

Another perspective on the energy balance, and its sensitivity to bathymetric resolution, is provided by area integration of the terms in (1) over the slope (200 m < h < 1800 m) and shelf (h < 200 m) regions. The time series of these terms are shown for the rougher bathymetry case in Figure 24. Integration of $\nabla \bullet \mathbf{EF}$ over the shelf yields the total energy radiating onto the shelf across the 200-m isobath (fluxes across the southern and northern boundaries are neglected). This value does not vary much with time, despite the substantial temporal and spatial variability in the M2 internal tide over the shelf. There is very little TEC over the shelf, consistent with Figures 14b,c.

Time-averages of the area-integrated terms are summarized in Figure 25, for both the rougher (a) and smoother (b) bathymetry cases. In the rougher bathymetry

case (Figure 25a), the integrated TEC over the slope has a mean value of about 81 MW. About 68% of this, approximately 55 MW, is dissipated over the slope. Integrating $\nabla \cdot EF$ over the slope yields the energy radiated out of the area, approximately 26 MW, which is nearly the sum of fluxes into the ocean interior (across the 1800 m isobath) and onto the shelf. About 14 MW are radiated from slope to shelf and about 12 MW to the interior ocean.

In the smoother bathymetry case (Figure 25b), baroclinic energy production over the slope is reduced by 34% to 54 MW. Dissipation is reduced by 38% to 34 MW. Thus, the ratio of dissipated to generated internal tide energy remains about the same over rougher and smoother bathymetry, with about 65% of baroclinic energy generated over the slope also dissipated there. In the case of smoother bathymetry, the integrated divergence of EF from the slope to the shelf is also reduced (to a total of 11 MW), but only by 18%. It appears that bathymetric resolution affects the levels of internal tide generation and dissipation more than the integrated value of onshore propagating EF.

2.7 Summary

The nested 1-km resolution model presented here describes coastal ocean circulation off Oregon in both the subinertial (wind-driven) and superinertial (semidiurnal) frequency bands quantitatively correctly. Our study has focused on generation (topographic energy conversion, TEC) and propagation of the superinertial M2 internal tide in this area. We find that most baroclinic tidal energy is generated over

the slope with a few hotspots (occupying 1.2% of the area of the continental slope) contributing 20% of the total.

Variability in both space and time is a prominent feature of the internal tide on the Oregon shelf, reflecting variation in background currents and hydrographic conditions. Although the model describes intermittency in the internal tide qualitatively correctly, the exact locations and times of intensified M2 internal tide are still difficult to predict. Furthermore, while it is clear that internal tide intermittency is associated with variability in wind-driven circulation, no simple relationship has been found between the intensity of the internal tide and characteristics of upwelling/downwelling, despite our attempts to find such a relationship.

Some aspects of baroclinic M2 energetics are quite stable. For instance, the locations of TEC hotspots are defined primarily by bathymetric details, and are relatively weakly affected by background conditions. Despite day-to-day variability in the onshore baroclinic EF, the net flux onto the shelf, integrated along the 200-m isobath, remains rather steady during the summer season. About 65% of the internal tide energy converted from the barotropic tide over the slope is dissipated on the slope. The remaining energy is propagated both into the interior ocean and onto the shelf, in roughly equal proportions. Spatial variability in the onshore energy flux is controlled to a great extent by bathymetric criticality offshore of the 200-m isobath, with areas of supercritical bathymetry along the shelf break rim reflecting a large fraction of the onshore-directed EF to deeper waters.

This study has helped us identify areas of intensified internal tide generation and propagation on the Oregon shelf, directing future observational and modeling studies toward better understanding the role of the tidal currents in the coastal ocean.

2.8 Acknowledgements

This research was supported by NSF (grants OCE-0648314, OCE-1030922), the Office of Naval Research (ONR) Physical Oceanography Program (grants N000140810942, N000141010745), NOAA-CIOSS, NOAA-IOOS (NANOOS). We also appreciate comments provided by two anonymous reviewers, who strengthened the paper in several ways.

2.9 Figures and Tables

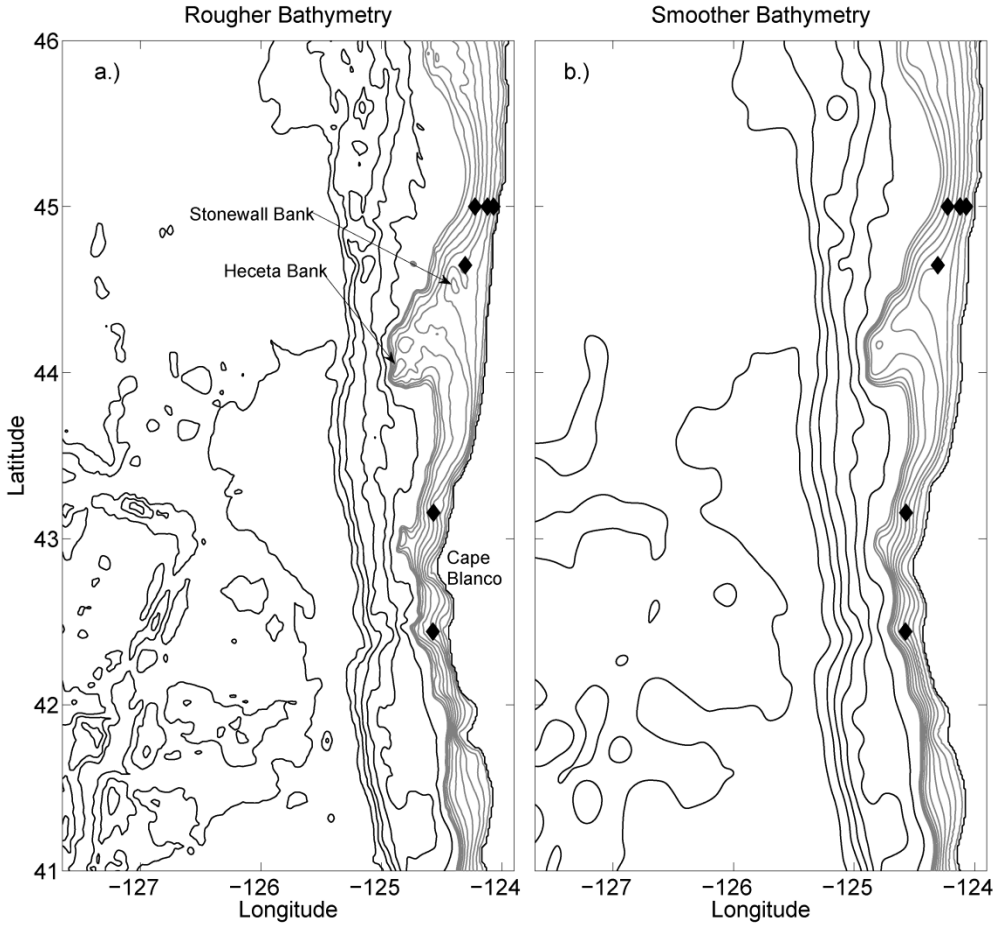

Figure 2.1 Model domain and bathymetry. The black diamond symbols along 45°N show location of three 2001 COAST ADCP moorings; the other diamonds are summer 2002 ADCP moorings. Half-tone contours are every 20 m, from the coast to 200 m depth; black contours are at every 500 m. (a) a rougher bathymetry case, (b) a smoother bathymetry case.

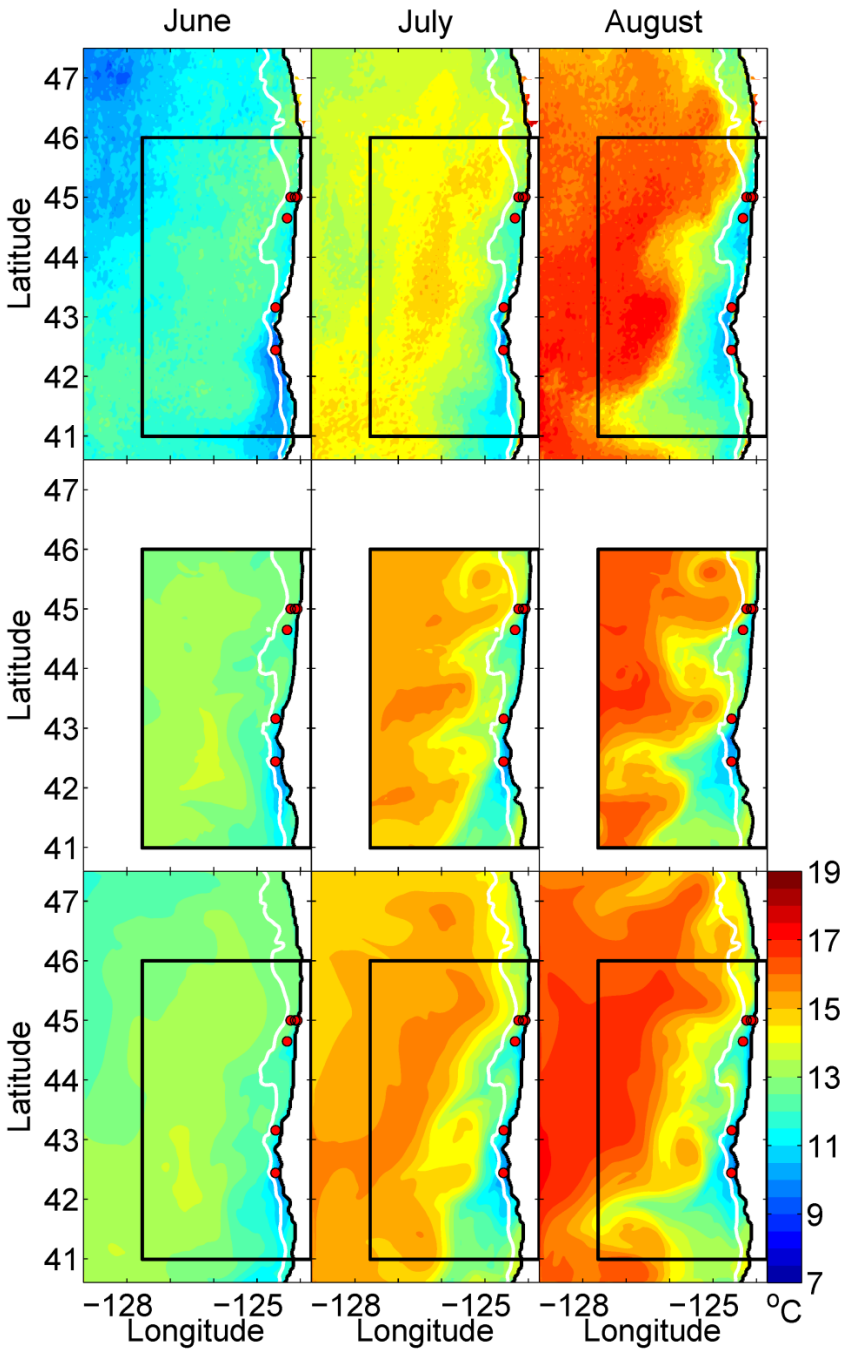

Figure 2.2 Monthly-averaged SST: (top) GOES (5.5-km resolution) satellite observations, (middle) the 1-km resolution ROMS model and (bottom) the 3-km resolution ROMS model that provided subtidal boundary conditions. Locations of ADCP moorings analyzed in this study are shown as red circles. The black rectangle is the domain of the 1-km model. The white contour is the 200-m isobath.

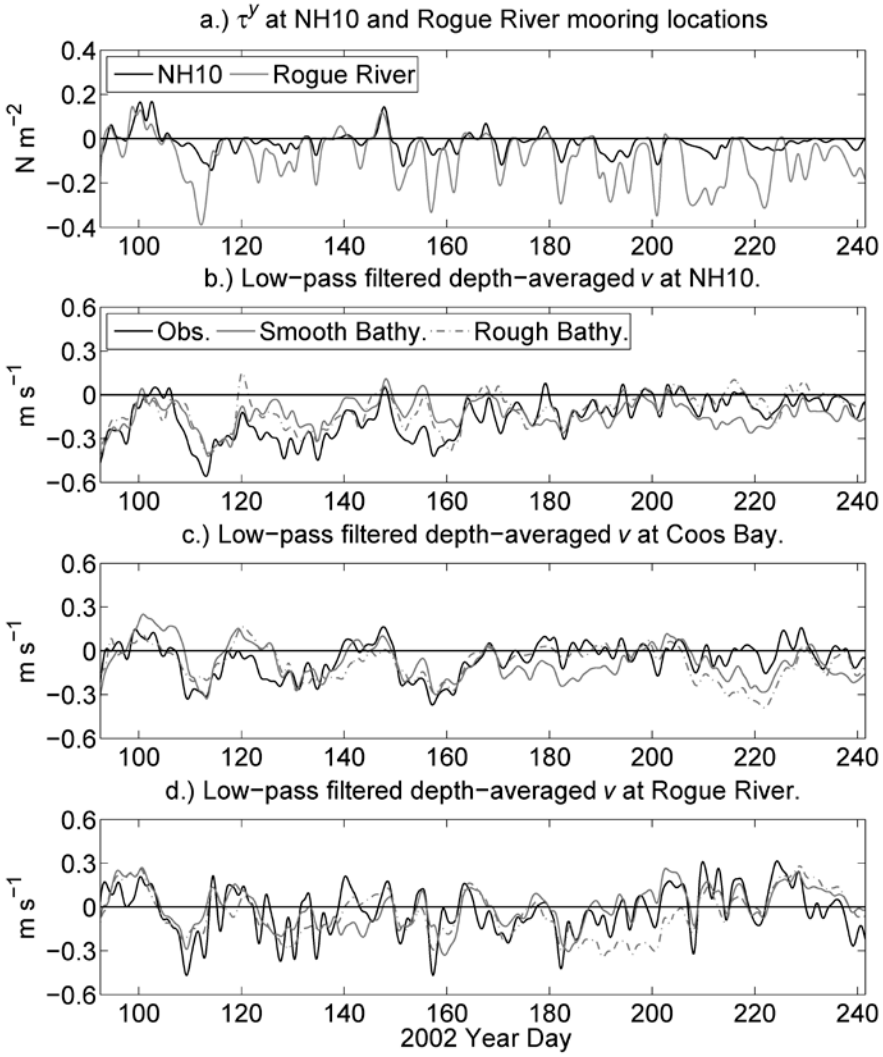

Figure 2.3 40-hour low-pass-filtered, depth-averaged observed and model meridional velocities at the NH10, Coos Bay and Rogue River mooring locations.

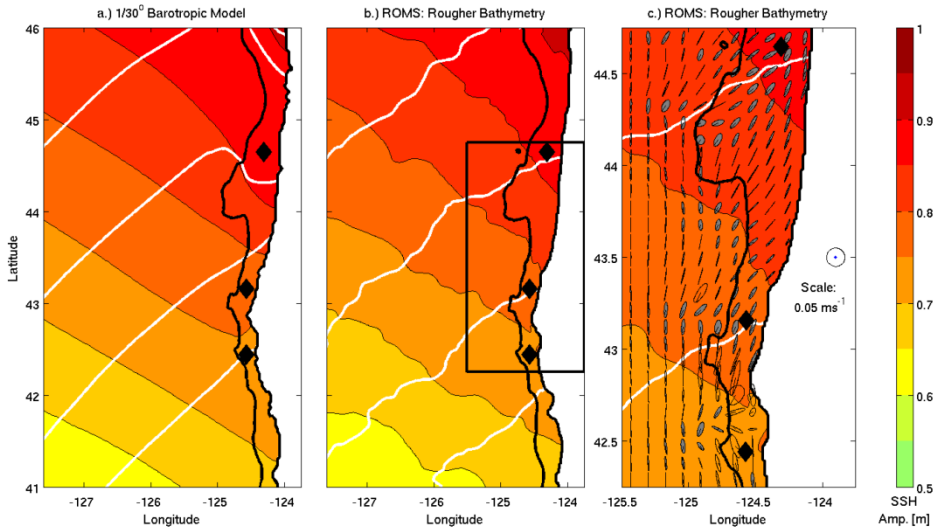

Figure 2.4 Barotropic M2 sea surface elevation tidal amplitude and phase: (a) 1/30° shallow-water equation model (Egbert et al. 1994; Egbert and Erofeeva 2002) providing tidal boundary conditions for our 1-km ROMS solution, (b) 1-km ROMS, the entire domain, and (c) 1-km ROMS, the close-up on the area shown as the black rectangle in the middle panel, with horizontal barotropic tidal current ellipses added. Shaded (clear) ellipses indicate counterclockwise (clockwise) rotation. Black diamonds mark the NH10, Coos Bay and Rogue River moorings. White phase lines are 5° apart.

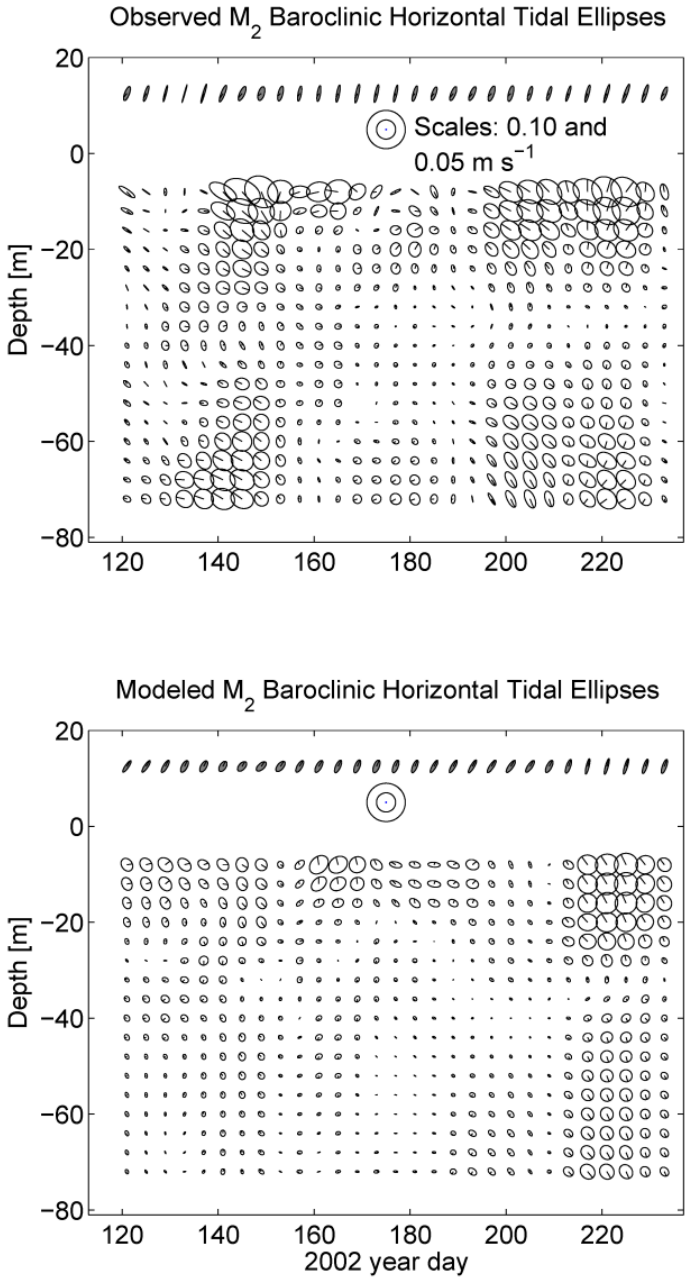

Figure 2.5 (Top) Observed and (bottom) modeled barotropic and baroclinic tidal ellipses at NH10 (h = 81 m). The vertical axis represents the depth of each tidal ellipse and the horizontal axis time (center of each 16-day analysis window). Ellipses above 10 m depth correspond to barotropic tides. Northward velocity is directed up and eastward velocity to the right. Shaded (unshaded) ellipses indicate counterclockwise (clockwise) rotation.

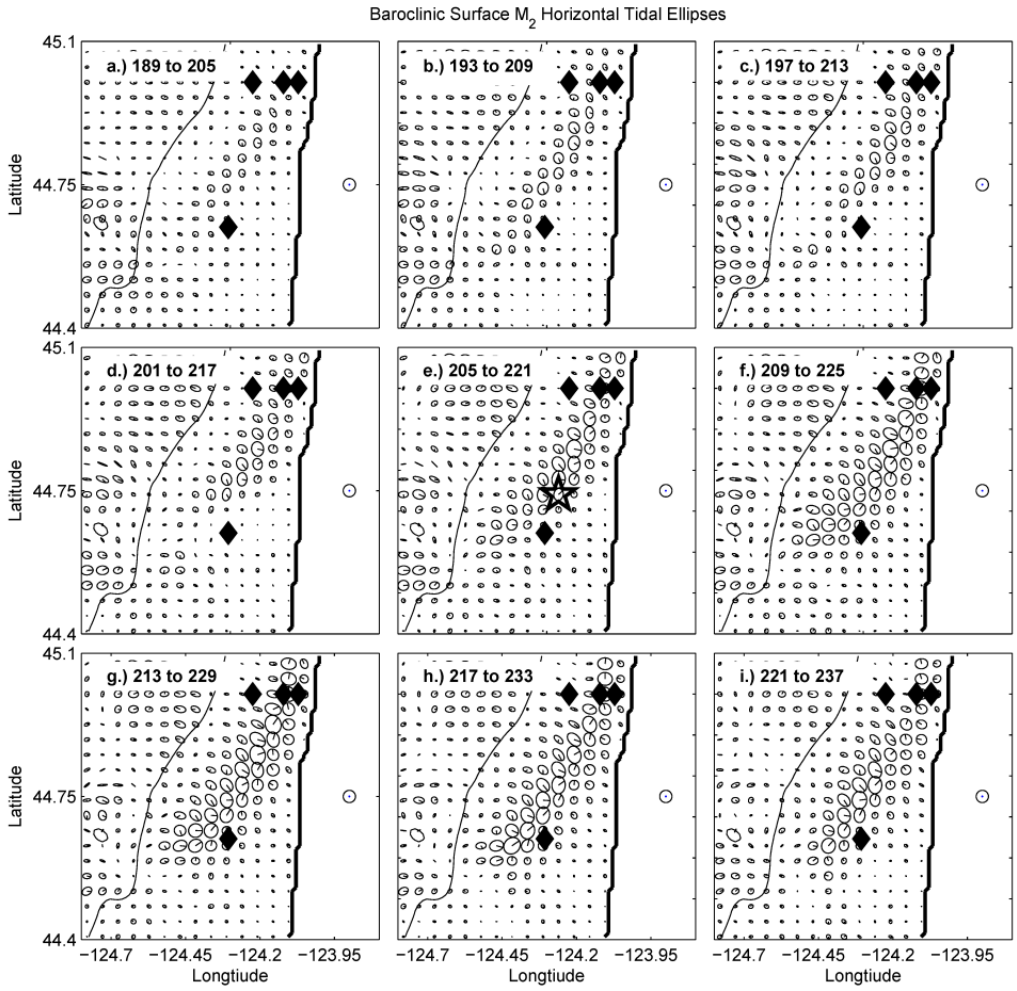

Figure 2.6 Modeled surface baroclinic M2 tidal ellipses near NH10, analyzed in 9 consecutive overlapping 16-day windows, yeardays 189–237, a period of observed intensified internal tide near NH10. The scale circle, plotted over land, is 0.1 m s^{-1}. The 200 m isobath is plotted. The black diamonds indicate the location of the NH10 mooring and three moorings from the 2001 COAST experiment. The black star in panel (e) marks the mooring location in Figure 2.7. Shaded (unshaded) ellipses indicate counterclockwise (clockwise) rotation. Ellipses are plotted with 4-km horizontal resolution.

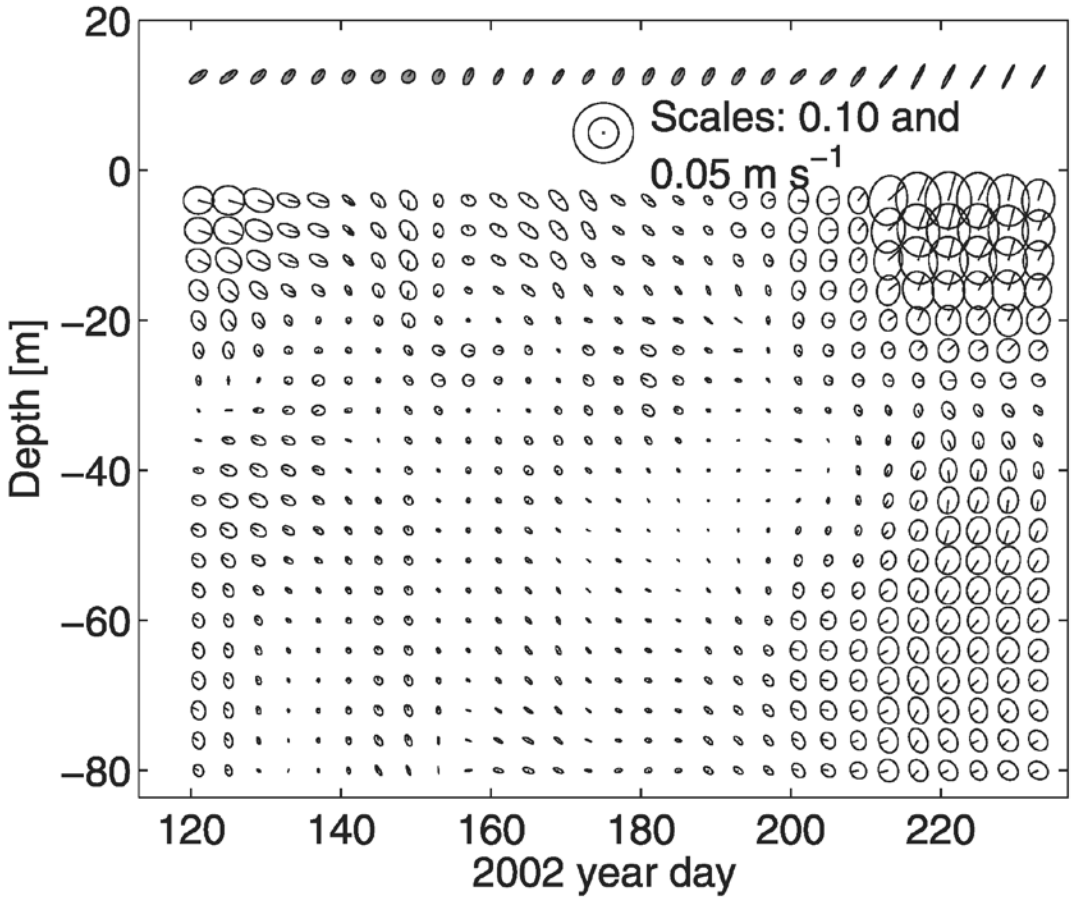

Figure 2.7 Model solution baroclinic tidal ellipses at (124.2604°W, 44.7407°N), approximately 10 km north of the NH10 mooring. Depth is 83 m. Details as in Fig. 2.5.

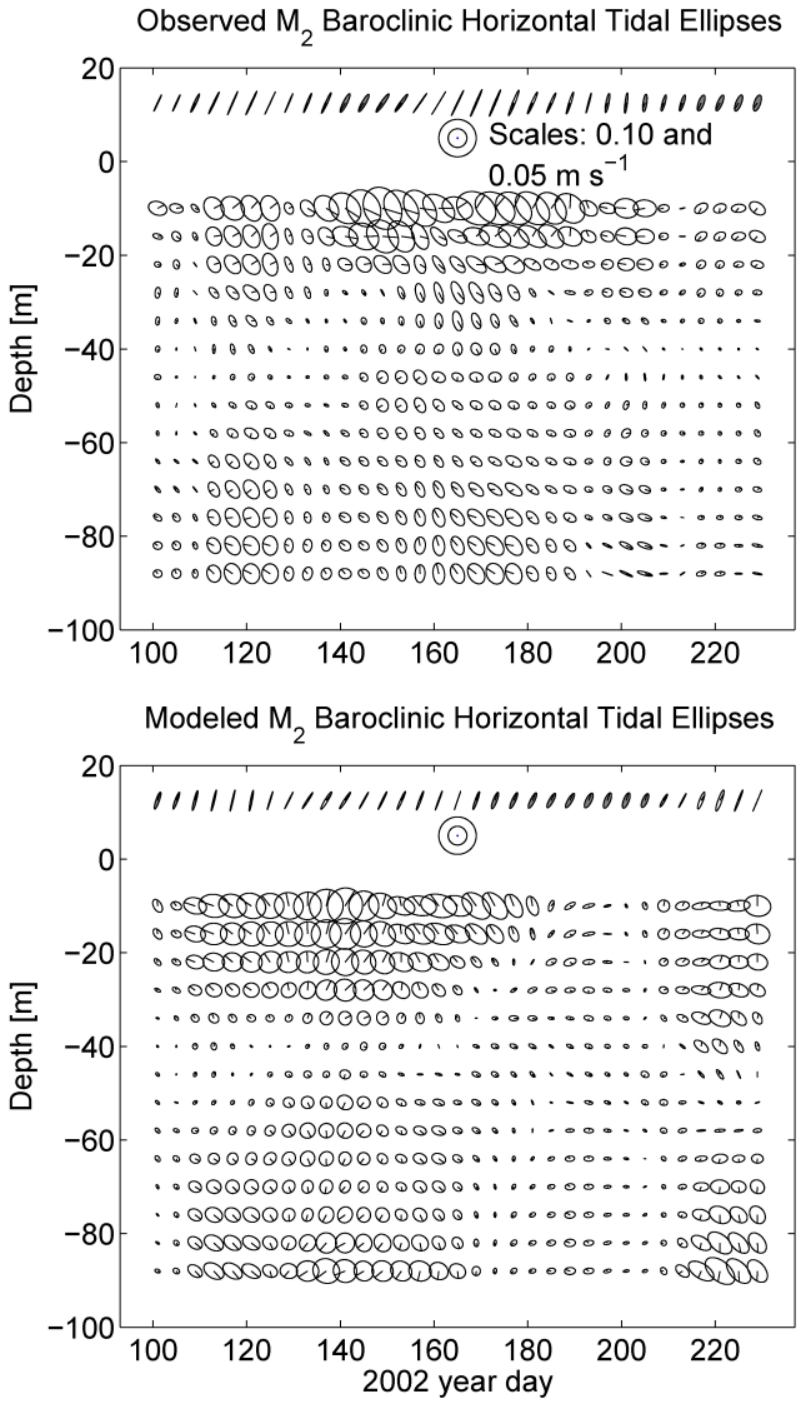

Figure 2.8 Observed (top) and modeled (bottom) solution baroclinic tidal ellipses at the Coos Bay mooring (h = 100 m). Details as in Fig. 2.5.

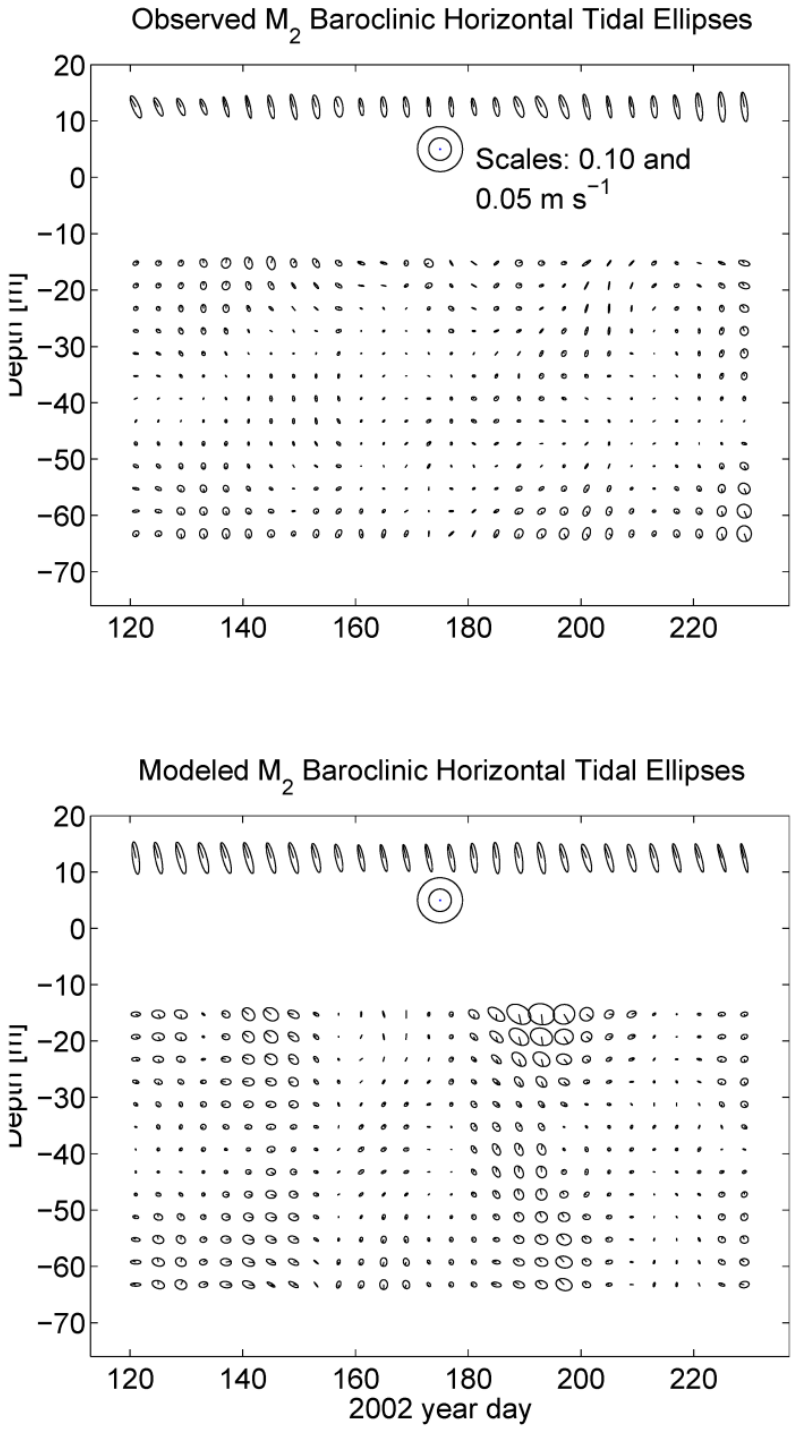

Figure 2.9 Observed (top) and modeled (bottom) solution baroclinic tidal ellipses at the Rogue River mooring (h = 76 m). Details as in Fig. 2.5.

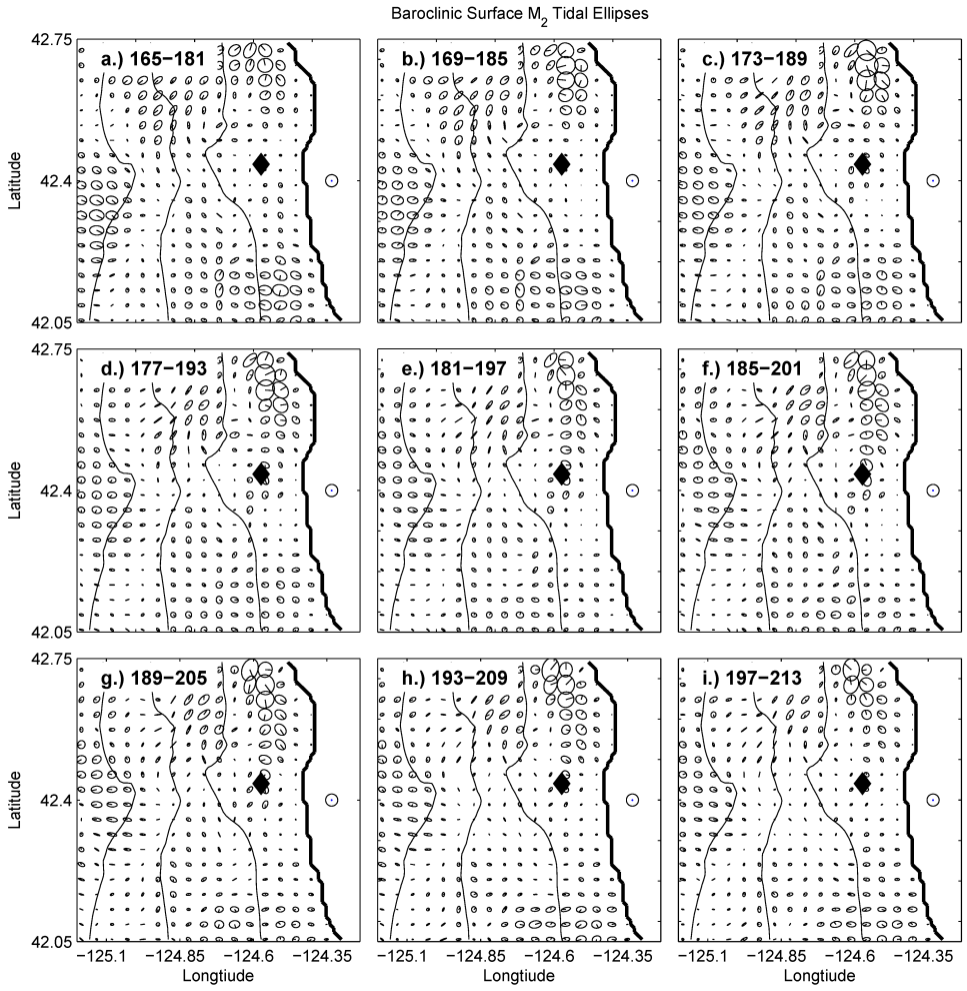

Figure 2.10 Surface baroclinic M2 tidal ellipses near Rouge River, analyzed in 9 overlapping 16-day windows (offset by 4 days), yeardays 165–213. The scale circle, plotted over land, is 0.1 m s^{-1}. Black contours are 200-m, 1000-m and 2000-m isobaths. The diamond marker is the location of the Rogue River mooring. Shaded (unshaded) ellipses indicate counterclockwise (clockwise) rotation. Ellipses are plotted with 4-km horizontal resolution.

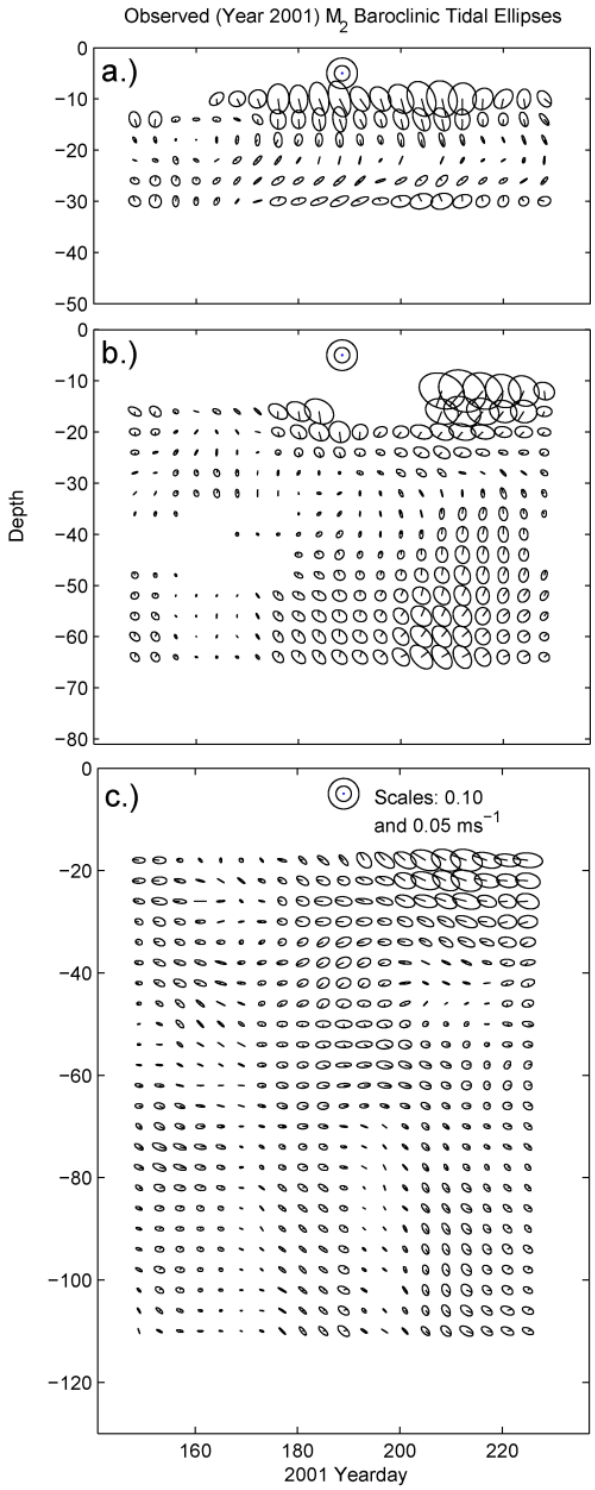

Figure 2.11 Observed baroclinic tidal ellipses during 2001 at the three COAST moorings along 45°N (from top to bottom: depths of 50 m, 81 m and 130 m).

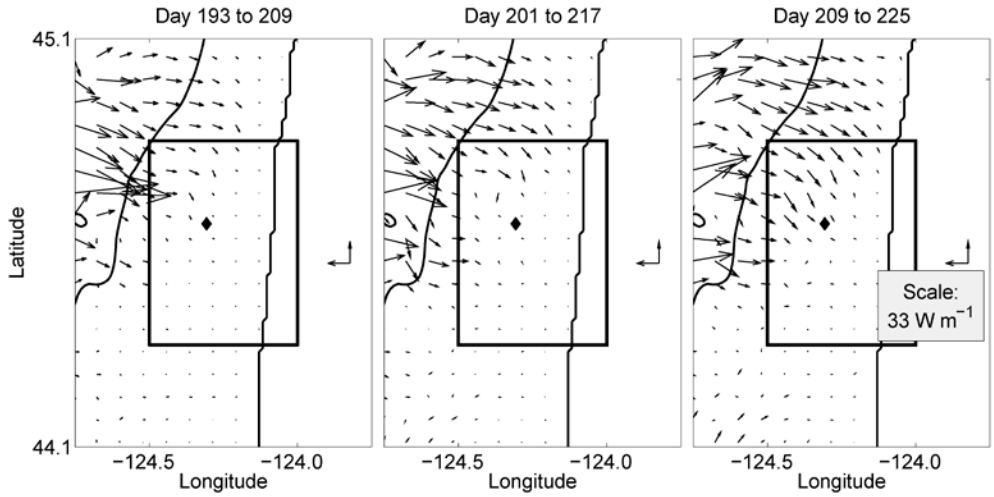

Figure 2.12 M2 baroclinic energy flux vectors analyzed in 3 partially overlapping 16-day windows over the central Oregon shelf, yeardays 193–225. The 200-m isobath contour is shown in black. The rectangle shows the extent of the model domainin Kurapov et al. (2003).

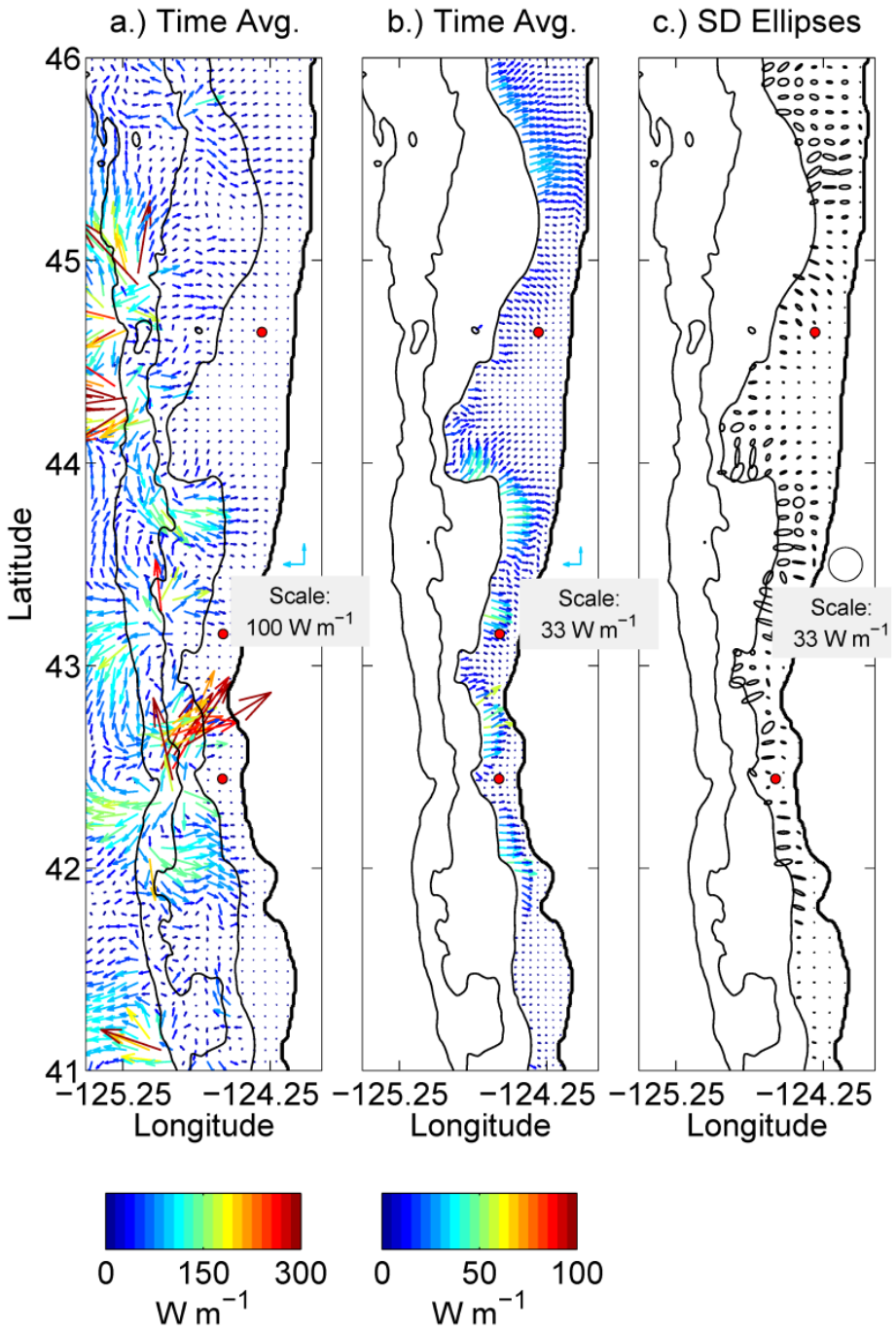

Figure 2.13 Time-average and standard deviation ellipses of the M2 baroclinic energy flux; color shows EF magnitude: (a) EF shown every 6 km, the vector scale and color range (0–300 W m^{-1}) chosen to emphasize EF on the slope, (b) EF on the shelf shown using a different vector and color scales (0–100 W m^{-1}), every 4 km, (c) standard deviation ellipses on the shelf, every 8 km. Black contours are the 200-, 1000- and 2000-m isobaths.

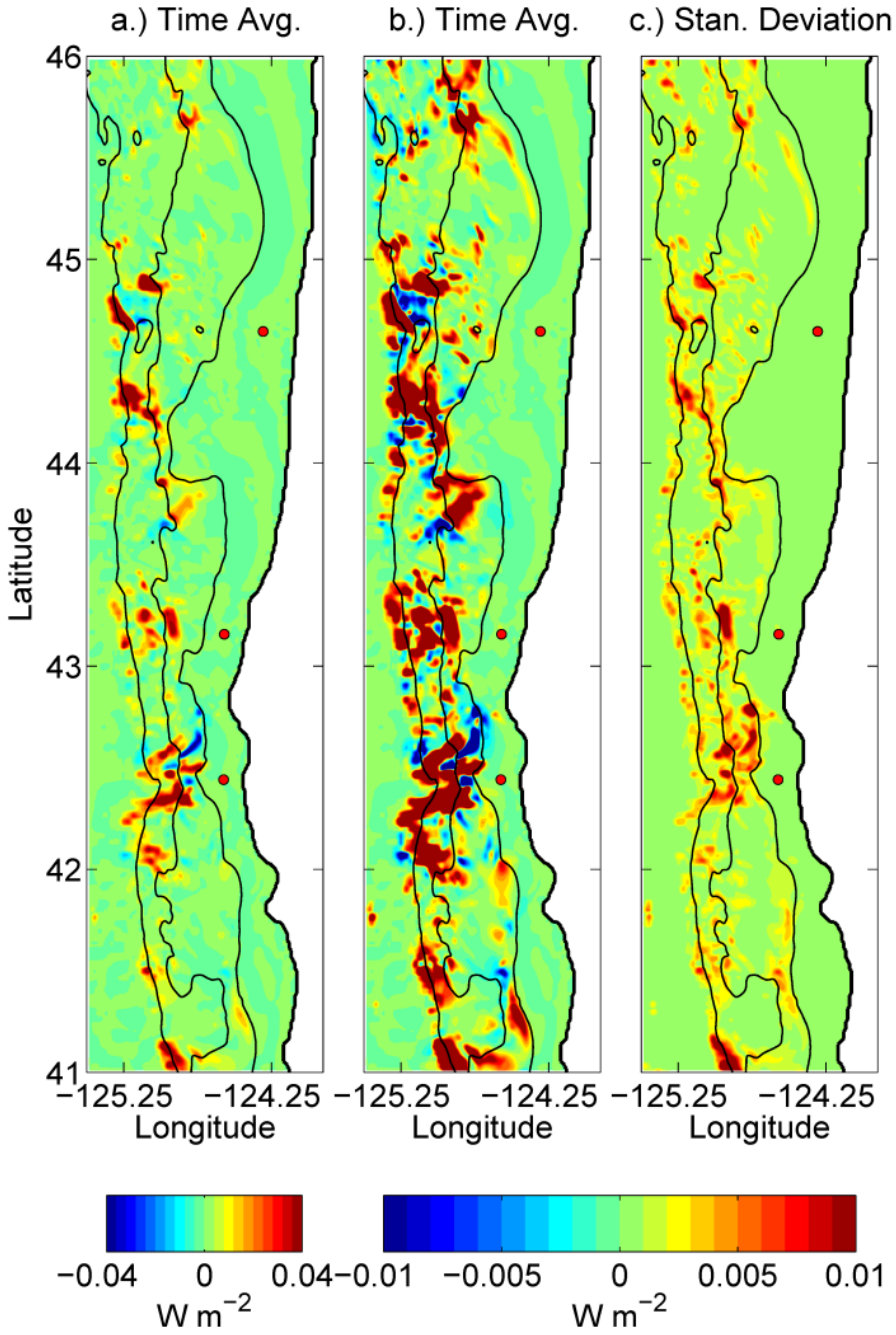

Figure 2.14 Time-average and standard deviation of TEC: (a) time-average, color range (±0.04 W m^{-2}) is chosen to emphasize hotspots, (b) time average at the finer range (±0.01 W m^{-2}), (c) standard deviation. Black contours indicate the 200-, 1000- and 2000-m isobaths.

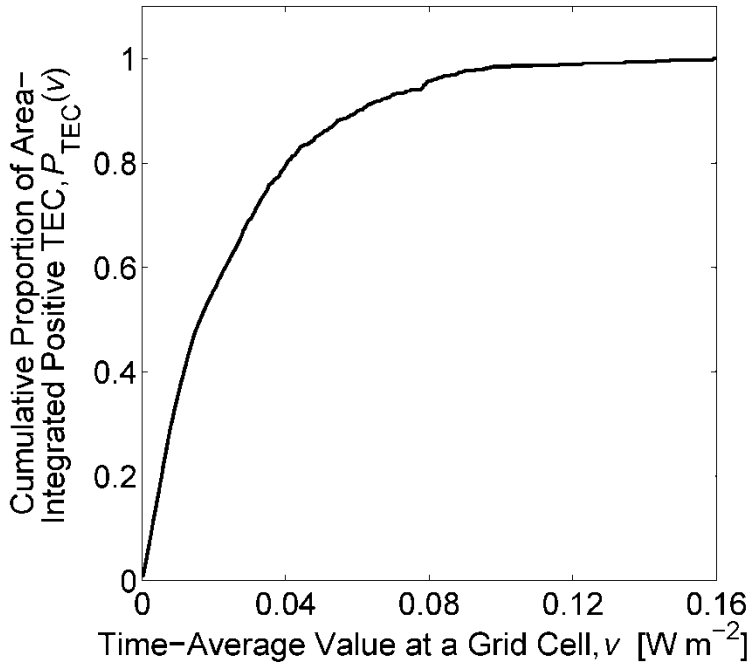

Figure 2.15 Proportion of area-integrated positive TEC, $P_{TEC}(v)$ (5), below a threshold value, v.

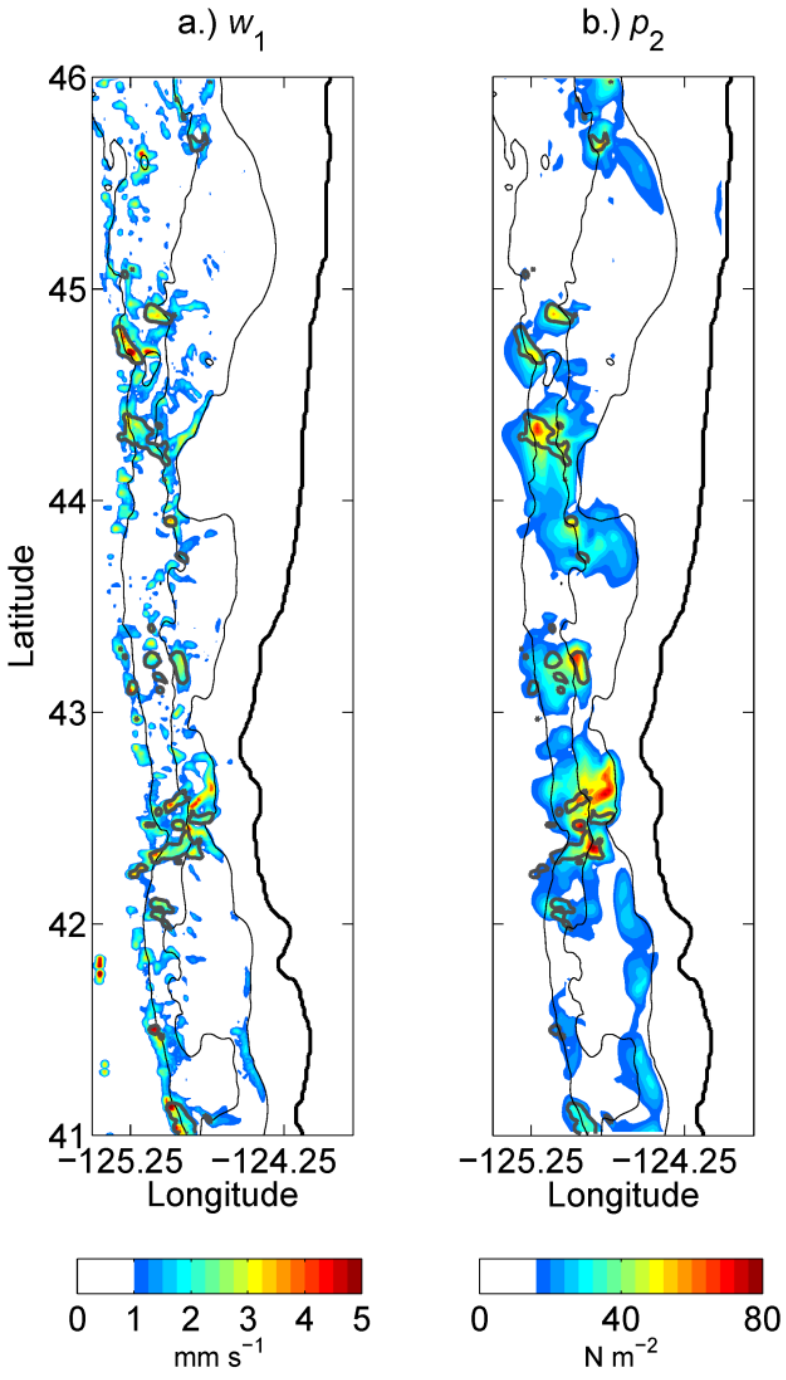

Figure 2.16 Time-averaged amplitudes of harmonic constants determining TEC (2): (a) vertical barotropic velocity at the bottom, and (b) tidal baroclinic pressure at the bottom. Black contours mark the 200-, 1000- and 2000-m isobaths. Half-tone contours mark TEC = 0.02 W m^{-2}.

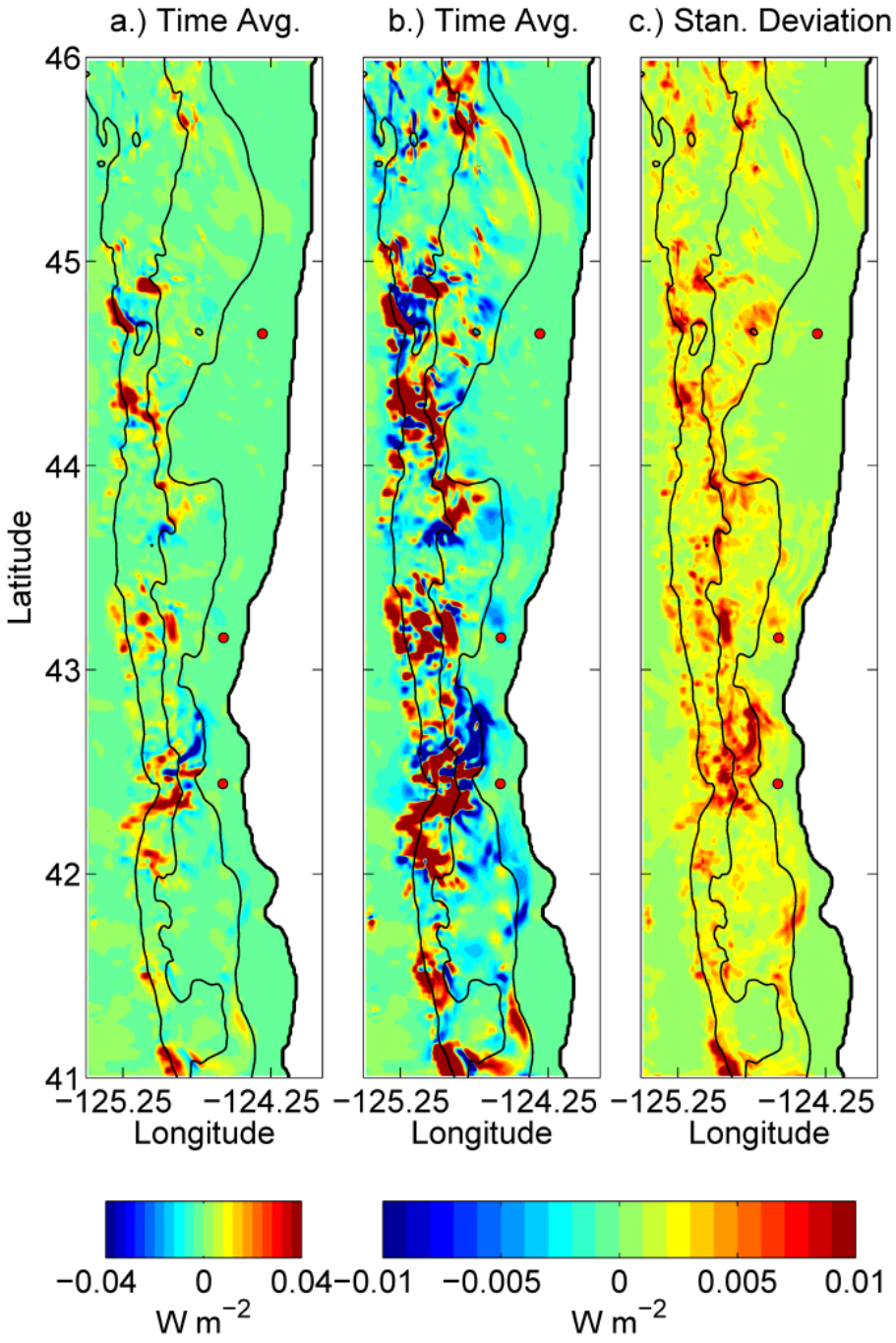

Figure 2.17 Time-average and standard deviation of the M2 baroclinic energy flux divergence: (a) time-average, color range (±0.04 W m^{-2}) is chosen to emphasize hotspots, (b) time average at the finer range (±0.01 W m^{-2}), (c) standard deviation. Black contours are the 200-, 1000- and 2000-m isobaths.

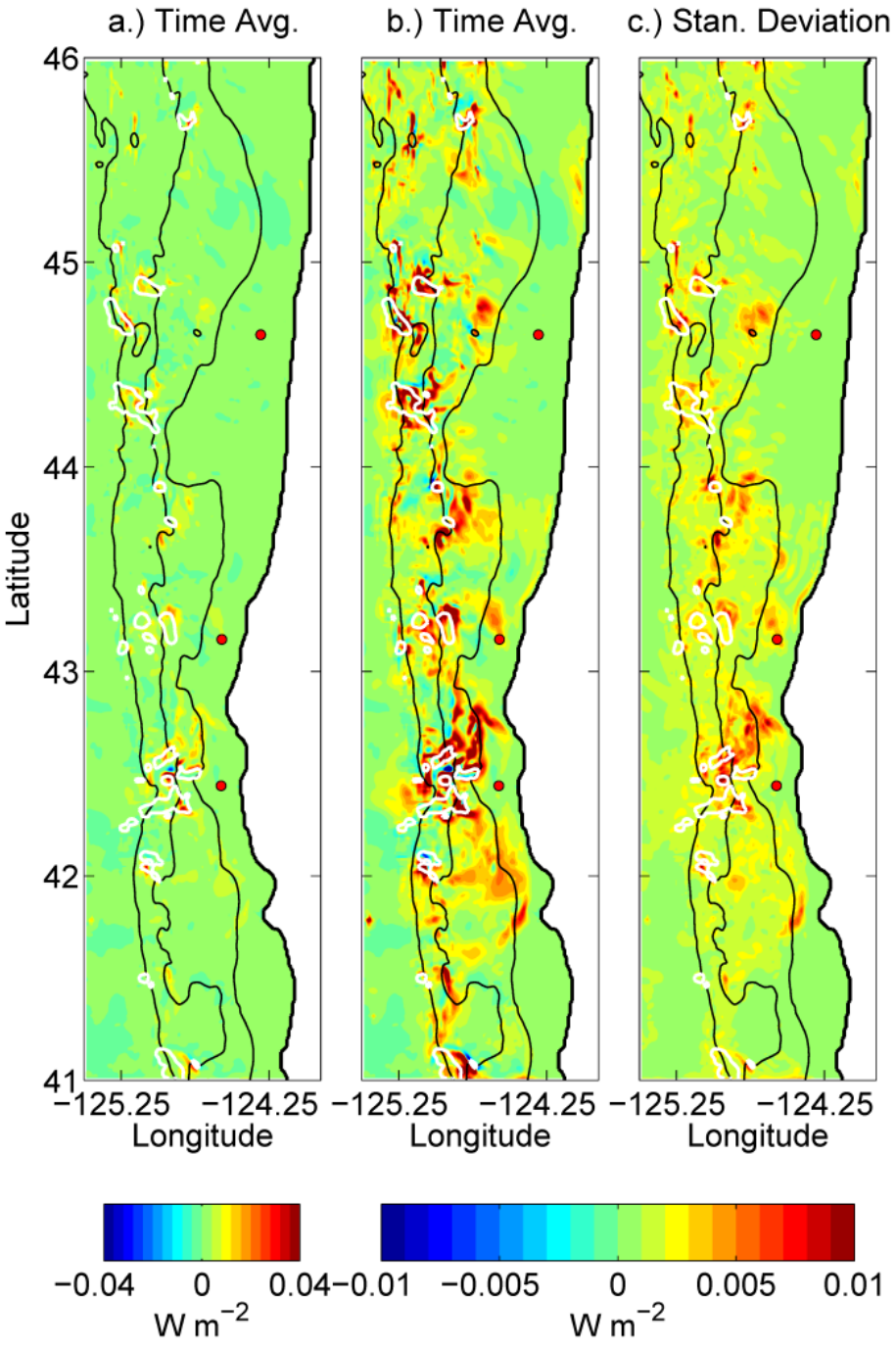

Figure 2.18 Time-average and standard deviation of the residual in (1): (a) time-average, color range ±0.04 W m^{-2} , (b) time average at the finer range (±0.01 W m^{-2}), (c) standard deviation. Black contours are the 200-, 1000- and 2000-m isobaths.

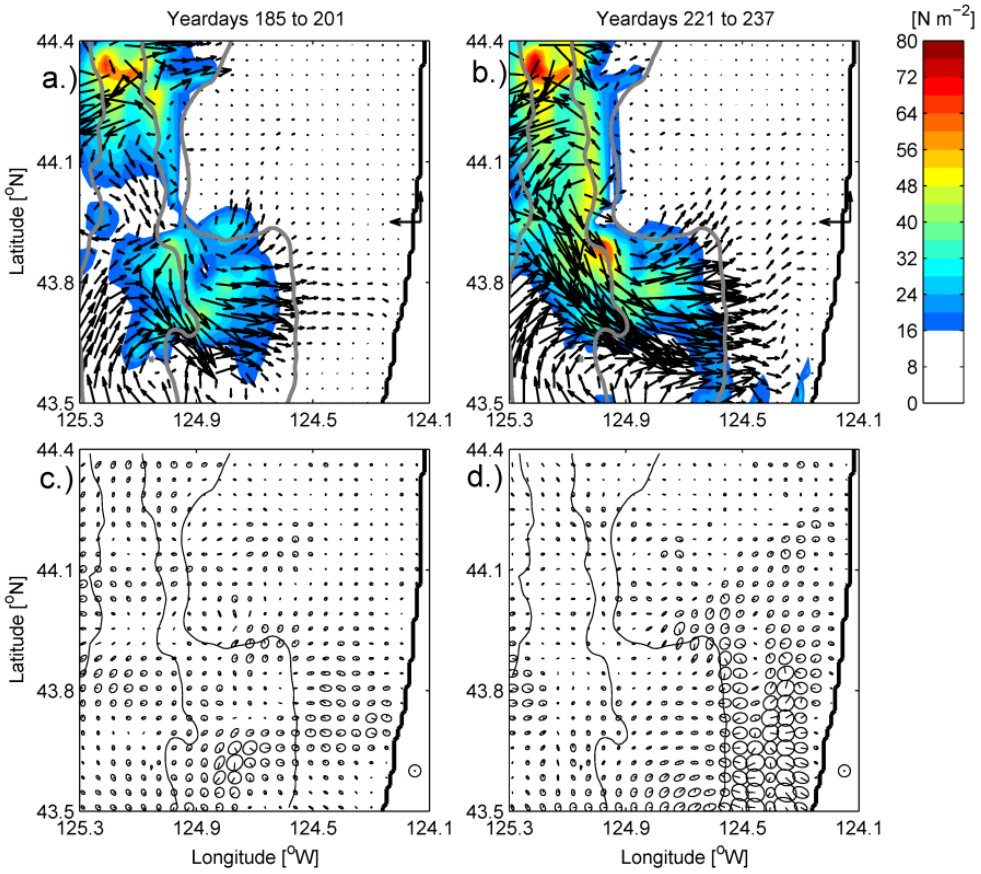

Figure 2.19 Top: Depth-integrated, tidally-averaged M2 baroclinic energy flux vectors and bottom baroclinic pressure during yeardays 185-201 (a) and 221-237 (b). The 200-, 1000- and 2000-m isobaths are contoured in gray. Scale vectors (rightof each panel) are 100 W m^{-1}. Bottom: Surface baroclinic tidal ellipses for the corresponding time periods. Scale circle at lower right is 0.10 m s^{-1}. Isobaths are contoured at the same intervals.

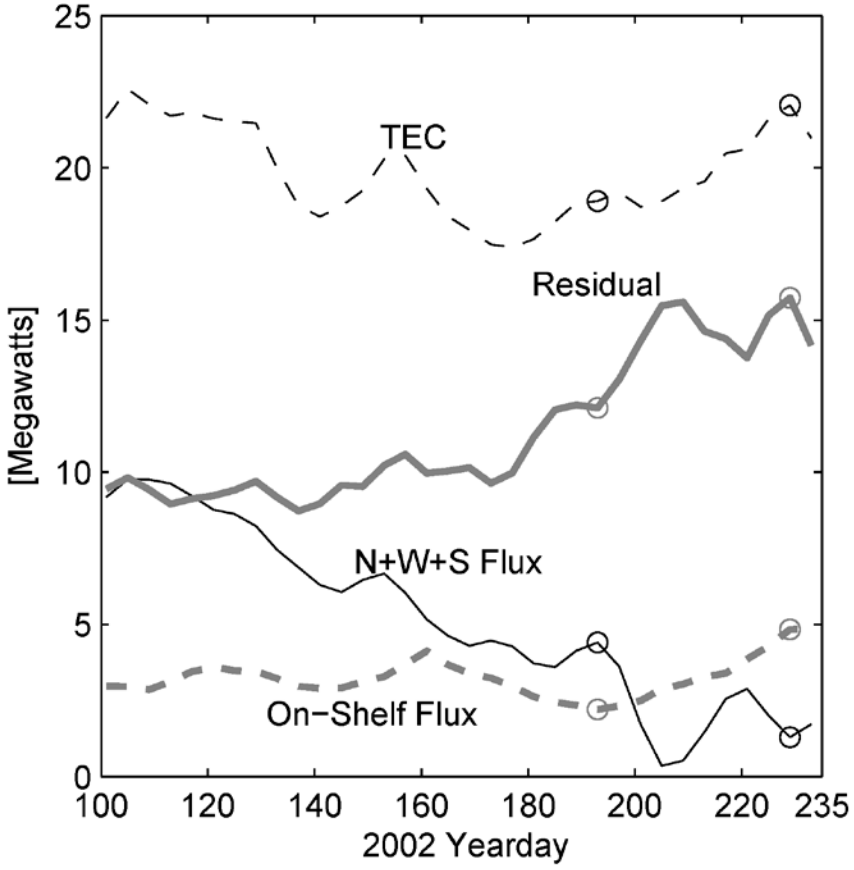

Figure 2.20 Time series of energy balance terms for the slope region in Figure 2.12 ([125.3°W, 200-m isobath]×[43.5°N, 44.4°N]). For the flux terms, positive values correspond to energy radiating out of the region. Circles on each line mark yeardays 193 and 229, the midpoints of the windows in Figure 19.

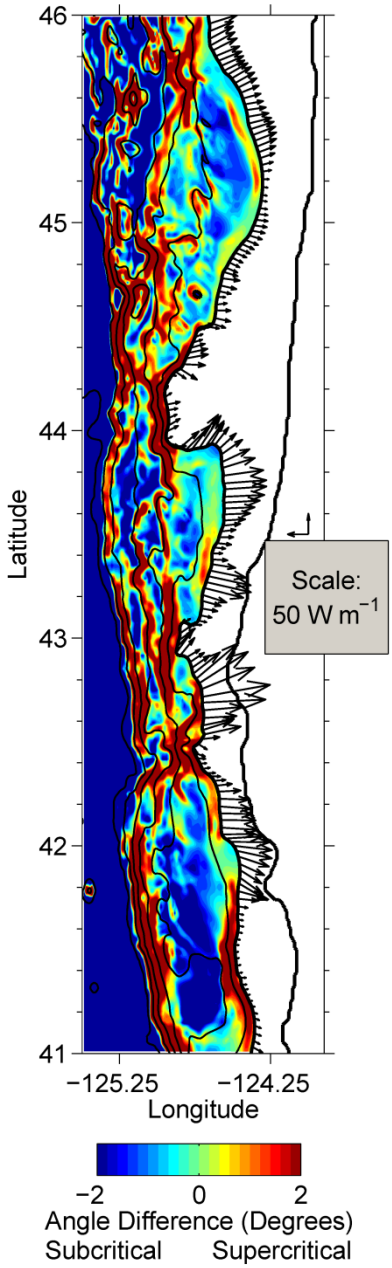

Figure 2.21 Bathymetric criticality (bathymetric slope angle minus wave characteristic slope angle), shown over the continental slope (color, shelf omitted), and EF across the 200 m isobath (vectors). Positive bathymetric criticality (warm colors) corresponds to the steep, supercritical slope. Thick black contours are the coast and 200 m isobaths. Thin black contours are every 500 m.

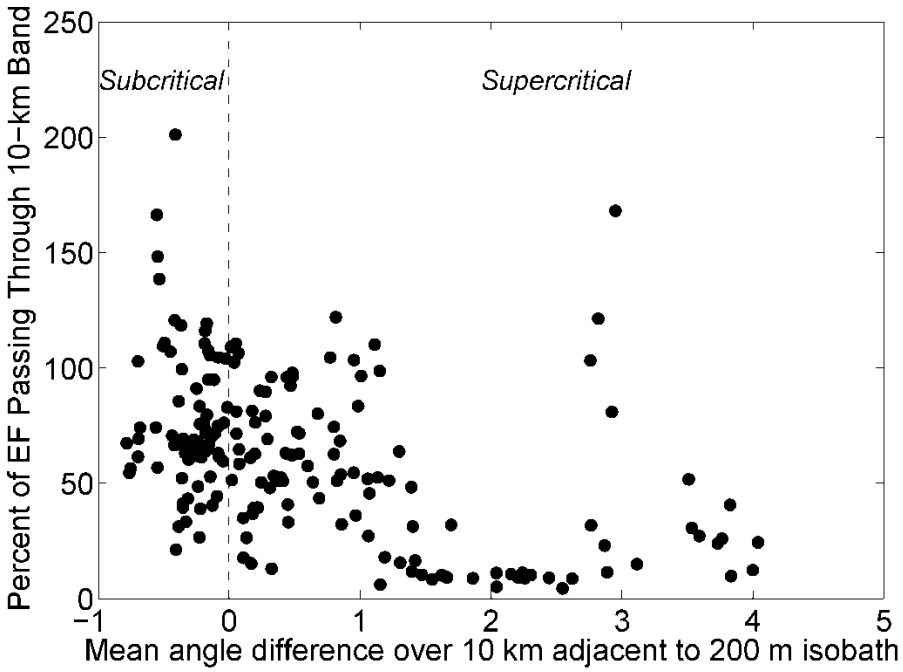

Figure 2.22 Scatter plot of the percent ratio of EF passing through the 10-km strip offshore of the 200 m isobath versus the mean angle difference (bathymetric slope minus wave characteristic slope). Averaging is in the direction perpendicular to the 200 m isobath. Positive angle difference corresponds to supercritical bathymetry, negative to subcritical bathymetry.

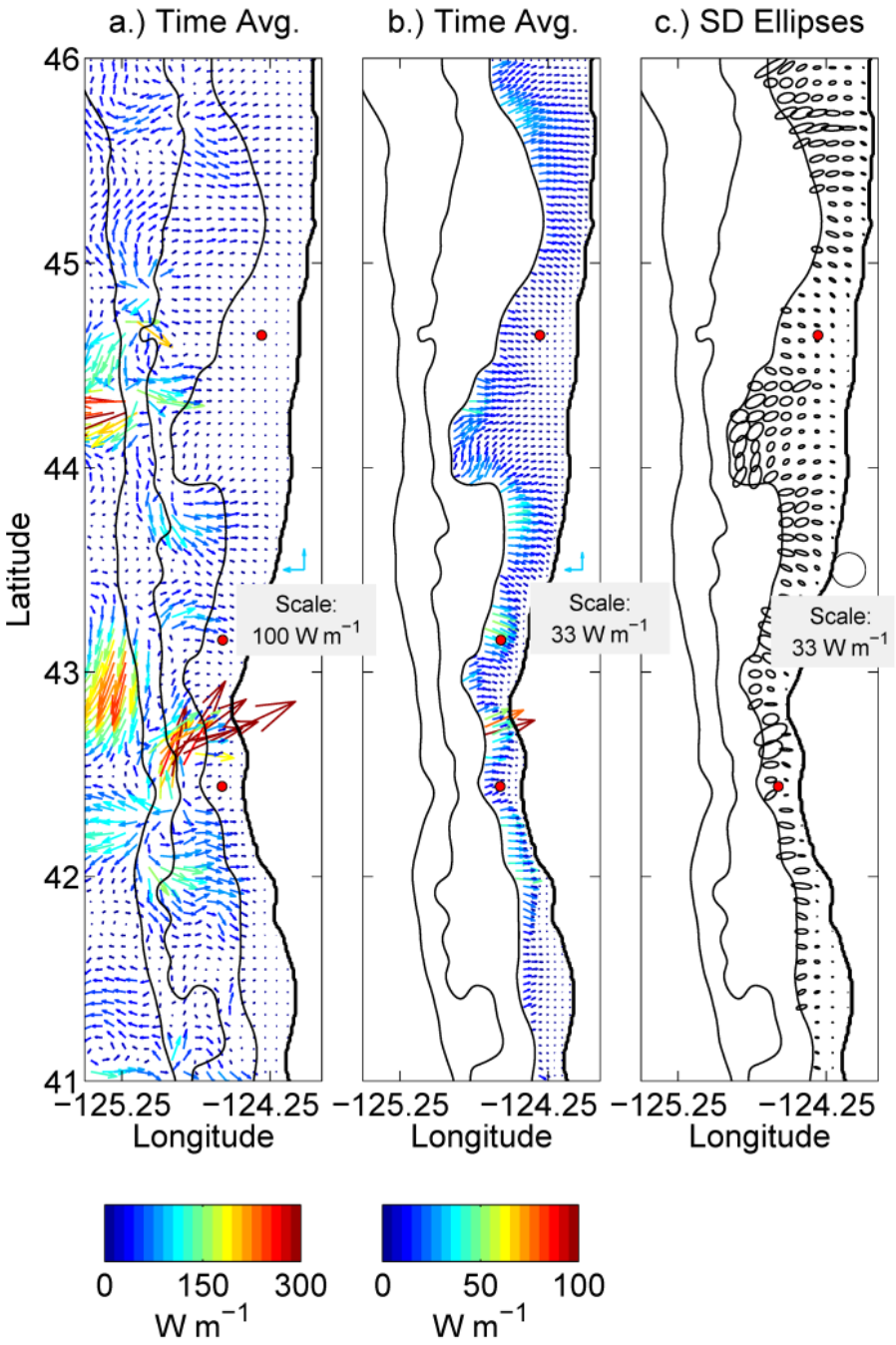

Figure 2.23 Time-averaged M2 baroclinic energy flux vectors and standard deviation ellipses from the smoother bathymetry case. Details as in Figure 2.13.

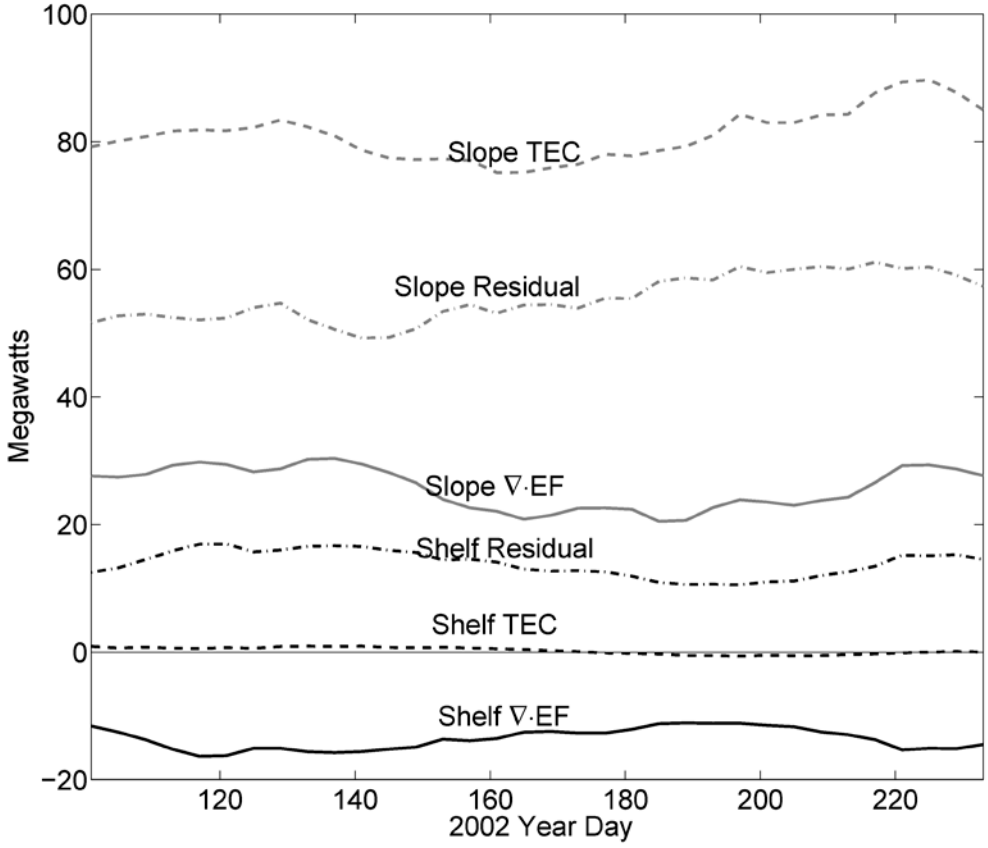

Figure 2.24 Time series of the area-integrated TEC, ∇ • EF, and the residual. Half-tone lines are for the area between the 1800- and 200-m isobaths (the slope) and black lines for the area between the 200-m isobath and the coast (the shelf).

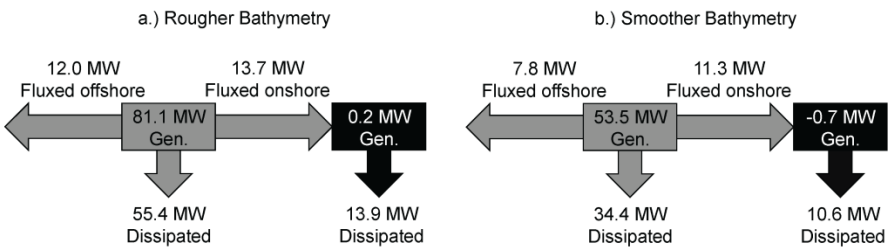

Figure 2.25 Diagrams summarizing time-averaged TEC, dissipation and energy flux over the slope (white) and the shelf (half-tone): (a) the rougher bathymetry case, (b) smoother bathymetry case.

TABLE **2.1** Model-data statistics for the depth-averaged currents at mooring locations.

	Observations			Smoother Bathymetry			Detailed Bathymetry		
Statistic	NH10	CB	RR	NH10	CB	RR	NH10	CB	RR
Mean [m s^{-1}]	-0.16	-0.06	-0.03	-0.14	-0.08	0.00	-0.11	-0.09	-0.05
Standard Deviation [m s^{-1}]	0.14	0.12	0.16	0.09	0.13	0.13	0.12	0.12	0.15
RMS [m s^{-1}]	-	-	-	0.12	0.12	0.12	0.09	0.11	0.14
Complex Correlation	-	-	-	0.44	0.48	0.64	0.72	0.47	0.59
Complex Phase Angle	-	-	-	3°	-1°	16°	1°	-3°	11°

TABLE **2.2** The mean of the major axis amplitude (m s^{-1}) and mean and standard deviation ($\mu \pm \sigma$) of the angle of inclination (relative to due east) of observed and modeled depth-averaged M_2 tidal currents at the NH10, Coos Bay and Rogue River moorings. Standard deviation of the major axis amplitude is small ($< .01$ m s^{-1}). For both observed and modeled velocities, the depth average is taken only over the depths at which observations are available. Statistics are computed from harmonic constants from 29 time windows. Inclination is degrees north of east

	NH10		Coos Bay		Rogue River	
	Obs.	Model	Obs.	Model	Obs.	Model
Major Axis Amp. [m s^{-1}]	0.04	0.04	0.06	0.05	0.05	0.07
Inclination	$73° \pm 3°$	$62° \pm 8°$	$67° \pm 6°$	$67° \pm 6°$	$102° \pm 6°$	$102° \pm 3°$

3. Intensified Diurnal Tides Along the Oregon Coast

J. J. Osborne, A. L. Kurapov, G. D. Egbert and P. M. Kosro

Journal of Physical Oceanography

45 Beacon Street

Boston, MA 02108-3693

In press

3.1 Abstract

Intensified diurnal tides are found along portions of the Oregon shelf (US west coast), based on analyses of high-frequency (HF) radar surface current data and outputs of a 1-km resolution ocean circulation model. K1 tidal currents with magnitudes near 0.07 m s^{-1} over a wider part of the shelf (Heceta Bank Complex, 44-44.5°N), previously predicted by Erofeeva et al. (2003), are confirmed here by newly available HF radar data. Intensified diurnal tides are also found along the narrow shelf south of Heceta Bank. In the close vicinity of Cape Blanco (42.8°N), diurnal tidal currents (K1 and O1constituents combined) may reach 0.3 m s^{-1}. Appreciable differences in diurnal tide intensity are found depending on whether the model is forced with tides and winds (case TW) or only tides. Also, diurnal variability in wind forcing is found to affect diurnal surface velocities. For the case forced by tides alone, results strongly depend on whether the model ocean is stratified (case TOS) or not (case TONS). In case TONS, coastal trapped waves at diurnal frequencies do not occur over the narrow shelf south of 43.5°N, consistent with dispersion analysis of a linear shallow water model. However, in case TOS, diurnal tides are intensified in that area, associated with the presence of coastal trapped waves. Case TW produces the strongest modeled diurnal tidal motions over the entire Oregon shelf, partially due to cross-shore tidal displacement (advection) of alongshore subinertial currents. At Cape Blanco, diurnal tidal variability dominates the modeled relative vorticity spectrum, suggesting that tides may influence separation of the along-shore coastal jet at that location.

3.1 Introduction

Summer circulation off the Oregon coast is characterized by wind-driven coastal upwelling varying on temporal scales of several days, driving a southward jet with mean speed near 0.5 m s^{-1}. As summer progresses, the cold SST front (Figure 1a) is driven offshore by Ekman transport, eddy variability, and separating coastal jets. Tides are dominated by the M2 constituent (period of 12.42 hr), with barotropic (depth-averaged) currents of up to 0.06 m s^{-1} over the shelf and internal tides reaching 0.15 m s^{-1} (Hayes and Halpern 1976; Torgrimson and Hickey 1979; Erofeeva et al. 2003; Kurapov et al. 2003; Osborne et al. 2011). Energetic diurnal tidal currents may also occur locally along the Oregon coast. A data-assimilating shallow-water ocean tidal model (Erofeeva et al. 2003) suggests that K1 tidal currents (period of 23.93 hr) may exceed 0.10 m s^{-1} over the wide Heceta Bank portion of the Oregon shelf (44-45°N). Reexamining historical current meter data, Erofeeva et al. (2003) also found that O1 currents could reach up to 0.08 m s^{-1}. The intensification of K1 currents was attributed to coastal trapped waves at a subinertial diurnal tide frequency. These have been associated with intensified diurnal tides in several places around the world, e.g., St. Kilda Island, UK (Cartwright 1969), Vancouver Island, Canada (Crawford and Thomson 1982; Cummins et al. 2000), and the Sea of Okhotsk, Russia (Kovalev and Rabinovich 1980; Yefimov and Rabinovich 1980; Rabinovich and Zhukov 1984; Odamaki 1994; Rabinovich and Thomson 2001).

While tidal currents are usually less energetic than wind-driven currents off Oregon, our recent model results using a comprehensive three-dimensional coastal ocean model (described in section 3.3) reveal that the shape of the SST front may be sensitive to details of barotropic tidal forcing. Cases using atmospheric forcing only (Figure 3.1b), atmospheric forcing plus M2 tides along the open boundaries (Figure 3.1c), or atmospheric forcing plus eight tidal constituents (from shortest period to longest: K2, S2, M2, N2, K1, P1 , O1 , and Q1; Figure 3.1d) yield, after five months of simulation, SST fronts of quite different shape. For comparison, the observed August 2002 SST field (from GOES satellite observations, Maturi et al. 2008) is shown in Figure 3.1a. While differences in the SST front geometry possibly reflect the high sensitivity of the non-linear hydrostatic model to small changes in the boundary conditions (Oliger and Sundstrom 1978), it is also possible that tides influence dynamics at subtidal frequencies, e.g., affecting coastal jet separation and offshore transport. This sensitivity has motivated us to look closer at diurnal tides using model results and surface currents observed by high frequency (HF) radars. Strong observed and modeled diurnal currents are found in the area identified by Erofeeva et al. (2003) (section 3.4). Large tidal velocities are also found near Cape Blanco (see Figure 3.1), resulting from a combination of mechanisms discussed in sections 3.5 and 3.6, including coastal trapped waves and the cross-shore advection of the subinertial alongshore jet by the diurnal tidal current.

3.3 Model

The model is based on the Regional Ocean Modeling System (ROMS, Shchepetkin and McWilliams 2005, www.myroms.org) that describes non-linear evolution of stratified flows using hydrostatic and Boussinesq approximations. Use of terrain-following coordinates in the vertical makes it particularly suitable for shelf flow studies, since the surface and bot- tom boundary layers can be finely resolved. Details of the implementation used here are very similar to Osborne et al. (2011). The model domain is (127.6°W-coast, 41-46°N), with resolution of 1 km in the horizontal and 40 terrain-following levels in the vertical. The study period is April through August 2002. Unless noted, winds are daily averages from the Coupled Ocean Atmosphere Mesoscale Prediction System (COAMPS; Hodur 1997) and parameters for surface heat flux computation are monthly averages from the National Centers for Environmental Prediction (NCEP) reanalysis (Kalnay et al. 1996). The daily-averaged winds are used to remove atmospheric diurnal variability, isolating diurnal tides as the only forcing mechanism with a 24-hour period. An additional model run is done using high-frequency (hourly resolution) winds to assess the response of near-surface currents to diurnal atmospheric variability. Subtidal boundary conditions are obtained from a 3-km regional ocean circulation model (Koch et al. 2010) and barotropic tides from a US West Coast 1/30° shallow-water data-assimilating model (Egbert and Erofeeva 2002, http://volkov.oce.orst.edu/tides/). Tidal forcing is applied by periodically varying (at each of the eight tidal frequencies) the velocity and sea surface height along the boundaries. No tidal forcing of any kind is directly applied to

any interior grid points. Several cases are considered below. Case TW ("tides plus winds") is forced by the winds, atmospheric heat fluxes, and the eight dominant tidal constituents. Case TONS ("tides only, no stratification") is forced by tides only and simulates the response of the unstratified ocean that has zero initial velocity. Case TOS ("tides only, stratified") is forced by tides only applied to the stratified ocean, which was initially at the state of rest (zero velocities and horizontally uniform stratification corresponding to average summer conditions off Oregon, Smith et al. 2001). Instantaneous model outputs are saved hourly for subsequent filtering and harmonic analysis.

3. Case TW: comparison against high frequency (HF) radar surface currents

Erofeeva et al. (2003) noted local intensification of K1 and O1 currents over the broader portion of the Oregon shelf between 44-45°N (Heceta and Stonewall Banks). In their study, surface velocities from short range (40 km) HF radars were assimilated, but those data did not cover the entire Heceta Bank area. Thestrongest modeled K1 tides were more than 40 km from the radar, thus, no direct observational evidence was available at that time to confirm the strongest model K1 tides. Surface current data from three 150 km long-range HF radars with overlapping coverage are now available in this region (Figures 3.2a-c and 3.3a-c; Kosro 2005; Kosro et al. 2006; Saraceno et al. 2008), located at 42.84°N (Cape Blanco Long, CBL), 43.67°N (Winchester Bay, WIN), and at 44.68°N (Yaquina Head Long, YHL). We analyze

hourly observations from CBL and WIN for June-August 2002 (92 days) and hourly observations from YHL (installed later) for June-July 2008 (61 days). Crawford and Thomson (1984) conclude that seasonally-varying ocean conditions (currents and stratification) may have a significant impact on diurnal tides. Comparisons using model outputs and data from different years are justified since they are from the same time of year. Each radar senses the radial component of the surface currents, along the line from the radar to the measurement point. While maps of two orthogonal velocity components (i.e., east-west/north-south) can be obtained in areas of overlapping coverage, we choose to analyze radial velocity component data here, since they provide more uniform accuracy and better resolution (no issue with geometric dilution of precision).

The HF radar radial velocity component time series have been harmonically analyzed using the T_TIDE software package (Pawlowicz et al. 2002). We infer for the P1 constituent, as none of the time series are long enough to separate the P1 and K1 constituents (178 day beat period). Here we provide analysis of both the K1 and O1 tidal amplitudes. The observed K1 signal is stronger than O1, but may be contaminated by diurnal wind-driven variability. The diurnal wind frequency differs from the K1 frequency by one cycle per year, such that signals at these two frequencies are difficult to separate in 2-3 month time series. The diurnal wind stress variability can be relatively large in the vicinity of Heceta Bank, as compared to the daily mean over the summer season. Perlin et al. (2004) examined twice- daily QuikSCAT (Liu 2002; Liu and Xie 2001) observations from June-September 2000 and 2001 and found that the mean difference between mooring and evening winds

may be as large as 0.04 N m^{-2} over a vast area of the Oregon shelf and slope, extending as far as 100 km offshore.

The observed O1 signal, though weaker than the K1 signal, is more easily separated from atmospherically forced diurnal signals. Comparing maps of diurnal current amplitudes at the K1 and O1 frequencies, we will attempt to delineate areas influenced by the tides and diurnal atmospheric variability.

Observed harmonic amplitudes are plotted in Figures 3.2 (left) and 3.3 (left) for the K1 and O1 constituents, respectively. The K1 observations between 44-45°N (Figures 3.2a and 3.2b) show large areas with radial currents up to 0.05 m s^{-1}, qualitatively consistent with the results of the data-assimilating shallow-water tidal model of Erofeeva et al. (2003). Observed O1 currents in this area are up to 0.04 m s^{-1}. Radial current amplitudes from YHL and WIN over the shelf near 44.5°N differ. The K1 and O1 tidal currents are north-south polarized but better aligned with the radial direction of the WIN radar. The strongest K1 and O1 radial velocity amplitudes are observed near Cape Blanco (see Figures 3.2c and 3.3c), where K1 amplitudes are in excess of 0.08 m s^{-1} and O1 amplitudes are up to 0.05 m s^{-1}.

Areas of intensified O1 tidal currents observed by the HF radars generally repeat those of K1, with smaller amplitudes (cf. Figures 3.2a-c and 3.3a-c). An exception is the shelf area north of 44.7°N sensed by the YHL instrument (cf. Figures 3.2a and 3.3a), where K1 currents are amplified and O1 currents are not. Similarly, in the region offshore of the 200-m isobath between 42.7-45.2°N, the observed K1 amplitudes (Figures 3.2abc) are much larger than O1 (Figures 3.3abc). Perlin et al.

(2004) find large diurnal variability in wind stress in these areas, and thus we suggest diurnal wind variability contributes here to the diurnal variability in currents.

To compare the model solution to HF radar observations, model surface current velocities are interpolated to HFR observation locations, projected in the direction of HF radials, high- pass filtered, and then harmonically analyzed with T_TIDE. We first consider model cases forced with daily-averaged wind fields (Figures 3.2d-f and 3.3d-f). Harmonic amplitudes of the model and HF radar K1 and O1 velocity radial components qualitatively agree with each other. Model K1 amplitudes also agree with the model results of Erofeeva et al. (2003). In the coastal region north of 44.7°N and offshore region south of 45.2°N, where observed increased diurnal variability in K1 estimates may possibly be driven by the atmospheric forcing (Figures 3.2abc), the modeled K1 currents are small (see Figures 3.2def). Since the diurnal variability is removed from the model wind forcing, finding that model amplitudes are weaker than observed amplitudes is also consistent with the hypothesis of atmospherically-driven diurnal surface velocity variability in these two areas. As an additional indication, modeled O1 amplitudes in the above-mentioned locations agree with observations (cf. Figures 3.3a and d, b and e, c and f).

To further test the hypothesis of atmospherically-driven diurnal surface velocity variability, we have computed a solution forced with high-frequency (hourly) winds. The mean wind stress field, June-August 2002, is shown in Figure 3.4a and the mean difference in wind stress between 8 pm local evening (03:00 UTC) and 11 am

local morning (18:00 UTC) in Figure 3.4b. Wind stress magnitudes near Heceta Bank vary by up to a factor of 3 over the course of a day, from 0.02 N m^{-2} to 0.07 N m^{-2}.

K1 model radial component amplitudes using the high-frequency wind solution are shown in Figures 3.2ghi. Between 42.7-44.3°N and 44.5-45.2°N, larger model amplitudes are found offshore of the 200-m isobath than in the case with daily-averaged winds, in better agreement with HF radar observations. Amplitudes are also larger over the shelf north of 44.7°N and south of 43.9°N. Curiously, at approximately 44.4°N, the high-frequency wind solution has near-zero K1 amplitude (Figure 3.2h) while the both the HF radar (Figure 3.2b) and the daily- averaged wind solution (Figure 3.2e) have local maxima in K1 amplitudes. It is possible that surface flow generated by diurnal wind variability near 44.4°N opposes tidal currents in that area. Perlin et al. (2004) showed that in a number of atmospheric models, accuracy of wind variability in the diurnal band may be limited. Despite the inconsistency between observed and modeled K1 estimates from HF radar at the WIN location, we may conclude that the surface current response to the diurnal wind variability may explain observed variability in some parts of the coastal ocean off Oregon.

The high-frequency wind solution was also analyzed at the O1 frequency and results (not shown) were similar to the O1 analysis of the daily-averaged wind solution.

HF radar data and model results were similarly analyzed for the P1 and Q1 frequencies. Amplitudes were less than 0.02 m s^{-1} and greatest over the Heceta Bank area and the tip of Cape Blanco.

4. Sensitivity of the Model Diurnal Tide Estimates to Ocean Background Conditions

To gain additional perspective on diurnal tides over the entire Oregon shelf, the root mean square K1 tidal current amplitudes RMSA = $\sqrt{(|\tilde{u}|^2 + |\tilde{v}|^2)/2}$ are computed over the shelf area between 41.5-45°N; here $\tilde{u}$, $\tilde{v}$ are harmonic constants of high-pass filtered modeled surface currents computed using time series for June and July 2002 (Figure 3.5). Diurnal velocity RMSA is found to be very sensitive to details of the background ocean state.

In case TW (forced by atmospheric fields and tides in combination, Figure 3.5a), elevated RMSA is found over the long portion of the Oregon shelf (41.7-44.7°N). Areas of particularly intense RMSA are qualitatively consistent with the results of the HF radar current analysis, described above. The RMSA is largest in the close vicinity of Cape Blanco, reaching 0.18 m s^{-1}.

To test sensitivity of the K1 tidal velocity to the background ocean conditions, we run case TONS (forced by tides only, no stratification) for 20 days and obtain surface velocity harmonic constants by harmonically analyzing (with T_TIDE) the last 16 days. The RMSA plot corresponding to this case (Figure 3.5b) reveals strikingly lower amplitudes than case TW over the entire shelf (including areas north and south of Cape Blanco and the Heceta Bank complex). The only significant area of intensification is at the shelf break between 44-44.5°N (the west edge of Heceta Bank). Case TOS (forced by tides only applied to a stratified ocean) is run and processed identically to case TONS. It reveals larger amplitudes than case TONS, but

not as large as case TW (Figure 3.5c). An exception is the area near and north of Cape Blanco, where additional analysis (not shown) reveals the presence of a tidal mixed front along the inner shelf. The associated alongshore geostrophic current is advected by the cross-shore tidal currents, which contributes to larger RMSA in harmonically analyzed velocity time series. Such a front is not normally formed under time-varying background conditions responding to upwelling- and downwelling-favorable winds, and is thus absent from case TW.

Erofeeva et al. (2003) associated intensified tidal velocity amplitudes at the edge of the Heceta Bank with coastal trapped waves at diurnal frequencies, based on the numerical eigenvalue analysis of the shallow water equations over the alongshore uniform bathymetry (using a bathymetric profile from Heceta Bank). Here, we provide similar analysis using the bathymetric profiles at 42.8°N (Cape Blanco) and 44.2°N (Heceta Bank), in the regions of larger RMSA. Additionally, we analyzed the section at 43.4◦N, between Cape Blanco and Heceta Bank. In these computations, a rigid-lid shallow-water model (Brink 1982; Chapman 1983) is utilized. The model variables are assumed to vary proportionally with $\exp[i(\omega t - ly)]$, where l is the alongshore wave number component. Dispersion curves for each profile's first wave mode, showing angular frequencies ω/f (normalized by the Coriolis frequency) as functions of l, are presented in Figure 3.6a (and corresponding bathymetric profiles in Figure 3.6b). The dispersion curve for Heceta Bank (44.2°N, Figure 3.6a, thin black line) crosses the horizontal dashed lines corresponding to the K1 and O1 frequencies, indicating that coastal trapped waves in an unstratified ocean can exist at this location at the diurnal tide frequencies. The dispersion curve for the Cape Blanco profile

(42.8°N, Figure 3.6a, thick gray line) nearly reaches the O1 frequency, but does not reach the K1 frequency. Dispersion curves computed for the gentler slopes south (not shown) and north (Figure 3.6a, thick black line) of Cape Blanco show maximums at frequencies much less than diurnal. These are consistent with the generally low K1 RMSA south of Heceta Bank in case TONS.

The effect of stratification on the dispersion properties of coastal trapped waves was discussed by Chapman (1983), who showed that with increasing stratification the ascending branch of the dispersion curve (at low wave numbers) is moved toward higher frequencies (i.e., closer to the diurnal frequencies). Although we do not repeat this analysis here, it is likely that the dispersion curve for 42.8°N that reached the O1 frequency would rise, reaching the K1 frequency in case TOS, permitting coastal trapped waves that would contribute to differences in RMSA between cases TOS and TONS.

To verify basic properties of the diurnal tide as a coastally trapped wave, barotropic (depth-averaged) K1 model tidal currents (case TW) are decomposed into counterclockwise (CCW) and clockwise (CW) rotary components, $(\tilde{u} \pm i\tilde{v})/2$ (Pugh 1987). Their amplitude and phase are shown in Figure 3.7. The coastal trapped wave on the Oregon shelf is characterized by CW velocity rotation and south-to-north phase propagation. In figure 3.7, CW amplitudes are generally large where RMSA is large and CCW amplitudes are small everywhere, except around several large capes. Within a few kilometers of Cape Blanco, horizontal barotropic current ellipses are linearly polarized, with the direction of velocity vector rotation poorly defined. There, maximum CCW and CW amplitudes are approximately equal, close to 0.10 m s^{-1}.

The CW rotary current phase shows northward wave propagation over the shelf in large regions between 42.5-43.75°N and 44-44.75°N. Between 42.5-43.75°N, the K1 wavelength is about 165 km. Between 44-44.75°N (Heceta Bank), the K1 wavelength is about 250 km.

For the O1 constituent (not shown), the CW rotary current shows patterns of coastal trapped waves similar to K1. O1 CW rotary current amplitudes at Heceta Bank and Cape Blanco are up to 0.04 m s^{-1} and 0.08 m s^{-1}, respectively.

5. Intensified Diurnal Tides Near Cape Blanco

Data from the HF radar located at the tip of Cape Blanco confirm extreme velocities at diurnal frequency very close to the cape. Figure 3.8 shows a 50-day time series during June-August 2002 of high-pass filtered HF radial component velocity (generally in the north-south direction), both observed (black) and modeled (gray), at a point off Cape Blanco (marked in Figure 3.9). The chosen location is at the closest radial distance sampled by the instrument. Here, observed radial speeds may exceed 0.3 m s^{-1}. Modeled currents are somewhat larger; the RMS amplitudes of the model and HFR time series are 0.17 m s^{-1} and 0.15 m s^{-1} , respectively.

The model K1 amplitudes increase toward the tip of the cape, so it is possible that diurnal tidal currents might exceed 0.3 m s^{-1} closer to the cape. The model predicts the phase of diurnal oscillations remarkably well, and also predicts variability in diurnal current amplitudes. These are generally largest when K1 and O1 are in phase, e.g., during episodes of diurnal spring tides. The period of the diurnal spring-

neap cycle is 13.58 days, about 1 day less than the 14.88 day period of the M2-S2 spring-neap cycle.

Events of intensified M2 tide may also be identified in this area. These are intermittent, associated with internal tide motions, and less predictable than diurnal tides. An area of strong barotropic-to-baroclinic M2 tide conversion on the continental slope, 60 km to the southwest of the cape (see Figure 2.13) may be influencing circulation here. Still, oscillations evident in Figure 3.8 are predominantly diurnal.

The presence of a narrow alongshore coastal jet in the vicinity of this point potentially affects tidal speeds due to advection of the jet by the cross-shore tidal component. To provide a crude estimate of the significance of this effect, let (u,v) be the orthogonal (cross-shore and alongshore) surface tidal velocity components. Let us assume that these evolve in presence of the steady alongshore background jet $V(x)$. Then the linearized momentum equation would include the u-V advection term: $v_t = -uV_x + \ldots$, where subscripts denote partial derivatives with respect to time t and the cross-shore coordinate x. The magnitude of this term is estimated using model outputs on June 26, when both the model and the HF radar show intensified diurnal currents near Cape Blanco (see Figure 3.8). During this time, the K1 and O1 tides are in phase. In Figure 3.9, we show the modeled average (subtidal) alongshore surface current (vectors), the magnitude of the average meridional component V (color), and the amplitude of the u (zonal) component of surface diurnal tide currents (the K1 and O1 constituents combined, black contours). The tidal amplitude estimates have been obtained by harmonic analysis of the 5-month model time series (April-August). The

location where velocities (shown in Figure 3.8) are sampled is marked by the star. The alongshore velocity in the jet changes between 0.25 and 0.5 m s^{-1} over a distance of 5 km; the corresponding shear is $V_x = 5 \times 10^{-5}$ s^{-1}. The cross-shore advection by the diurnal tidal current with an amplitude of $u = 0.07$ m s^{-1} will provide a contribution to the tidal v amplitude of $uV_x/\omega = 0.05$ m s^{-1}. So, near the cape, this mechanism may contribute to 20-30% of the observed intensified diurnal signal near the cape. The rest may be attributed to the coastal trapped waves and topographic effects.

The same scaling estimates may be applied to other areas of the shelf, in particular, the wide Heceta Bank shelf area. Here case TOS yields K1 amplitudes near 0.02 m s^{-1} and case TW near 0.05 m s^{-1}. The 0.03 m s^{-1} increase in the amplitude may be explained easily as the effect of the advection of the upwelling jet by the diurnal tidal current. The HF radar (see Figures 3.2 and 3.3) senses the diurnal tide influenced by this advection.

In addition to being a site with strong tides, Cape Blanco is a separation point for the equatorward coastal jet (Barth et al. 2000; Koch et al. 2010; Kurapov et al. 2011). Energetic tides here may contribute to eddy dynamics and modify cross-shelf transport. Figure 3.10a shows time series of the model-derived relative vorticity (vertical component) normalized by the Coriolis parameter, $f^{-1}(\partial v/\partial x - \partial u/\partial y)$ (where u and v are full surface currents), in cases TW (gray) and WO (black) sampled at the same point as above (see also map in Figure 3.10c) and plotted for the entire model run. Case TW shows periodic high-frequency variability in normalized vorticity with peak values exceeding 2, suggesting strongly non- linear flows. Vorticity spectra

(Figure 3.10b) confirm that case TW (gray) has more power at higher frequencies than case WO (black), with peaks appearing at one and two cycles per day, corresponding to diurnal and semi-diurnal tides. Also, the Coriolis-normalized vorticity in case TW shows spatio-temporal variability not seen in case WO. As an example, we show instantaneous maps of vorticity every 6 hours on April 20, 2002 (Figure 3.11). On this date, the location of frontal structures in cases TW and WO are still similar (after a 20-day spin- up from the same initial conditions). Both cases show large vorticity near Cape Blanco, but the tide acts to fundamentally change the model kinematics. In the vicinity of Cape Blanco, the diurnal tide may displace the jet (identified by the patch of large positive vorticity) by as much as 10 km over one tidal cycle (see Figure 3.11, left). In comparison, the vorticity field in case WO is relatively steady during this time period (Figure 3.11, right). Additional studies will be needed to describe this tidal modulation in more detail and understand mechanisms that may influence jet separation at Cape Blanco and other large capes along the US West Coast (Strub et al. 1991).

6. Summary

Analyses of HF radar surface current data confirms areas of intensified diurnal tidal currents along the Oregon coast. In the vicinity of Cape Blanco, where observed diurnal currents exceed 0.3 m s^{-1} , the currents may be a combination of coastal trapped waves and advection of the subtidal, wind-driven coastal jet by the tidal

currents. The latter mechanism may contribute more than 50% to the diurnal tide current amplitudes over the wider part of the Oregon shelf (Heceta Bank complex).

Our study reveals the effect of the linearized advection on diurnal current amplitudes at the surface, on average over the summer season. In future studies, it would interesting to learn how this effect extends through the water column, and whether changes in the strength of the subtidal current influence diurnal current amplitudes on temporal scales of days to seasonal.

Diurnal wind variability also contributes to elevated diurnal surface current amplitudes, in particular, in areas where the strong upwelling jet is found. It is possible that atmospherically-driven diurnal ocean variability in the area of the jet is also in part determined by the advection of the alongshore coastal jet by wind-driven diurnal motions.

The 1-km resolution model describes diurnal tide variability in the vicinity of Cape Blanco qualitatively correctly and accurately predicts the timing of intensified diurnal tide events. These come during periods of the diurnal spring tide, when the K1 and O1 tides are in phase. Variability in the ocean response from one spring tide period to another may be affected by intermittent semi-diurnal internal tides and the intensity of the coastal jet. The ocean model also identifies areas of locally intensified diurnal tidal currents in the vicinity of a number of smaller capes. Additional studies will be needed to understand details of three-dimensional tidally-driven circulation around Cape Blanco, as influenced by headland topography (e.g., Signell and Geyer 1991; Geyer 1993; McCabe et al. 2006).

Strong tidal modulation of surface currents in the vicinity of the capes may affect material transports, in particular larvae dispersion. Areas of high larvae retention rates have been proposed as Marine Protected Areas. Numerical simulations of larvae dispersion (e.g., Kim and Barth 2011) should account for tidal variability to more accurately predict particle movement and retention in shallow coastal environments.

3.8 Acknowledgments.

This research was supported by the National Science Foundation (Grants OCE-0000734, OCE-0648314, and OCE-1030922), the Office of Naval Research Physical Oceanography Pro- gram (Grants N000140810942 and N000141010745), National Oceanic and Atmospheric Ad- ministration (NOAA) grant NA11NOS0120036, NOAA-CIOSS, and NOAA-IOOS (NANOOS). The authors thank J. A. Barth, M. S. Hoecker-Martinez, R. M. Samelson, and S. H. Suanda for their helpful discussions.

3.9 Figures

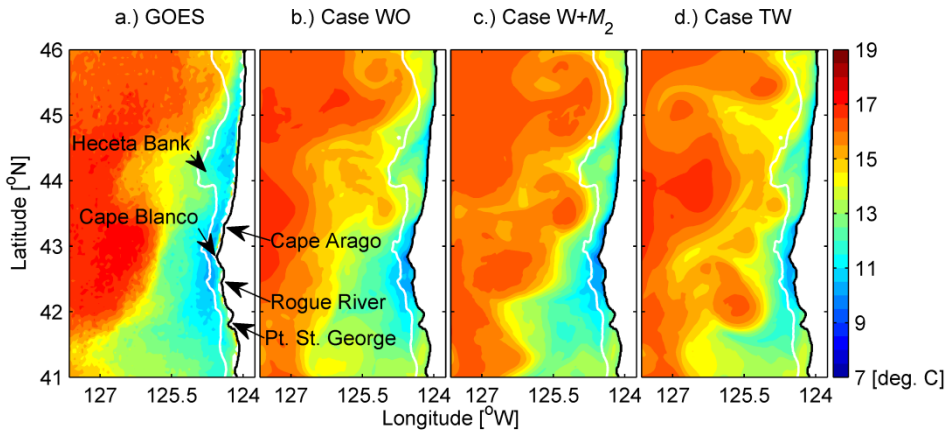

Figure 3.1 August 2002 mean sea surface temperature: (a) GOES satellite observations (Maturi et al. 2008), (b) ROMS model forced by winds only ("case WO"), (c) ROMS model forced by winds and the M2 tide ("case W+M2"), and (d) ROMS model forced by winds and eight tidal consituents ("case TW"). White lines mark the 200-m isobath. Selected geographical features are indicated.

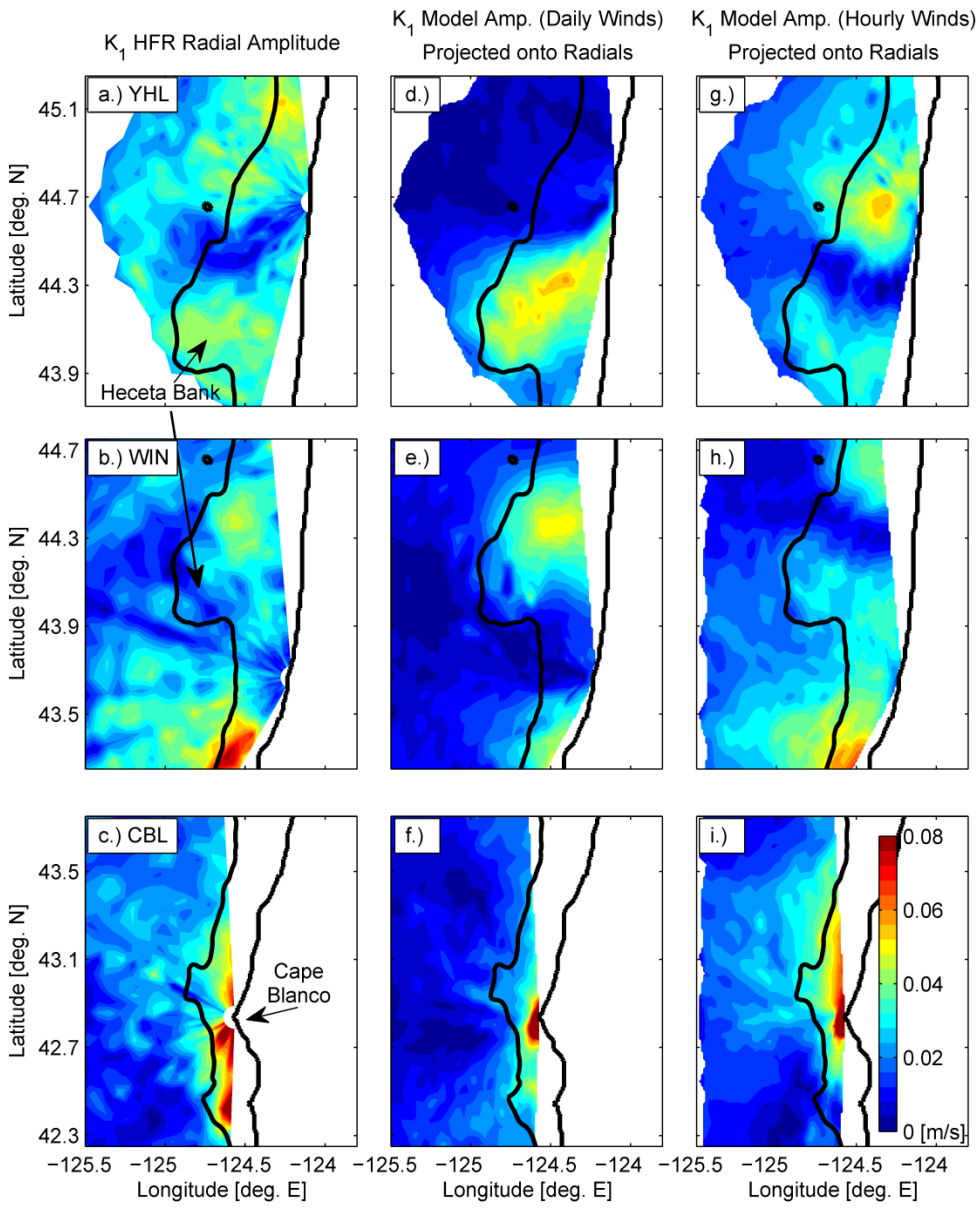

Figure 3.2 Tidal amplitudes (in m s^{-1}) of K1 surface current radial amplitudes from HF radars (left), model forced with daily-averaged winds (center), and high-frequency (hourly) winds (right). Top panels are for the YHL radar, middle panels for the WIN radar, and bottom panels for the CBL radar. YHL ob- servations are from June and July 2008, the first year such observations are available. WIN and CBL observations are from June-August 2002, the same year as the model. Black lines mark the 200-m isobath and the coast.

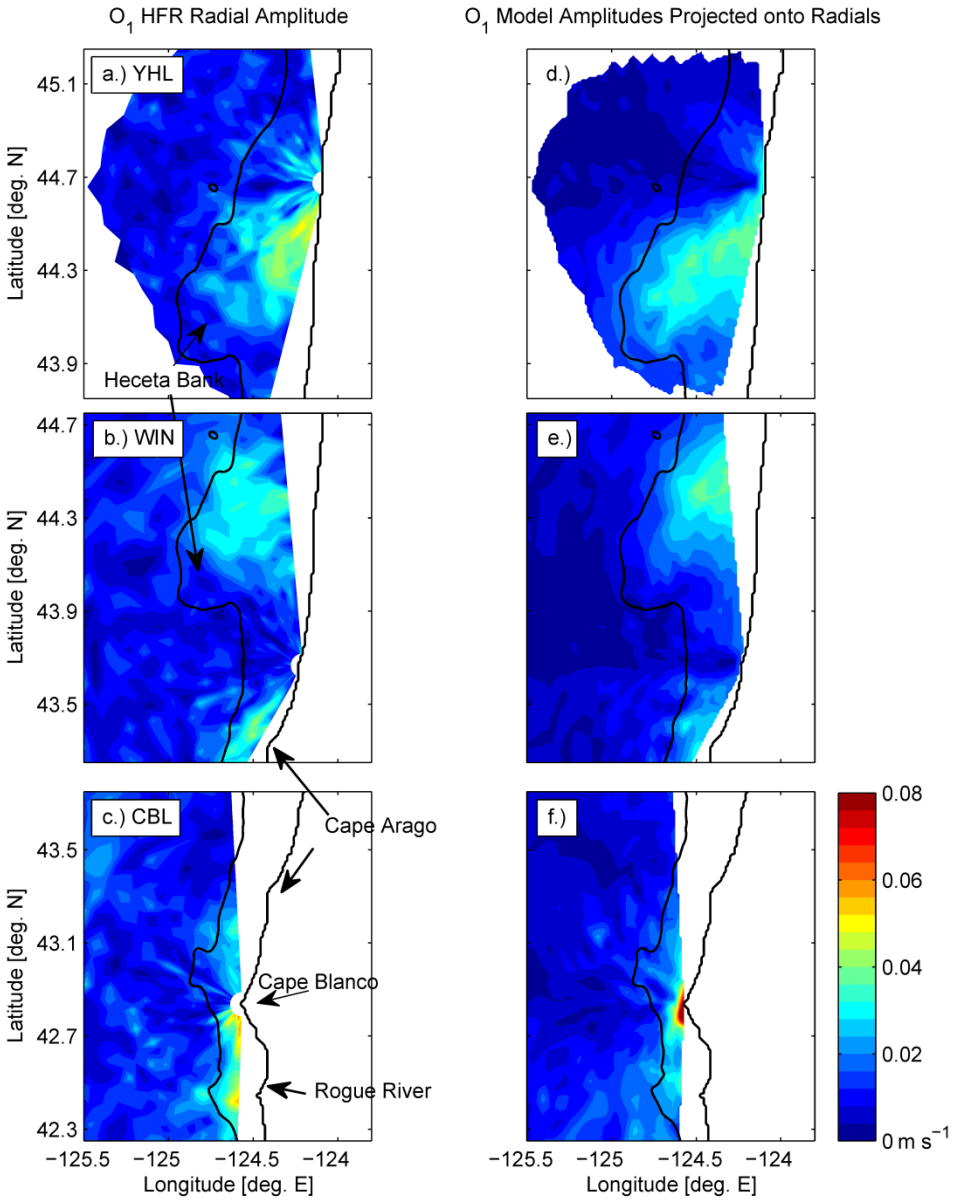

Figure 3.3 As in Figure 2, but for O1 currents. Tidal amplitudes (in m s^{-1}) of O1 surface current radial amplitudes from HF radars (left) and daily-averaged wind model (right). Top panels are for the YHL radar, middle panels for the WIN radar, and bottom panels for the CBL radar. YHL observations are from June and July 2008, the first year such observations are available. WIN and CBL observations are from June-August 2002, the same year as the model. Black lines mark the 200-m isobath and the coast.

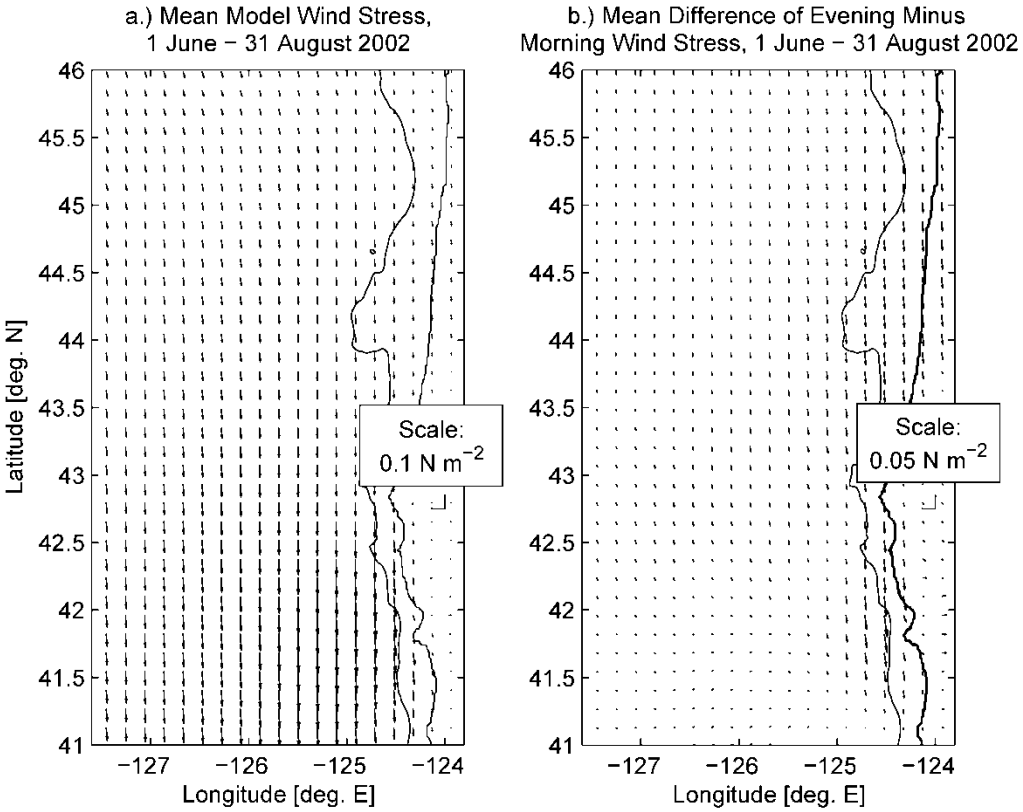

Figure 3.4 (a) Mean model wind stress, 1 June - 31 August 2002. (b) Mean of the differences of local evening (03:00 UTC) and local morning (18:00 UTC) wind stress, 1 June - 31 August 2002. Note the difference in scales. The 200-m isobath and coast are contoured.

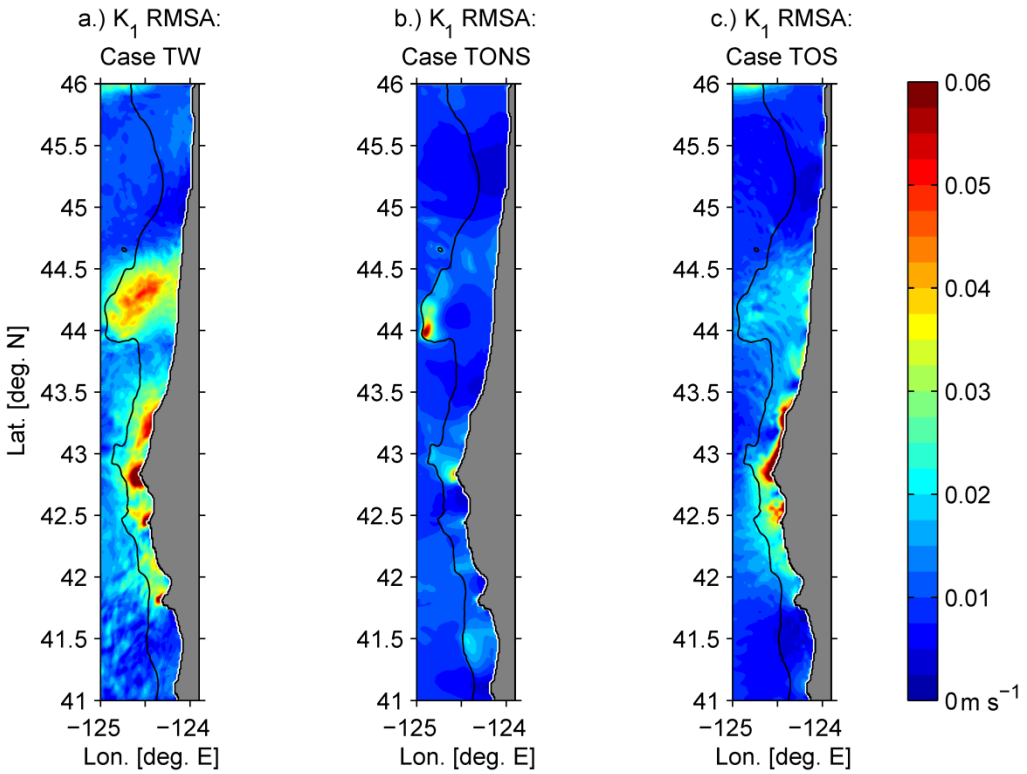

Figure 3.5 From left to right: (a) *K*1 RMSA in case TW, (b) *K*1 RMSA in case TONS, and (c) *K*1 RMSA in case TOS. In all panels, the black line marks the 200-m isobath.

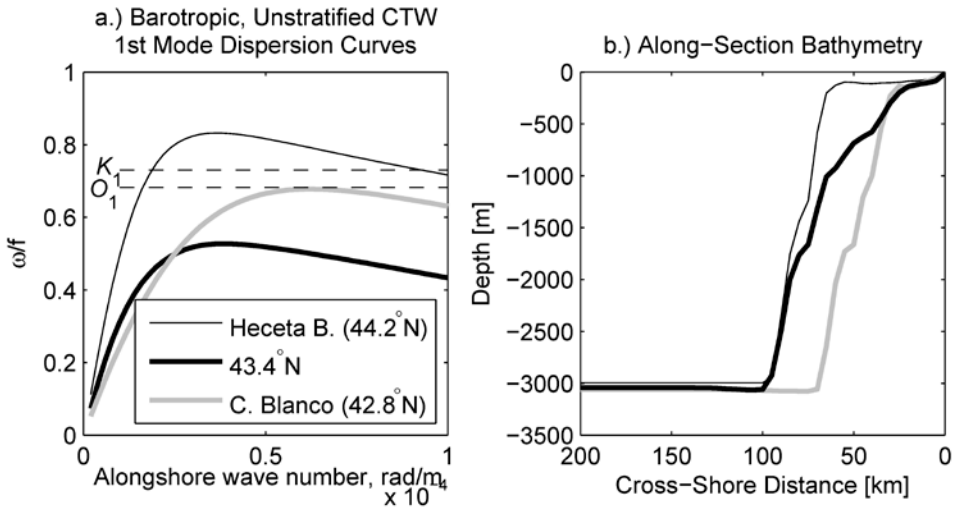

Figure 3.6 (a) Dispersion curves for the first mode coastal trapped waves at Heceta Bank (44.2°N, thin black line), 43.4°N (thick black line), and Cape Blanco (42.8°N, thick gray line). Dashed black lines indicates the Coriolis-normalized K1 and O1 tidal frequencies. (b) Bathymetry along those sections. Note that for eigenvalue analysis, bathymetry has been artificially flattened in the abyssal plane.

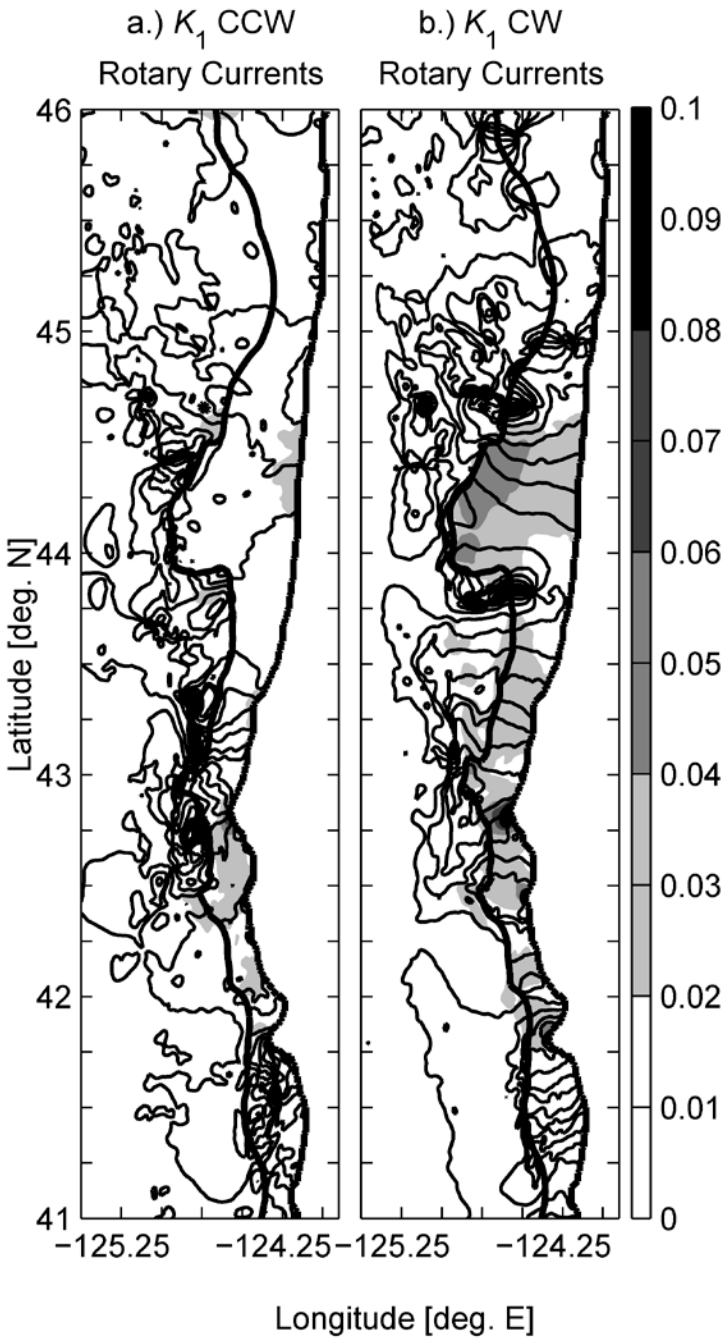

Figure 3.7 (a) Counterclockwise depth-averaged K1 rotary currents from case TW. (b) Clockwise depth-averaged K1 rotary currents from case TW. In both panels, the thick black lines mark the 200-m isobath and the coast, while the thin black lines mark rotary current phase (every 30°) and the shading marks rotary current amplitude.

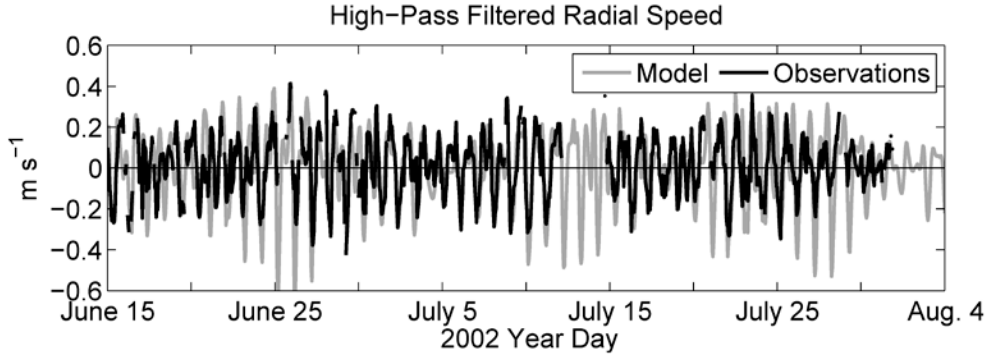

Figure 3.8 Time series of HFR-observed (black) and model (gray) radial velocity component near Cape Blanco (location marked in Figure 10).

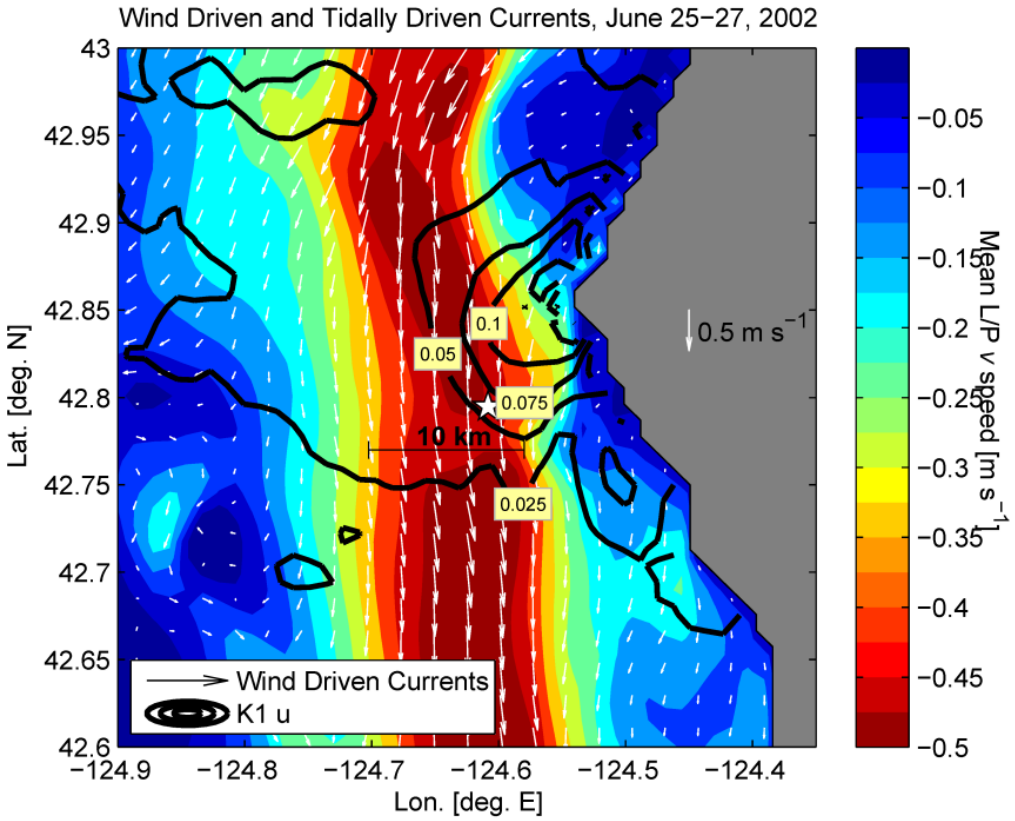

Figure 3.9 Color field: 40-hour low-pass filtered v from 23:00 UTC June 26. Black contours: K1+O1 *u* (which are in phase during June 25-27) at 0.025 , 0.05, 0.075, and 0.1 cm s^{-1}, as computed from high-pass filtered, harmonically analyzed currents for April, May, June, July, and August 2002. The star marks the location of the HFR time series in Figure 3.8.

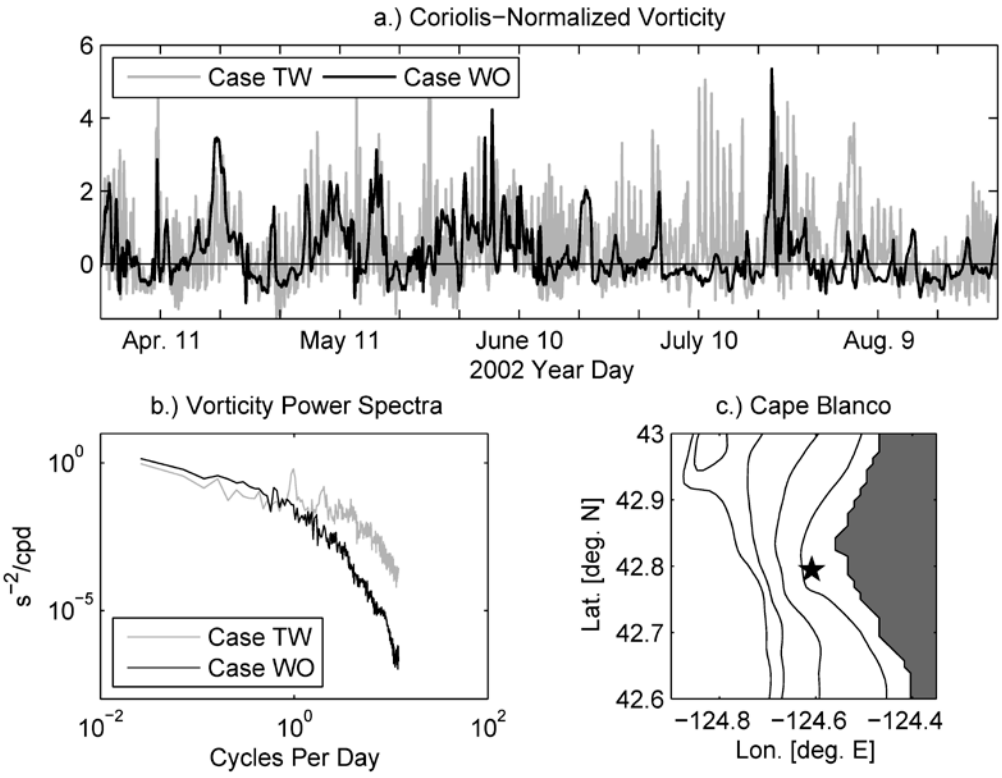

Figure 3.10 (a) Time series of Coriolis-normalized relative vorticity (vertical component) from case case TW (gray) and WO (black) at the point marked with the star in panel c. (b) Spectra of vorticity time series from case TW (gray) and case WO (black), as computed from the entire model run. (c) Close-up of Cape Blanco region. Star marks the location of the time series in Figure 7 and this figure. Black lines mark the 50-, 100-, 150-, and 200-m isobaths.

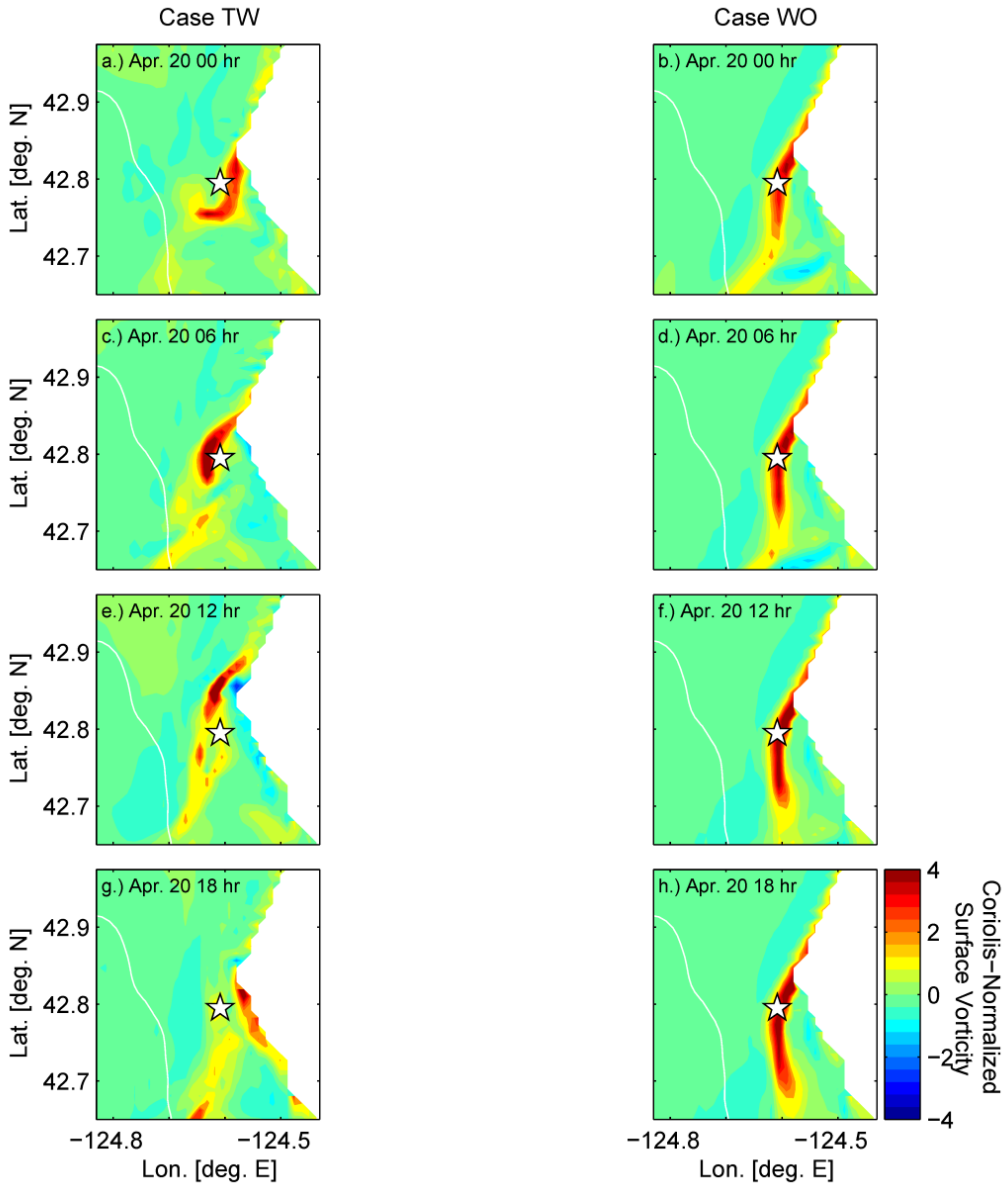

Figure 3.11 Instantaneous modeled Coriolis-normalized surface relative vorticity during April 20, 2002 for case TW (left) and case WO (right). Horizontal image pairs (i.e., a and b, c and d, e and f, g and h) are at the same time for the two cases. Image pairs are separated by six hours (i.e., c and d are two hours after a and b).

4. Dispersion of the California Undercurrent by Internal Tide Motions

J. J. Osborne, A. L. Kurapov, G. D. Egbert and P. M. Kosro

In preparation

4.1. Introduction

The California Undercurrent (CUC) is a poleward slope flow along the eastern boundary of the North Pacific Ocean. It is identified in observations over the continental slope below the main pycnocline (Hickey 1979) and is typically 10-20 km wide. The northward transport associated with the CUC is estimated as 0.5-1.5x106 m3 s-1 (Hickey 1979, Pierce et al. 2000). To the Oregon slope, it brings relatively warmer and saline waters of subtropical origin (Hickey 1979, Thomson and Krassovski 2010). It varies seasonally, usually intensifying by the end of the upwelling season (Collins et al. 2003). During summer, the CUC is capped by a southward surface current driven by upwelling-favorable winds (e.g., Huyer 1976, Smith 1981, Allen et al. 1995, Federiuk and Allen 1995). During winter, predominantly northward winds drive downwelling and a northward surface-to-bottom current along the shelf break. The undercurrent is hard to identify during this time. The wintertime northward surface-to-bottom flow is sometimes called the Davidson Current (Hickey 1979). The CUC is not always continuous; it can turn off-shore, separate, and form anti-cyclonic eddies (Garfield et al. 1999, Pierce et al. 2000, Kurian et al. 2011).

Forcing mechanisms for the CUC and other eastern boundary poleward undercurrents are not entirely understood. Proposed mechanisms have been classified into three categories (Hill et al. 1998), including a response to wind stress curl (e.g. McCreary 1981, Marchesiello et al. 2003), the alongshore pressure gradient (e.g.

Wang 1982; Huthnance 1984, 1985; Choboter 2005), or rectification of flow over topography (Haidvogel and Brink 1986, Holloway 1987; Holloway et al. 1989).

CUC waters contain relatively less dissolved oxygen than subarctic waters farther north (Hickey 1979, Thomson and Krassovski 2010). The CUC affects nutrient concentrations along its path due to its low nitrate-phosphate ratio (Liu and Kaplan 1989, Castro et al. 2001). This in turn can affect marine organisms such as zooplankton (Swartzman et al. 2005) and further influence higher trophic levels. As the CUC contributes to source waters for summer upwelling (MacFadyen et al. 2008), understanding mechanisms by which CUC waters enter the shelf can be important for local biology.

Wind-driven upwelling has been established as the primary forcing of on-shore flow near the bottom (e.g. Garrett et al. 1993), but the contribution of internal tides to cross-isobath dispersion of CUC waters and resulting slope-shelf material exchange has not been studied. We hypothesize here that internal tides may provide an important contribution to on-shelf transport of slope undercurrent waters. The proposed mechanism is explained with the help of Fig. 4.1. Consider fluid particles in the undercurrent, passing a chosen point near bottom, e.g., at 300 m isobath. As particles flow along the slope, the tide moves them up and down the slope. This oscillatory motion, plus mixing over the shelf and asymmetry in the bottom boundary layer response to upslope and downslope motions, adds randomness to fluid particle trajectories. As in a random walk model (Pearson 1905), the standard deviation of particle cross-shore displacements from their original depth would increase with time.

Without the perturbation, we would expect that these particles move to the north and remain close to the original depth.

In a three-dimensional coastal ocean model, it is possible to release a passive tracer at a point on slope and analyze the tracer's cross-isobath dispersion as it moves with the undercurrent. In a case without tides, we would hypothesize the undercurrent waters would have smaller dispersion than in a case with tides.

To investigate this, the 1-km resolution model by Osborne et al. (2014) is utilized. For model details see section 4.2. The internal tides in an area of relatively straight slope (between Cape Blanco and Heceta Bank) and the structure of the undercurrent in August 2002 are analyzed in section 4.3. Results of passive tracer experiments are explored in section 4.4. Conclusions are presented in section 4.5.

4.2 Model

The model set-up utilized here is similar to that in Osborne et al. (2014). It is based on the Regional Ocean Modeling System (ROMS), a non-linear, hydrostatic, Boussinesq, primitive equation model featuring terrain-following coordinates in the vertical and advanced numerics (Shchepetkin and McWilliams, 2005). The significant difference between the previous model of Osborne et al. (2014) and the solutions presented here is that we presently use the multidimensional positive definite advection transport algorithm (MPDATA; e.g., Smolarkiewicz 1983, 1984, 1998). MPDATA is a second-order accurate, positive-definite, and conservative finite method for fluid tracer fields. A numerical experiment in which the tracer is released

at a point is an example of advecting a non-negative field with very sharp gradients. Our initial attempt to simulate tracer release without the MPDATA option in ROMS resulted in noisy solutions. To suppress this noise, we use MPDATA. However, it is more diffusive than ROMS' other advection schemes, making it more difficult to discern the impact of tides on tracer propagation (i.e., comparison of cases with and without tides, section 4.4).

Solutions discussed are obtained using realistic bathymetry, initial conditions, boundary conditions, and surface forcing (see Osborne et al. 2011, 2014). The domain is from 127.6°W to 124°W and 41°N to 46°N, approximately 300 km by 550 km, with the eastern edge of the domain at the Oregon coast. Resolution is approximately 1 km in the horizontal and with 40 levels in the vertical. The vertical levels are configured to provide relatively higher resolution near the surface and bottom (by choosing ROMS parameters as θ_s = 5, θ_b = 0.5, thermocline = 50 m, Vtransform = 1, and Vstretching = 1). Bathymetry is a combination of a 12"-resolution National Oceanic and Atmospheric Administraion (NOAA)-National Geophysical Data Center bathymetry product and a lower-resolution ETOPO5 5' gridded bathymetry (NOAA 1988). A minimum depth of 10 m is set along the coast.

Atmospheric forcing is obtained using the COARE bulk flux formulation (Fairall et al. 1996a,b), in which we utilize daily-averaged wind speed from the Coupled Ocean-Atmosphere Mesoscale Prediction System (COAMPS, Hodur 1997) and monthly averaged short-wave radiation, surface air temperature, relative humidity, and cloud cover from the National Centers for Environmental Prediction's reanalysis solution (Kalnay et al. 1996).

Subtidal boundary conditions are obtained from a 3-km resolution regional ROMS model (Koch et al., 2010). Tidal forcing (free surface elevation and barotropic velocity from a US West Coast data-assimilating 1/30°-resolution (Egbert and Erofeeva 2002, http://volkov.oce.orst.edu/tides/)) is applied at the boundary at every time step; no tidal forcing is applied to interior points. Tidal forcing includes 8 constituents (from the shortest to the longest period: K2, S2, M2, N2, K1, P1, O1, Q1). The base case ("case TW") includes both tidal and atmospheric forcing and is run for 5 months, starting on 1 April 2002. Because of limited predictability of energetic coastal flows (particularly near the end of summer, Kim et al. 2009), details of mesoscale circulation in the coastal transition zone (CTZ, just offshore of the shelf) differ in this solution and the solution run without tides (a "winds-only case" WO), by the end of the 5-month run (even though they started from the same initial conditions). Eddy variability in the CTZ may affect the structure and continuity of the undercurrent. To fairly compare cases with and without the tides in August (when the undercurrent is strongest in our model), an additional case was run, using a de-tided TW solution for 0000 UTC 31 July 2002 as the initial condition. This case is run for a period of about 1 month (to 0000 UTC 2 September 2002). Unless said specifically, this solution (obtained after the re-start with initial conditions identical to those from TW on July 31) will be referred to as case WO.

Barotropic velocity is defined here as the depth average and is indicated with a subscript 1. Baroclinic velocity is the deviation from the depth-averaged current and indicated with a subscript 2.The slope is the region between the 2000- and 200-m isobaths and the shelf is the region between the 200-m isobath and the coast. Subtidal

quantities are obtained by applying a 40-hour low-pass filter (Beardsley et al. 1985). These are denoted $\langle q \rangle$. High-pass filtered quantities are $q'(\boldsymbol{x}, t) = q(\boldsymbol{x}, t) - \langle q(\boldsymbol{x}, t) \rangle$, the total less the low-pass filtered part.

4.3 Ocean variability on the slope between Cape Blanco and Heceta Bank

To study the effect of internal tides on cross-slope dispersion of the CUC waters, an area must be found where both are present and relatively strong. Simple bathymetry, with few along-coast variations, is also preferred, as dynamics will be more two-dimensional, easing analysis. Such a region is found between 43.2°N and 43.8°N (north of Cape Blanco and south of the Heceta Bank complex). Here, we find relatively large onshore depth-integrated tidally-averaged M2 baroclinic energy flux across the 200-m isobath, up to 50 W m^{-1} (see Fig. 2.13; Osborne et al., 2011).

To provide additional information about the strength of the modeled internal tide (i.e., case TW) in this area, we discuss cross-shore (zonal) high-pass filtered baroclinic internal tide velocities (u'_2) at 43.75N. Fig. 4.2 shows the cross-shore section of the root-mean-square magnitude (with respect to time) of u'_2 at 43.75°N between 12:00 UTC 2 Aug 2002 and 12:00 UTC 29 August 2002. Near the bottom over the upper part of the slope, between 124.7°W and 124.5°W, the u'_2 RMS value is relatively large, between 0.03 and 0.04 m/s. The surface u'_2 RMS value is up to 0.07 m/s. Bottom u'_2, shown as a function of longitude and time (Fig. 4.3) reveals periods of weaker and stronger baroclinic semi-diurnal tides. At the peak periods,

these may reach 0.15-0.2 m/s. Attempts were made to connect spring-neap variability in barotropic tides to internal tide activity in this area, but no obvious or simple connections have been found.

Peak u'_2magnitudes, may be larger in June-July than in August. Nevertheless, we choose to perform analyses with the passive tracer in August because the CUC is observed to become stronger over the summer season, and August is the last month of our simulation.

Next we analyze the model cross-shore hydrographic structure in several transects to identify the California Undercurrent (CUC). CUC waters are relatively warmer and saltier than the subarctic waters at the same densities. Here we attempt to identify the CUC by its time-averaged alongshore (meridional) current and spiciness (e.g., Flament 2002). Spiciness may be defined as "orthogonal" to density in a T-S diagram. Due to its origins far to the south, the California Undercurrent is observed to have relatively high spiciness compared to surrounding waters (e.g, relatively warmer and saltier than surrounding waters). Fig. 4.4 shows August 2002-averaged cross-shelf sections of the spiciness (color) and the meridional current (contours) at five latitudes between 43.2°N and 43.8°N for cases TW and WO. In terms of these quantities, the CUC is clearly visible in the model. In both cases, the meridional velocity shows a northward jet with a sub-surface maximum between 0.08 and 0.12 m s^{-1}. Locations of maximum northward slope velocity are close to locations where spice maximums are found. At the two northern sections (43.65°N and 43.8°N), the northward jet extends to the surface, with southward flowing waters on

the western, off-shore side and also on the shelf (which is indicative of a recirculation area in the southern part of Heceta Bank (Oke et al., 2002)).

Despite case WO being restarted at the end of July using the TW solution as the initial condition, solutions TW and WO diverge over the month of August. In particular, the two southern-most sections (43.2°N and 43.35°N) show the greatest meridional velocity differences in cases TW and WO. In case TW, the northward flow has greater cross-shore extent, off-shore of 125.2°W to the shelf break (approximately 124.7°W). In case WO, the northward flow is narrower. Additionally, at 43.2°N, the depth of maximum northward flow is different. In case TW, it is between 500 m and 600 m depth (not shown), while in case WO, it is at 400 m.

Across all latitudes, the spiciest water (>0) is in a thin layer (<10 m) at the surface, where surface heat flux directly impacts water properties. Below this layer we find less spicy ("mintier") water, with a minimum of -0.8. The spice signature of the CUC is below the minty layer, with a maximum of about -0.1. Over the shelf, the minty layer thins, and disappears near the inner shelf. The two model cases appear relatively similar, though case WO is spicier, especially along the 43.35°N section.

4.4 The influence of tidal motions on the cross-isobath transport of CUC Water: model experiments with passive tracer release

Based on the presence of relatively strong modeled internal tides and the undercurrent between 42.2°N and 43.8°N, we choose to re-run the model with a passive tracer released continuously at the sea floor at (124.69°W, 43.3°N), at the 300-m isobath.

This point is near the core of the CUC at that latitude. The latitude was chosen in anticipation that the tracer will flow to the north (as will be shown), through the region of strong internal tides. The tracer release starts at 0000 UTC 31 July 2002 and continues throughout August. The tracer concentration units are m^{-3}. Cases TW and WO (which have identical initial conditions on 31 July 2002) are compared. Three perspectives on tracer concentration over the shelf are considered: maps of tracer in the bottom layer of the model, vertical cross-shelf sections of tracer, and volume-integrated tracer.

Bottom Tracer

Fig. 4.5 shows tracer bottom concentrations for cases TW (left) and WO (right) averaged over 4 August 2002, 9 August 2002, and 14 August 2002 (5, 10, and 15 days after release). Similarly, Fig. 4.6 shows bottom concentrations over 19 August 2002, 24 August 2002, and 29 August (20, 25, and 30 days after release). Over the first 10 days (Figs. 4.5a-d), the tracer concentrations at the bottom are relatively similar, spreading north of the release point (magenta dot), and mostly staying between the 100-m and 500-m isobaths.

Fifteen days after release (14 August, Figs. 4.5e,f), the two cases start to show noticeable differences in bottom tracer concentrations. In case TW, the tracer patch is shorter along the path of the undercurrent (50 km vs. 75 km) and wider in the east-to-west direction (40 km vs. 25 km). Near 43.3°N, tracer is found all the way to the coast. In case WO, high concentrations of tracer are moving westward along the south flank of Heceta Bank, but virtually no tracer is found in-shore of the 100-m isobath.

Over the rest of August, bottom tracer in the two cases continues to diverge. On August 19, after 20 days of release in case TW (Fig. 4.6a), bottom tracer reaches the coast from 42.4°N to 43.7°N. In case WO (Fig 4.6b), bottom tracer hardly penetrates the 100-m isobath. Some bottom tracer in case WO is present along the west flank of Heceta Bank, a result never seen in case TW.

On August 24 and 29, in case TW, tracer at low concentrations (<10 m^{-3}) covers more of the shelf area than case WO (cf. Figs. 4.6c,e to Figs 4.6d,f), particularly inside the 100-m isobath.

We should mention that the contrast between cases TW and WO would be more striking if the MPDATA advection option were not used (not shown). Without the MPDATA option, the WO tracer path is much narrower. The MPDATA option in ROMS adds diffusivity but removes numerical noise in the tracer solution.

Tracer Vertical Cross-Shelf Sections

Tracer vertical cross-shelf sections are shown along 43.75°N (the same latitude as that analyzed in section 4.3) averaged over 5-day periods (5-9 August, days 6 through 10 of tracer release – Fig. 4.7; 10-14 August – Fig. 4.8; and 15-19 August – Fig. 4.9). More tracer is found on the shelf in case TW than WO. The tracer is distributed throughout the water column more uniformly (case TW) instead of being confined to within the bottom 50 m (case WO). In both cases, a tracer patch appears in the middle of the water column over the slope and is associated with the flow separated from the slope north of the cross-section; the recirculating flow brings the tracer back to this latitude.

Over 20-29 August, tracer in case TW reaches all the way to the coast and there outcrops at the surface (Figs. 4.10a, 4.11a). This never happens in case WO; tracer remains within the bottom 25 m or 50 m of the water column (Figs. 4.10b, 4.11b).

Volume-Integrated Tracer Concentration on the Shelf

To quantify the effect of tides on the on-shelf tracer flux, the tracer is volume-integrated over the shelf. Specifically, integration is done from the 200-m isobath to the coast, from 43.3°N to 43.9°N, and vertically from the sea floor to the sea surface. This estimate is obtained for every model snapshot (hourly) for both cases. The resulting time series, normalized by the amount of the tracer released in one day, are plotted in Fig. 4.12.

First, tidal variability is present in case TW and not in case WO. Some of this tidal variability appears diurnal in nature. Over the 144 hours (six days) from 8 to 13 August, there are 6 large spikes in case TW's shelf-integrated dye, roughly one per day. There are also five smaller spikes between the six large spikes, due to the semi-diurnal tide. From about 20 to 28 August, additional spikes are seen in case TW. Initially, these spikes alternate between large and small amplitude, as seen from 8 to 13 August, before becoming relatively consistent in amplitude around 25 August (with semi-diurnal period).

For trends in subtidal time scales, over the first half of August, the two cases increase at same order of magnitude, with case TW (black) having about 50% more tracer in the shelf area than case WO (red). Over the rest of the release period, the

amount of tracer in case TW slightly increases, but, in case WO, tracer decreases by about 50% over 17 to 27 August and then regains this amount over 27 August to 2 September. Increases and decreases in the integrated tracer amount on scales of days in both cases are associated with periods of upwelling and relaxation.

To further investigate the contribution of tidal motions to on-shore material transport, cross-shelf tracer fluxes have been computed and then averaged in space and time. Tracer fluxes are further decomposed into contributions due to slow and fast motions (similar to a Reynolds decomposition). Specifically, the following is done:

1. For each case, modeled velocities are interpolated to the 200-m isobath between 43.3°N and 43.9°N and then the component perpendicular to the 200-m isobath is found. This velocity is labeled v; it is a function of depth, time, and along-shore position.
2. The tracer concentration (q, m^{-3}) is also interpolated to the 200-m isobath between 43.3°N and 43.9°N. It is also a function of depth, time, and along-shore position.
3. v and q are each decomposed in to a time-averaged term ($\bar{v}, \bar{q}$) and a time deviation ($v_D = v - \bar{v}, q_D = q - \bar{q}$).
4. The deviations are further decomposed into low-pass filtered terms ($\langle v_D \rangle, \langle q_D \rangle$) and high-pass filtered terms ($v_D{}', q_D{}'$) using the 40-hour filter (Beardsley et al. 1985).
5. The instantaneous tracer flux can be expanded into nine terms, $vq = (\bar{v} + \langle v_D \rangle + v_D{}')(\bar{q} + \langle q_D \rangle + q_D') = \cdots$. Averaging in time over the month

of August eliminates four terms (time average times high- or low-pass filtered time deviation), leaving five terms,

$$vq = \bar{v}\bar{q} + \overline{\langle v_{\mathrm{D}}\rangle\langle q_{\mathrm{D}}\rangle} + \overline{v_{\mathrm{D}}{}'q_{\mathrm{D}}{}'} + \overline{\langle v_{\mathrm{D}}\rangle q'_{\mathrm{D}}} + \overline{v'_{\mathrm{D}}\langle q_{\mathrm{D}}\rangle},$$

namely, a product of time-averaged velocity and tracer, tracer due to slowly varying dynamics, a transport due to quickly-varying dynamics (the Reynolds term), and two cross terms. As verified below, the cross terms, while not identically zero by definition, are negligibly small. The terms in this last equation are functions of depth and along-shore position.

6. These terms are also averaged over the length of the 200-m isobath, leaving them as functions of depth alone. Results are plotted in Fig. 4.13.

In case TW, the Reynolds term is of the same order of magnitude as the transport due to the time-averaged quantities' slowly-varying dynamics. All these terms are relatively small in the upper 80 meters and have extremes in the bottom 50 m (obviously, since the tracer is released near the bottom). The transport due to the time-average term is positive, strongest on-shore at about 170 m depth, and is negative near the bottom. The slow-varying part of the flow transport tracer off shore. It is strongest at about 160 m depth and is practically 0 at the bottom. The term due to high-frequency tidal is strongest and on-shore in the bottom 50 m. The tides makes a significant contribution to on-shelf tracer transport.

In case WO, only the transport due to the means and slowly-varying currents are non-zero. The time-average is on-shore over all depths. The difference from case TW may be explained as differences between the two cases in mean circulation, in

particular the shape of the recirculation eddy south of Heceta Bank). The low-pass filtered term is generally off-shore and is similar to case TW.

4.5 Conclusions

Our model reproduces a California Undercurrent that is qualitatively consistent with observations and general understanding of its structure. Model experiments with passive tracer continuously released near the bottom at 300-m depth and analyses of cross-shore tracer transport confirm that tides contribute to cross-isobath dispersion of undercurrent waters and their on-shore transport. Additionally, more tracer is found near the surface in case TW than in case WO . Additional analyses are needed to understand if dissipation of the internal tide in the inner-shore region contributes to increased vertical turbulent flux of the tracer to the surface. Future analyses of dynamical mechanisms leading to asymmetry of onshore and offshore tidal transports, resulting in the net onshore transport due to the tidal motions, will require attention to the bottom boundary layer dynamics during the different phases of the tide.

4.6 Figures

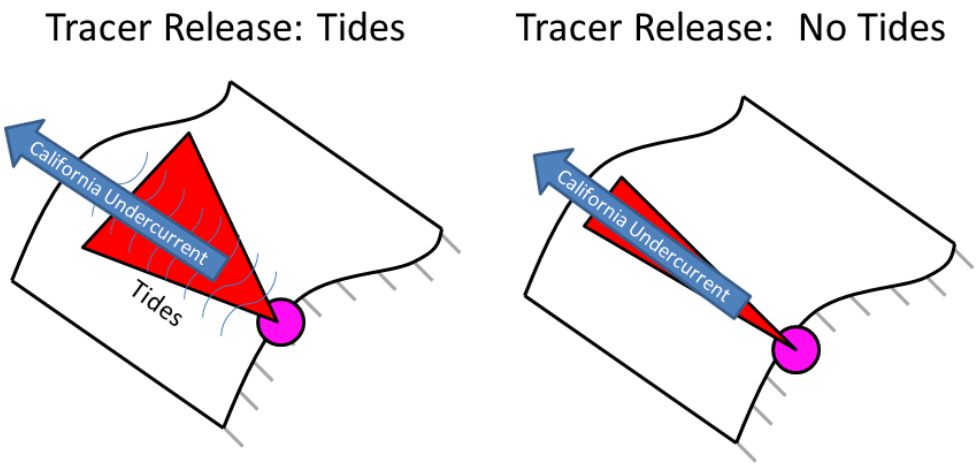

Fig. 4.1: Cartoon hypothesis of the passive tracer release experiment. Right: In the case with tides, tracer will be released at the sea floor on the upper slope and then be advected to the north by the California Undercurrent and also onto the shelf by tidal motions. Left: In the case without tides, tracer will again be advected to the north by the California Undercurrent, but less will move onto the shelf.

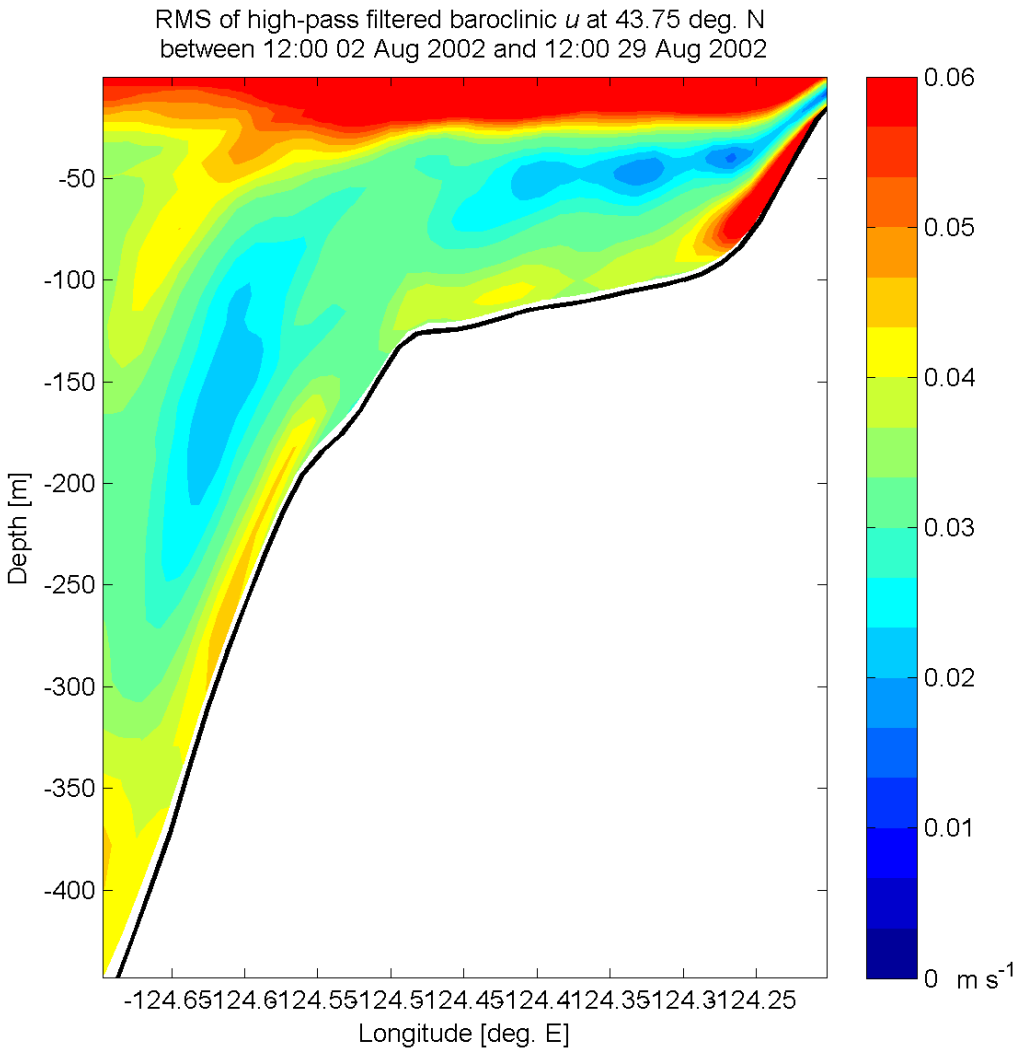

Fig. 4.2: Root-mean-square (with respect to time) of high-pass filtered, baroclinic u at 43.75°N between 12:00 UTC 2 Aug 2002 and 12:00 UTC 29 August 2002.

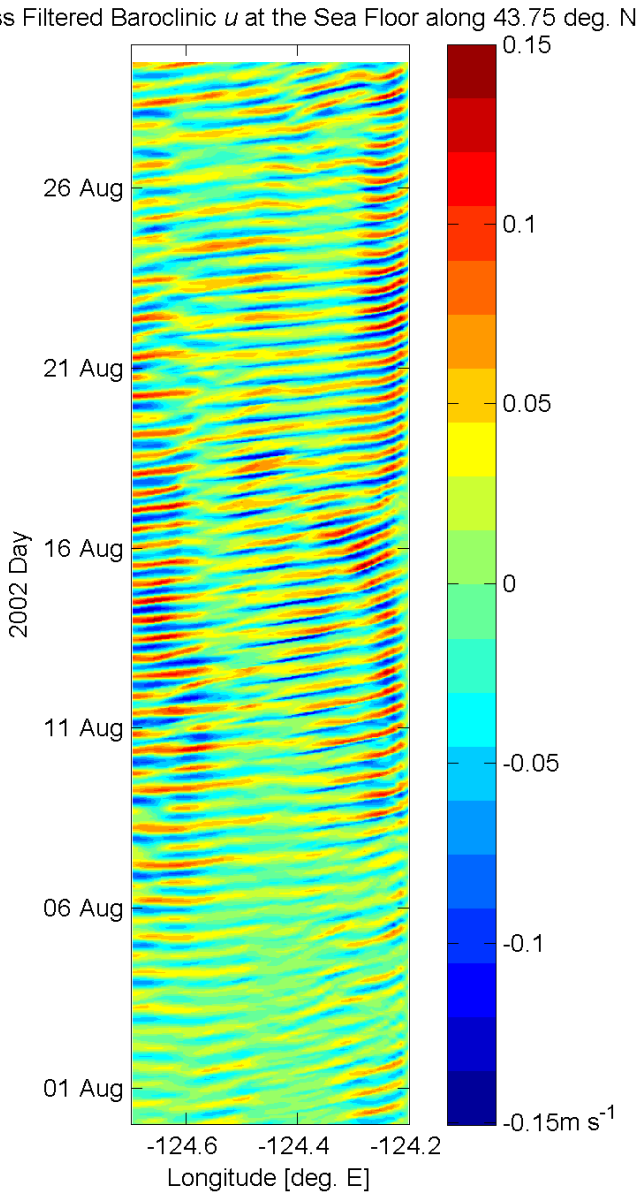

Fig. 4.3: High-pass filtered baroclinic u (i.e., u'_2) at the sea floor along 43.75°N from case TW.

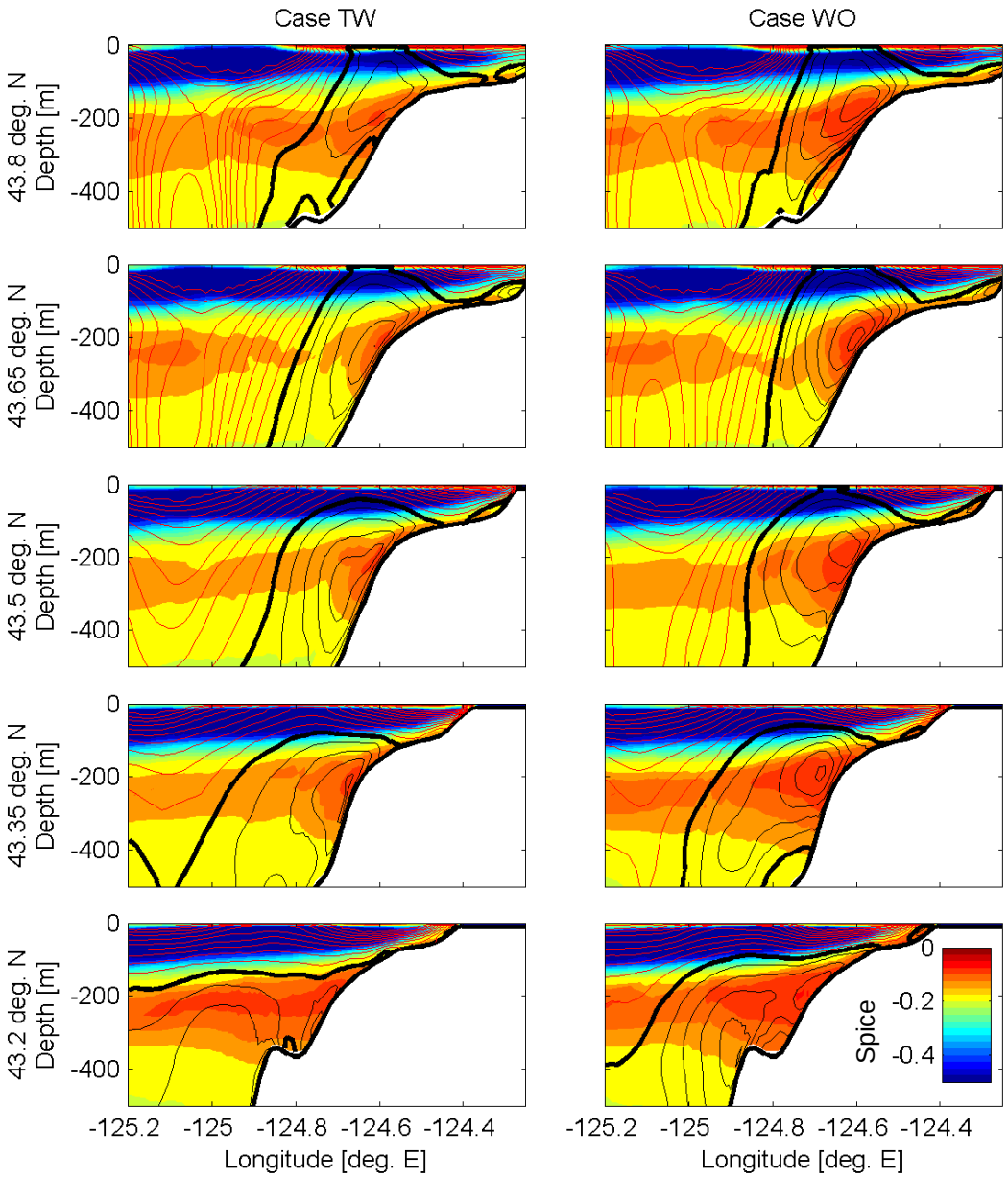

Fig. 4.4: August 2002-averaged spice (color) and meridional current (contours) for cases TWA (left) and WOA (right). Thick black contour marks 0-meriodional velocity, thin black lines northward velocity every 0.02 m/s and thin red lines southward velocity every -0.02 m/s. The CUC is clearly visibly in both spice and meridional velocity.

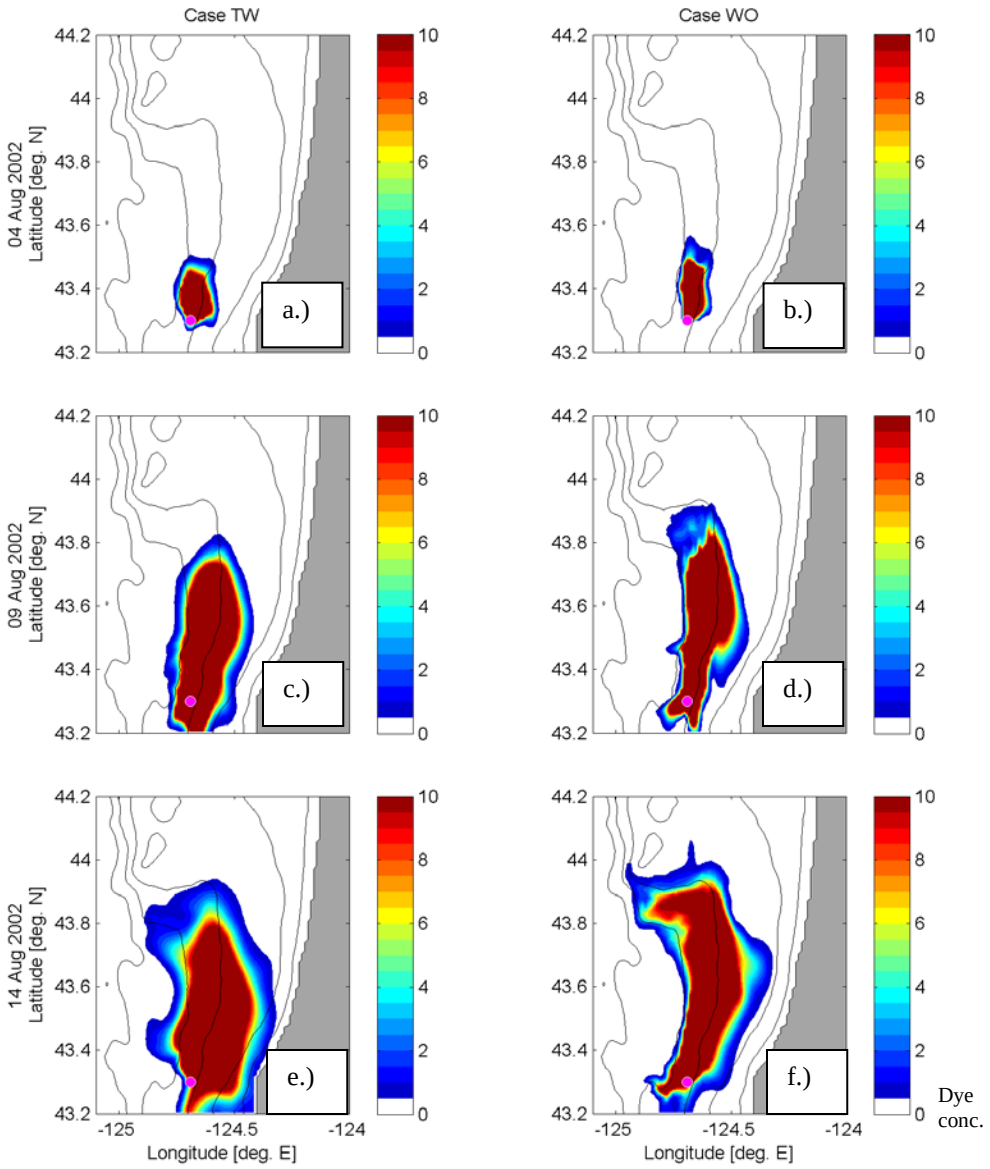

Fig. 4.5: Bottom tracer for cases TW (left) and WO (right) five days after release (top), 10 days (middle), and 15 days (bottom). Fields are daily-averaged to remove tidal and inertial variability. Black lines mark the 50-, 100-, 200-, 500-, and 1000-m isobaths. Magenta dot in each panel marks the tracer release point.

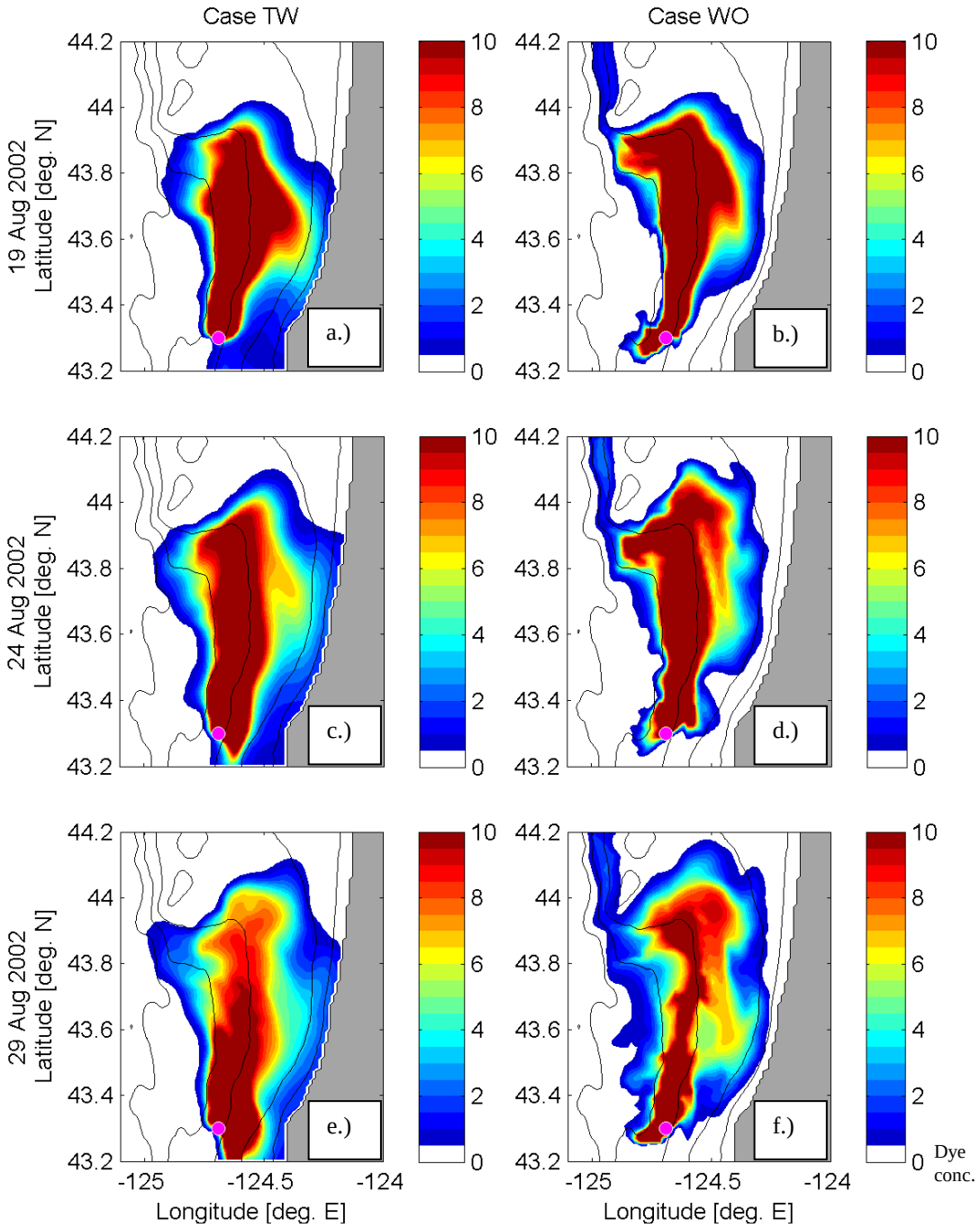

Fig. 4.6: Similar to Fig. 4.4. Bottom tracer for cases TW (left) and WO (right) 20 days after release (top), 25 days (middle), and 30 days (bottom). Fields are daily-averaged to remove tidal and inertial variability. Black lines mark the 50-, 100-, 200-, 500-, and 1000-m isobaths. Magenta dot in each panel marks the release point.

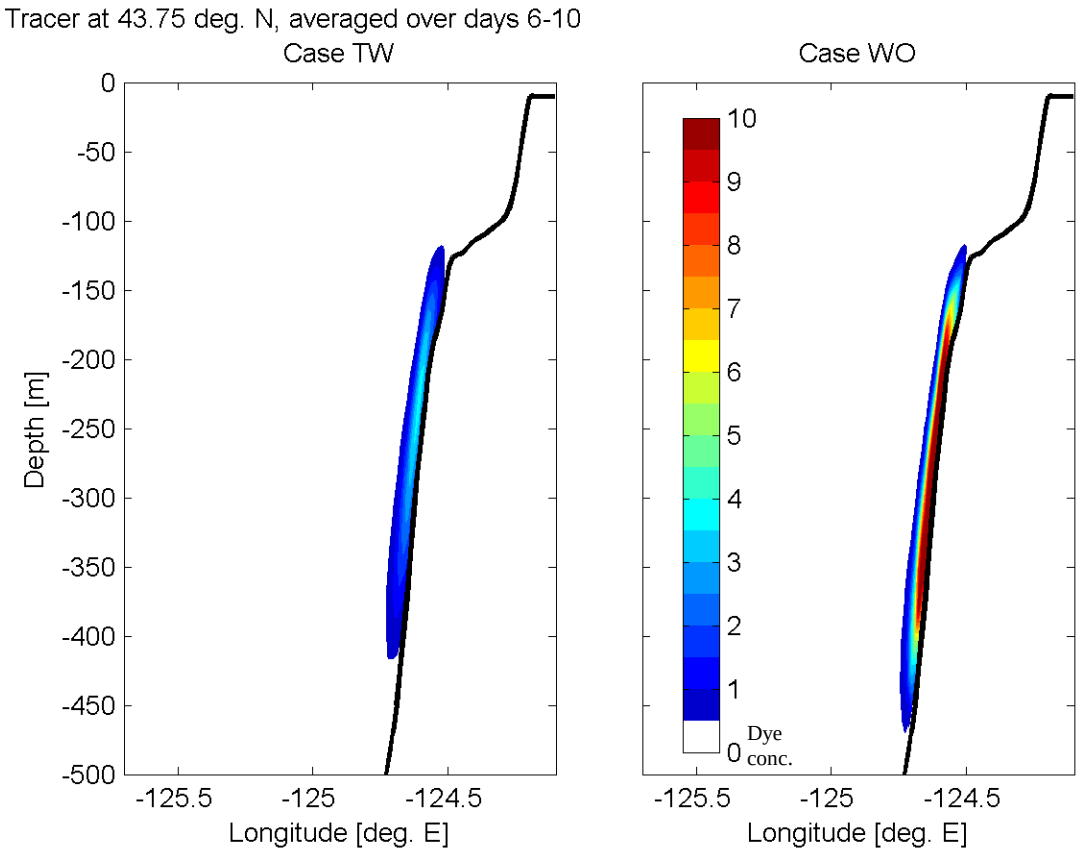

Fig. 4.7: Cross-section of tracer at 43.75°N averaged over days 6-10 of the release period (5-9 August 2002).

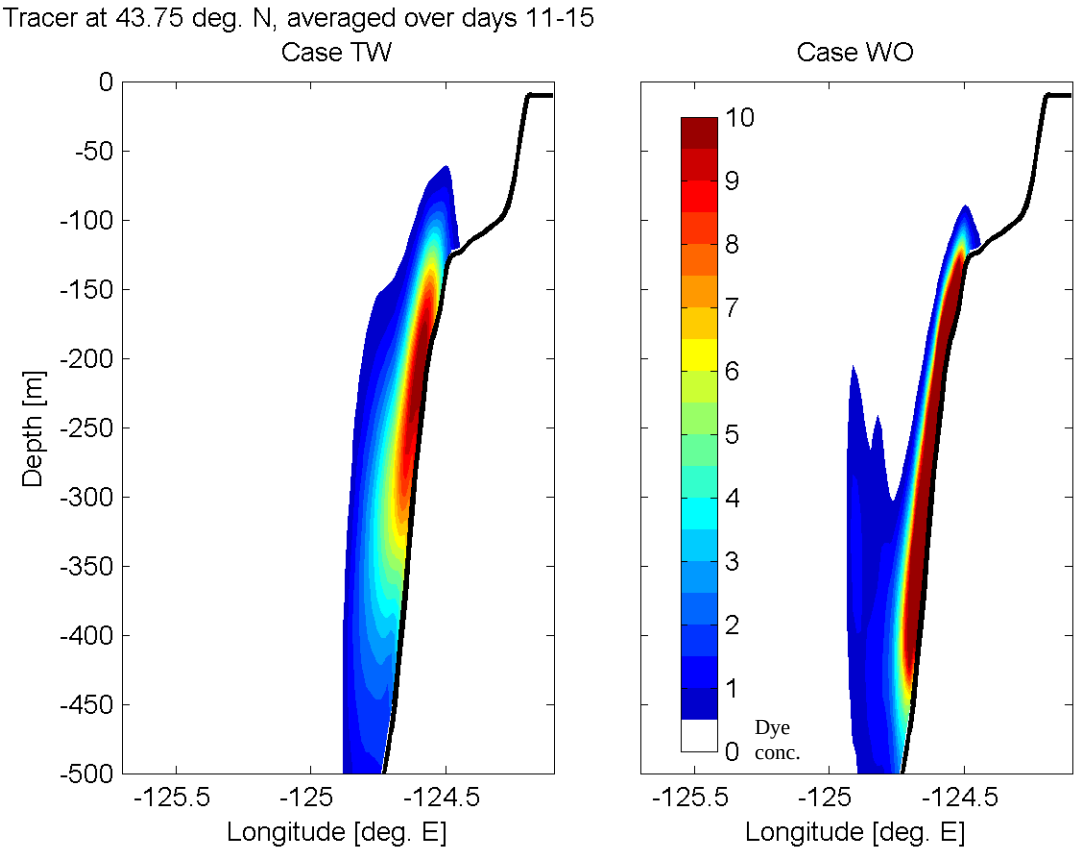

Fig. 4.8: As in Fig 4.6, cross-section of tracer at 43.75°N averaged over days 11-15 of the release period (10-14 August 2002).

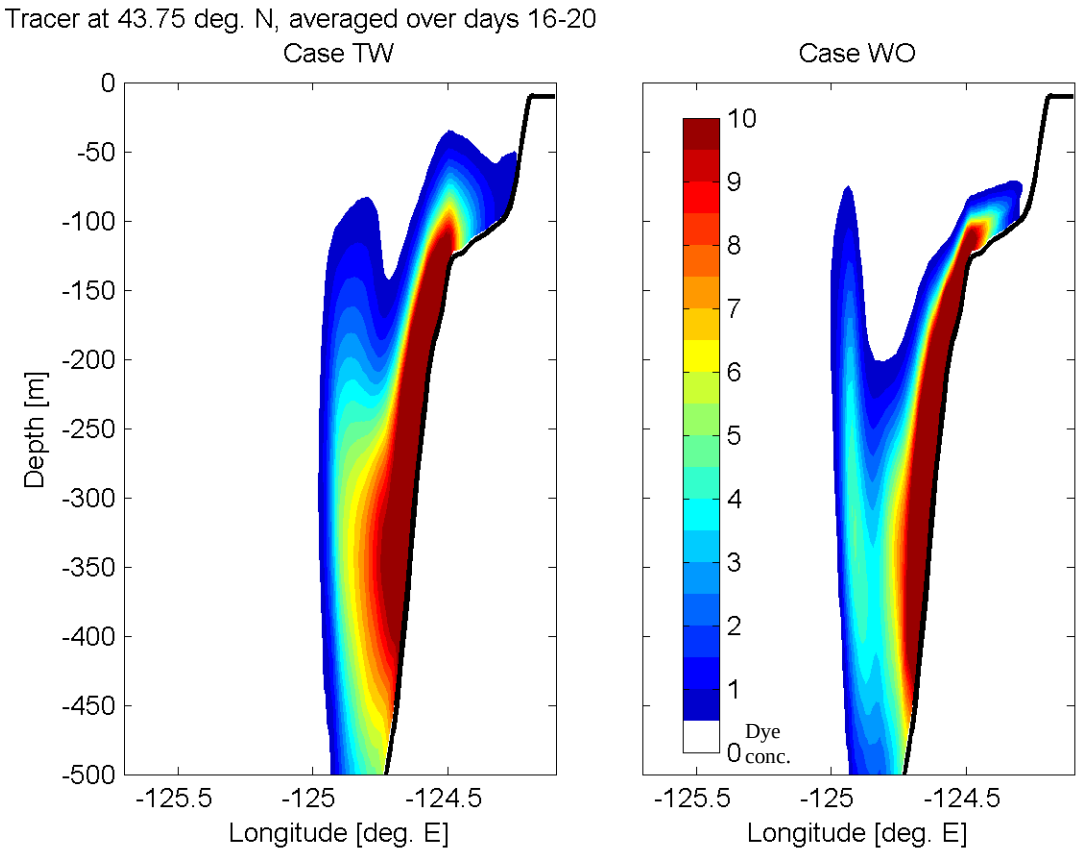

Fig. 4.9: As in Figs. 4.6 and 4.7, cross-section of tracer at 43.75°N averaged over days 16-20 of the release period (15-19 August 2002).

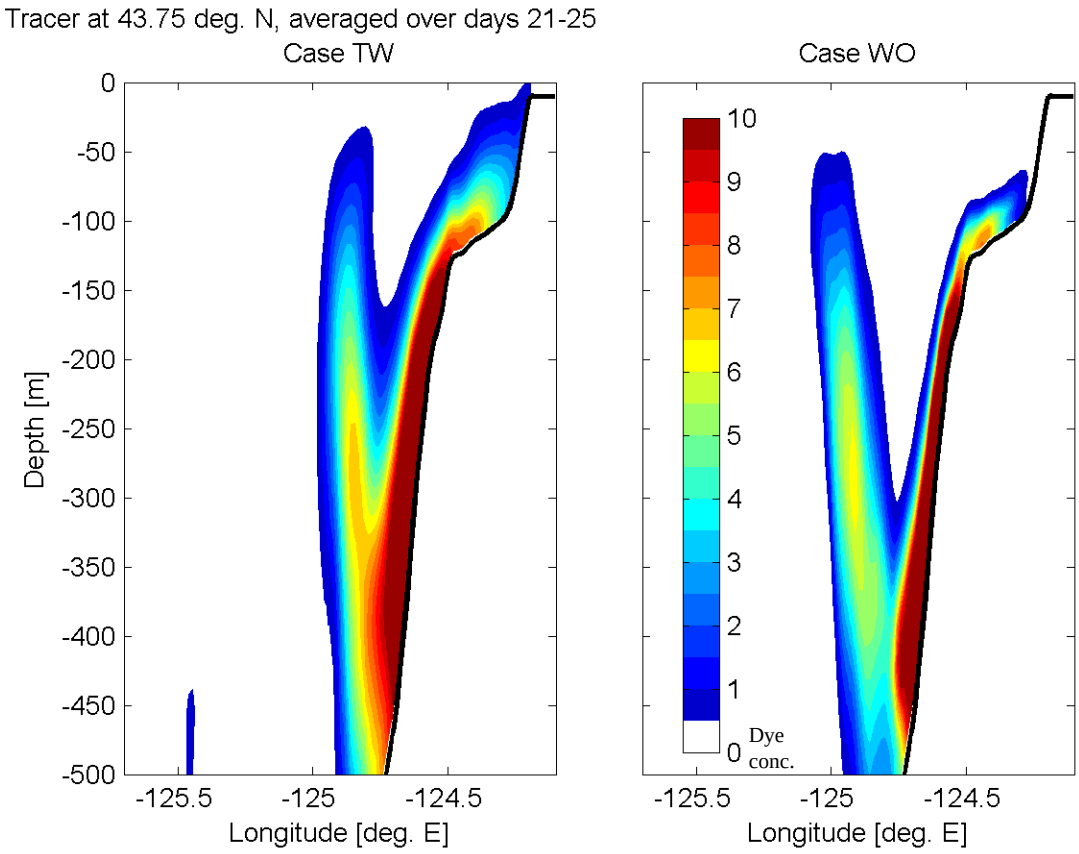

Fig. 4.10: As in Figs. 4.6-4.8, cross-section of tracer at 43.75°N averaged over days 21-25 of the release period (20-24 August 2002).

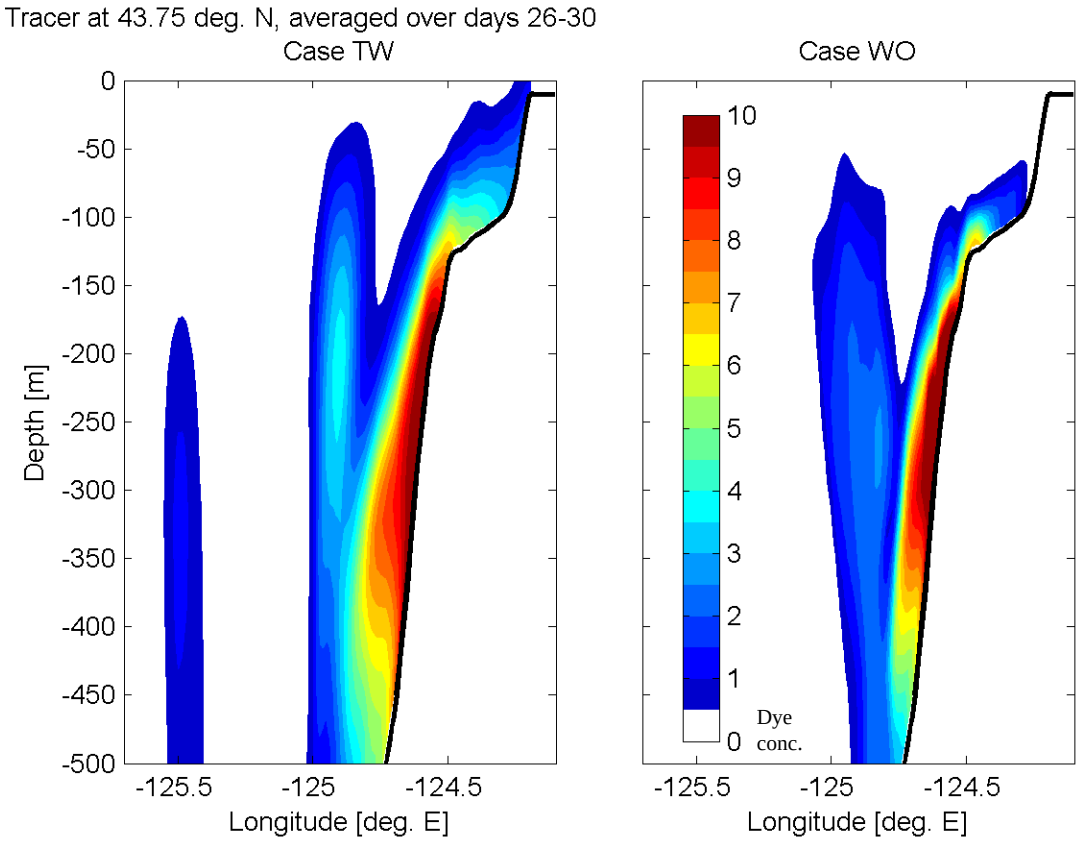

Fig. 4.11: As in Figs. 4.6-4.9, cross-section of tracer at 43.75°N averaged over days 26-30 of the release period (25-29 August 2002).

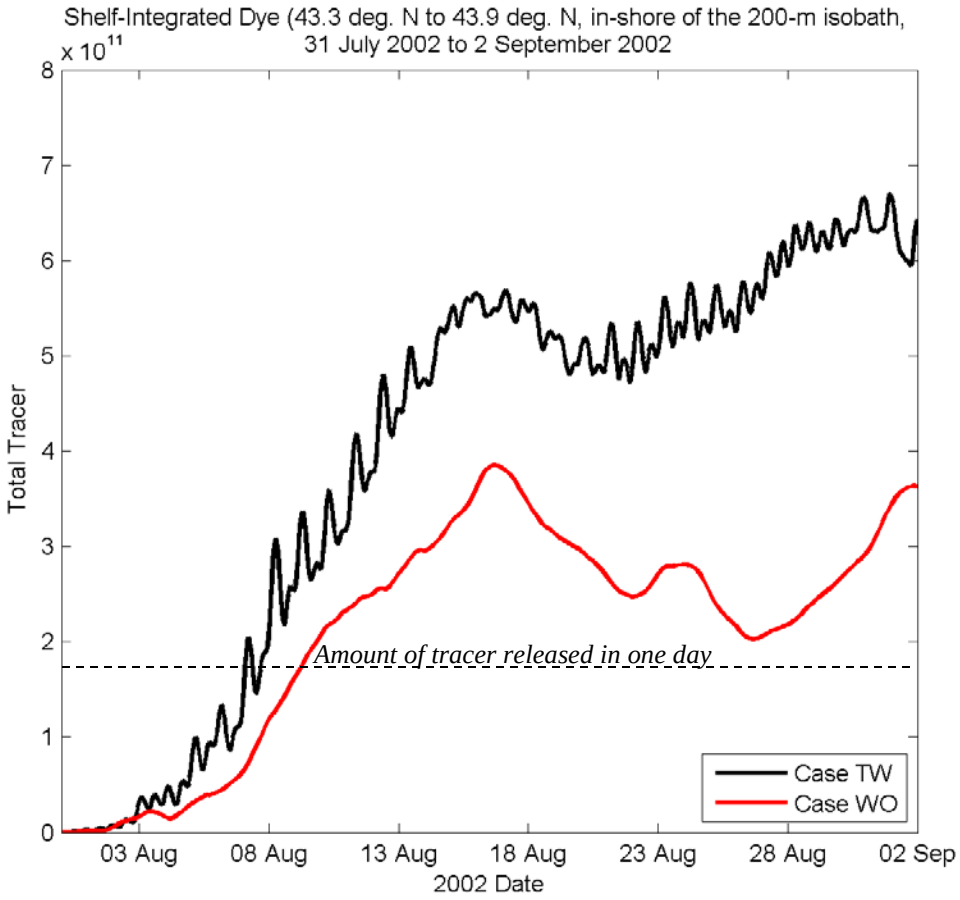

Fig. 4.12: Time series of volume-integrated tracer over the shelf area (200-m isobath to shore, sea floor to sea surface) between 43.3°N and 43.9°N during the tracer release period for cases TW (black) and WO (red). Tracer release begins at midnight on 31 July. The dashed horizontal black line represents the amount of tracer released in any one day.

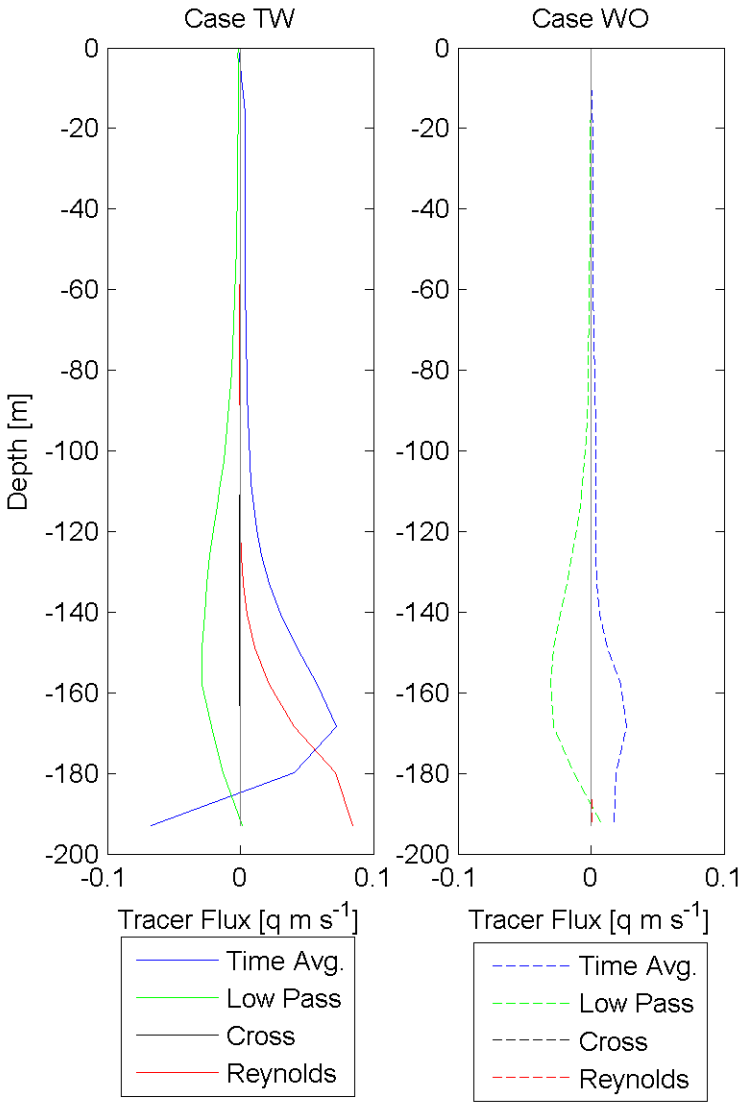

Fig 4.13: Tracer flux across the 200-m isobath (positive: on-shore, negative: off-shore) as a function of depth, averaged in time over August 2002 and averaged in space from 43.3°N to 43.9°N. Case TW is on the left and Case WO on the right. Tracer flux terms are decomposed into the time average (blue), low-pass (green), cross (black), and Reynolds (red) terms, as described in SECTION X. In both cases, the cross term averages to nearly zero at all depths. In case WO, the Reynolds term is also averages to nearly zero at all depths.

5. Conclusions

The work presented in this dissertation addresses interactions of tidal and sub inertial flow on the Oregon shelf during summer 2002. Its major findings are (1) that M2 internal tide generation on the slope is steady over the summer but that there is limited predictability of intra-shelf propagation of M2 baroclinic tidal energy and resulting internal tide currents; (2) that K1 and O1 diurnal tides intensify over the shelf (as previously predicted by Erofeeva et al. 2003), especially at capes, due to coastal trapped waves (Erofeeva et al. 2003) and cross-shelf advection of the coastal jet aliased into the tidal signal; and (3) internal tides significantly contribute to on-shelf flux of California Undercurrent waters at the bottom, particularly in a Reynolds-averaged sense.

As this work progressed, it included more physical forcing in the form of additional tidal constituents. Other physical forcing in the Oregon coastal ocean includes the Columbia River and high-frequency atmospheric forcing. The fresh water of the Columbia River is a buoyancy source and could impact internal tide dynamics, hence a possible extension to Chapter 2. High-frequency wind forcing was briefly examined in Chapter 3 and its effects are unclear. High-frequency variability in surface heat flux was not explored, and could possibly impact or interact with variability in the surface ocean driven by high-frequency winds. A coupled-ocean atmosphere model would be a better way to pursue such questions.

This work has several other possible extensions. One obvious possibility is how knowledge of internal tides in the deep ocean would quantitatively improve

numerical models of internal tides on the shelf. While the results of Kelly and Nash (2010) and Nash et al. (2012b) suggest the answer is no, it could help to reveal if there is variability at M2 internal tide generation sites on the Oregon slope. Such a study could also investigate internal tides at other frequencies, particularly S2 and N2. The latter has a 28-day beat period with the M2 constituent and has 20% of its strength, comparable to the modulation of the K1 tide by the P1 tide.

Biogeochemical models of the Oregon shelf have typically not included tides. Chapter 3 suggests that tides do alter subinertial surface circulation on the shelf, and Chapter 4 shows tides bring California Undercurrent waters onto the shelf. These combined effects may be significant for local marine ecosystems. What is unclear is whether tidal effects can be generally parameterized or if the specific spatio-temporal details of tidal circulation (e.g., near Cape Blanco) are critical.

Bibliography

Allen, J. S., P. A. Newberger, and J. Federiuk, 1995: Upwelling circulation on the Oregon continental shelf. Part I: Response to idealized forcing. Journal of Physical Oceanography, 25, 1843–1866.

Althaus, A. M., E. Kunze, and T. B. Sanford, 2003: Internal tide radiation from Mendocino Escarpment. J. Phys. Oceanogr., 33, 1510–1527.

Baines, P. G., 1982: On internal tide generation models. Deep-Sea Research, 29, 307–338.

Barth, J. A., S. D. Pierce, and R. L. Smith, 2000: A separating coastal upwelling jet at Cape Blanco, Oregon and its connection to the California Current System. Deep-Sea Research II, 47, 783–810.

Batchelder, H. P., et al., 2002: The GLOBEC Northeast Pacific California Current System program. Oceanography, 15, 36–47.

Beardsley, R. C., R. Limeburner, L. K. Rosenfeld, Introduction to CODE-2 moored array and large-scale data report, CODE-2: Moored Array and Large-Scale Data ReportL. Limeburner, Tech. Rep. 85-35, 1–21Woods Hole Oceanogr. Inst., Woods Hole, Mass., 1985a.

Bennett, A. F., 1992: Inverse methods in physical oceanography. Cambridge University Press.

Black, T. L., 1994: The new nmc mesoscale eta model: Description and forecast examples. Weather Forecasting, 9, 265–278.

Boyd, T., M. D. Levine, P. M. Kosro, S. R. Gard, and W. Waldorf, 2002: Observations from Moorings on the Oregon Continental Shelf, May - August 2001. Data Report 190, Oregon State University, College of Oceanic and Atmospheric Sciences, 104 Ocean Admin Bldg, Corvallis, OR 97331.

Brink, K. H., 1982: A comparison of long coastal trapped wave theory with observations off Peru. Journal of Physical Oceanography, 12, 897–913.

Cartwright, D. E., 1969: Extraordinary tidal currents near St. Kilda. Nature, 223, 928–932.

Castro, C. G., F. P. Chavez, and C. A. Collins, 2001: Role of the California Undercurrent in the export of denitrified waters from the eastern tropical North Pacific. Global Biogeochem. Cycles, 15, 819–830.

Chapman, D. C., 1983: On the influence of stratification and continental shelf and slope topography on the dispersion of subinertial coastally trapped waves. Journal of Physical Oceanography, 13, 1641–1652.

Chapman, D. C., 1985: Numerical treatment of cross-shelf open boundaries in an barotropic ocean model. Journal of Physical Oceanography, 15, 1060–1075.

Chavanne, C., P. Flament, D. Luther, and K.-W. Gurgel, 2010: The surface expression of semi-diurnal internal tides near a strong source at Hawai'i. Part II: interaction with mesoscale currents. Journal of Physical Oceanography, in press.

Chen, D., H. W. Ou, and C. Dong, 2003: A model study of internal tides in the coastal front zone. Journal of Physical Oceanography, 33, 170–187.

Collins, C. A., L. M. Ivanov, and O. V. Mel'nichenko, 2003: Seasonal variability of the California Undercurrent: Statistical analysis based on the trajectories of floats with neutral buoyancy. Phys. Oceanogr., 13, 135–147.

Crawford, W. R. and R. E. Thomson, 1982: Continental shelf waves of diurnal period along Vancouver Island. Journal of Geophysical Research, 87 (C12), 9516–9527.

Crawford, W. R. and R. E. Thomson, 1984: Diurnal-period continental shelf waves along Vancouver Island: A comparison of observation with theoretical models. Journal of Physical Oceanography, 14, 1629–1646.

Cummins, P. F., L. Y. Oey, Simulation of barotropic and baroclinic tides off Northern British Columbia, J. Phys. Oceanogr., 27, 762–781, 1997.

Cummins, P. F., D. Masson, and M. G. G. Foreman, 2000: Stratification and mean flow effects on diurnal tidal currents off Vancouver Island. Journal of Physical Oceanography, 30, 15–30.

Di Lorenzo, E. and Young, W. R. and Smith, S. L., 2006: Numerical and analytical estimates of M-2 tidal conversion at steep oceanic ridges. Journal of Physical Oceanography, 36 (6) 1072-1084, doi:10.1175/jpo2880.1.

Egbert, G. D. and R. D. Ray, 2000: Signicant dissipation of tidal energy in the deep ocean inferred from satellite altimeter data. Nature, 405: 775-778.

Egbert, G. D., A. F. Bennett, and M. G. G. Foreman, 1994: TOPEX/POSEIDON tides estimated using a global inverse model. Journal of Geophysical Research, 99 (C12), 24 821–24 852, doi:10.1029/94JC01894.

Egbert, G. D. and S. Y. Erofeeva, 2002: Efficient inverse modeling of barotropic ocean tides.Journal of Atmospheric and Oceanic Technology, 19 (2), 183–204.

Erofeeva, S. Y., G. D. Egbert, and P. M. Kosro, 2003: Tidal currents on the central Oregon shelf: Models, data and assimilation. Journal of Geophysical Research, 108, 3148, doi:10.1029/2002JC001615.

Geyer, W. R., 1993: Three-dimensioanl tidal flow around headlands. Journal of Geophysical Research, 98 (C1), 955–966.

Fairall, C. W., E. F. Bradley, J. S. Godfrey, G. A. Wick, J. B. Edson, and G. S. Young, 1996a: Cool-skin and warm-layer effects on sea surface temperature. Journal of Geophysical Research, 101 (C1), 1295–1308.

Fairall, C. W., E. F. Bradley, D. P. Rogers, J. B. Edson, and G. S. Young, 1996b: Bulk parameterization of air-sea fluxes for Tropical Ocean-Global Atmosphere Coupled-Ocean Atmosphere Response Experiment. Journal of Geophysical Research, 101 (C2), 3747.

Federiuk, J. and J. S. Allen, 1995: Upwelling circulation on the Oregon continetntal shelf. Part II: Simulations and comparisons with observations. Journal of Physical Oceanography, 25, 1867–1889.

Flament, P., A state variable for characterizing water masses and their diffusive stability: Spiciness, Prog. Oceanogr., 54, 493–501, 2002.

Flather, R. A., 1976: A tidal model of the north-west European continental shelf. Mem. Soc.R. Sci. Li`ege, 6, 141–164.

Galperin, B., L. H. Kantha, S. Hassid, and A. Rosati, 1988: A quasi-equilibirum turbulent energy model for geophysical flows. Journal of the Atmospheric Sciences, 45 (1), 55–62.

Garfield, N., C. A. Collins, R. G. Paquette, and E. Carter, 1999: Lagrangian exploration of the California Undercurrent, 1992–95. J. Phys. Oceanogr., 29, 560–583.

Garrett, C., P. MacCready, and P. Rhines, 1993: Boundary mixing and arrested Ekman layers: rotating stratified flow near a sloping boundary. Annu. Rev. Fluid Mech., 25: 291-323.

Hall, P. and A. M. Davies, 2007: Internal tide modelling and the influence of wind effects. Continental Shelf Research, 27 (9), 1357–1377.

Hayes, S. P. and D. Halpern, 1976: Observations of internal waves and coastal upwelling on the Oregon coast. Journal of Marine Research, 34, 247–267.

Hickey, B. M., 1979: The California Current System—Hypotheses and facts. Prog. Oceanogr., 8, 191–279.

Hickey, B. M., S. Geier, N. Kachel, S. R. Ramp, and P. M. Kosro, 2009: Seasonal water properties and velocity in the northern california current: Interannual variability and alongcoast structure. Limnology and Oceanpgraphy, in Preparation.

Hodur, R. M., 1997: The Naval Research Laboratory's Coupled Ocean/Atmosphere Mesoscale Prediction System (COAMPS). Monthly Weather Revuew, 125, 1414–1430.

Huyer, A. 1976. A comparison of upwelling events in two locations: Oregon and Northwest Africa. J. Marine Res., 34(4):531-546.

Jachec, S. M., O. B. Fringer, R. L. Street, and G. Margot G, 2007: Effects of grid resolution on the simulation of internal tides. International Journal of Offshore and Polar Engineering, 17 (2), 105–111.

Janjic, Z. I., 1994: The step-mountain eta coordinate model: Further developments of the convection, viscous sublayer, and tubulence closure schemes. Monthly Weather Review, 122, 927–945.

Kalnay, E., et al., 1996: The NCEP/NCAR 40-year reanalysis project. Bulletin of the American Meterological Society, 77 (3), 437–471.

Kim, S. and J. A. Barth, 2011: Connectivity and larval dispersal along the Oregon coast estimated by numerical simulations. Journal of Geophysical Research, 116, L06 002, doi:10.1029/2010JC006741.

Kelly, S. M. and J. D. Nash, 2010: Internaltide generation and destruction by shoaling internal tides. Geophysical Research Letters, 37, L23 611, doi:10.1029/2010GL045598.

Kim, S., R. M. Samelson, and C. Snyder, 2009. Ensemble-based estimates of the predictability of wind-driven coastal ocean flow over topography. Monthly Weather Review, 137, 2515-2537, DOI: 10.1175/2009MWR2631.1.

Koch, A. O., A. L. Kurapov, and J. S. Allen, 2010: Modeling analysis of a separated jet in the coastal transition zone off oregon. Journal of Geophysical Research, in Press.

Kosro, P. M., 2003: Enhanced southward ow over the oregon shelf in 2002: A conduit for subarctic water. Geophysical Research Letters, 30 (15), 8023, enhanced southward flow over the Oregon shelf in 2002: A conduit for subarctic water.

Kosro, P. M., 2005: On the spatial structure of coastal circulation off Newport, Oregon, during spring and summer 2001, in a region of varying shelf width. Journal of Geophysical Research, 110, C10S06, doi:10.1029/2004JC002769.

Kovalev, P. D. and A. B. Rabinovich, 1980: Bottom measurements of tidal currents in the southern part of the Kuril-Kamchatka trench. Oceanology, 20, 294–299.

Kundu, P. K., 1976: Ekman veering observed near the ocean bottom. Journal of Physical Oceanography, 6, 238–242.

Kurapov, A. L., J. S. Allen, and G. D. Egbert, 2010: Combined effects of wind-driven upwelling and internal tide on the continental shelf. Journal of Physical Oceanography, 40, 737–756.

Kurapov, A. L., J. S. Allen, G. D. Egbert, and R. N. Miller, 2005: Modeling bottom mixed layer variability on the mid-Oregon shelf during summer upwelling. Journal of Physical Oceanography, 35, 1629–1649.

Kurapov, A. L., G. D. Egbert, J. S. Allen, , R. N. Miller, S. Y. Erofeeva, and P. M. Kosro, 2003: The M2 internal tide off Oregon: Inferences from data assimilation. Journal of Physical Oceanography, 33, 1733–1757.

Kurapov, A. L., D. Foley, P. T. Strub, G. D. Egbert, and J. S. Allen, 2011: Variational assimilation of satellite observations in a coastal ocean model off Oregon. Journal of Geophysical Research, 116, C05 006, doi:10.1029/2010JC006909.

Kurian, J., F. Colas, X. Capet, J. C. McWilliams, and D. B. Chelton (2011), Eddy properties in the California Current System,J. Geophys. Res.,116,C08027, doi:10.1029/2010JC006895

Liu, W. T., 2002: Progress in scatterometer application. Journal of Oceanography, 58 (121-136).

Liu, K. K., and I. R. Kaplan, 1989: The eastern tropical Pacific as a source of 15N-enriched nitrate in seawater off southern California. Limnol. Oceanogr., 34, 820–830.

Liu, W. T. and X. Xie, 2001: Improvement in spacebased scatterometers and increased scientific impact in the past decade. Proc. Oceans 2001, Honolulu, HI, Marine Technology Society, Vol. 1, 626–630.

Llewellyn Smith, Stefan G., W. R. Young, 2002: Conversion of the Barotropic Tide. J. Phys. Oceanogr., 32, 1554–1566.

Llewellyn Smith, S. G. & Young, W. R. 2003 Tidal conversion at a very steep ridge. J. Fluid Mech., 495, 175-191, doi:10.1017/S0022112003006098.

M. Xue, M., K. K. Droegemeier, V. Wong, A. Shapiro, and K. Brewster, 1995: ARPS Version 4.0 users guide. University of Oklahoma, Norman, OR 73072, Center for Analysis and Prediction of Storms.

MacFadyen, A., B.M. Hickey, andW. Cochlan, 2008: Influences of the Juan de Fuca Eddy on circulation, nutrients, and phytoplankton production in the northern California Current System. J. Geophys. Res., 113, C08008, doi:10.1029/2007JC004412.

Marchesiello, P., J. C. McWilliams, and A. Shchepetkin, 2001: Open boundary conditions for long-term integration of regional oceanic models. Ocean Modelling, 3, 1–20.

Marchesiello, P., J. C. McWilliams, and A. Shchepetkin, 2003: Equilibrium structure and dynamics of the California Current System. J. Phys. Oceanogr., 33, 753–783.

Martini, K., M. H. Alford, E. Kunze, S. M. Kelly, and J. D. Nash, 2011: Observations of internal tides on the Oregon continental slope. J. Phys. Oceanogr., 41, 1772–1794.

Maturi, E., A. Harris, C. Merchant, J. Mittaz, B. Potash, W. Meng, and J. Sapper, 2008: NOAA's sea surface temperature products from operational geostationary satellites. Bulletin of the American Meteorological Society, 89 (12), 1877–1888.

McCabe, R. M., P. MacCready, and G. Pawlak, 2006: Form drag due to flow separation at a headland. Journal of Physical Oceanography, 36, 2136–2152.

McCreary, J. P., 1981. A linear stratified model of the coastal undercurrent Phiios. Trans. R. Soc. London Ser. A, 302, 385--413.

Mellor, G. L. and T. Yamada, 1982: Development of a turbulence closure model for geophysical fluid problems. Reviews of Geophysics and Space Physics, 20 (4), 851–875.

Merrifield, M. A., and P. E. Holloway, 2002: Model estimates of m2 internal tide energetics at the Hawaiian Ridge. J. Geophys. Res.,107, 3179, doi:10.1029/2001JC000996.

Mittelstadt, J., 1998: The eta-32 mode. Technical Attachment 98-03, National Weather Service Western Region Headquarters. Available online at http://www.wrh.noaa.gov/wrh/98TAs/9803/.

Mooers, C. N. K., 1970: The interaction of an interal tide with the frontal zone of a coastal upwelling region. Ph.D. thesis, Oregon State University.

Mooers, C. N. K., 1975a: Several effects of a baroclinic current on the cross-stream propagation of inertial-internal waves. Geophysical and Astrophysical Fluid Dynamics, 6, 245–275.

Mooers, C. N. K., 1975b: Several effects of a baroclinic currents on the three-dimensional propagation of inertial-internal waves. Geophysical and Astrophysical Fluid Dynamics, 6, 277–284.

Munk, W. H., and C. Wunsch, 1998: Abyssal recipes II: Energetics of tidal and wind mixing. Deep-Sea Res, 45, 1977–2010.

Nash, J. D., S. M. Kelly, E. L. Shroyer, J. M. Moum, and T. F. Duda (2012), The unpredictable nature of internal tides on continental shelves, J. Phys. Oceanogr., 42, 1981–2000, doi:10.1175/JPO-D-12-028.1.

Nash, J., E. Shroyer, S. Kelly, M. Inall, T. Duda, M. Levine, N. Jones, and R. Musgrave, 2012a: Are any coastal internal tides predictable? Oceanography, 25 (2), 80{95, doi:10.5670/oceanog.2012.44.

Niwa, Y., and T. Hibiya (2001), Numerical study of the spatial distribution of the M2 internal tide in the Pacific Ocean, J. Geophys. Res., 106, 22,441–22,449.

NOAA, 1988: Data Announcement 88-MGG-02, Digital relief of the Surface of the Earth. Tech. rep., National Geophysical Data Center, Boulder, Colorado.

Odamaki, M., 1994: Tides and tidal currents along the Okhotsk coast of Hokkaido. J. Oceanogr., 50, 265–279.

Oke, P. R., J. S. Allen, R. N. Miller, and G. D. Egbert, 2002a: A modeling study of the three-dimensional continental shelf circulation off Oregon. Part II: Dynamical analysis. Journal of Physical Oceanography, 32, 1383–1403.

Oke, P. R., et al., 2002b: A modeling study of the three-dimensional continental shelf circulation off Oregon. Part I: Model-data comparisons. Journal of Physical Oceanography, 32, 1360–1382.

O'Keefe, S., 2005: Observing the coastal ocean with HF radar. M.S. thesis, Oregon State University.

Oliger, J. and A. Sundstrom, 1978: Theoretical and practical aspects of some initial boundary value problems in fluid dymaics. SIAM J. Appl. Math., 35, 419–446.

Osborne, J. J., A. L. Kurapov, G. D. Egbert, and P. M. Kosro, 2011: Spatial and temporal variability of the m2 internal tide generation and propagation on the Oregon shelf. J. of Phys. Oceanogr., 2037–2062, doi:10.1175/JPO-D-11-02.1.

Osborne, J. J., A. L. Kurapov, G. D. Egbert, and P. M. Kosro, 2014: Intensified diurnal tides on the Oregon shelf. J. of Phys. Oceanogr., in press.

Park, J.-H. and D. R. Watts, 2006: Internal tides in the southwestern Japan/East Sea. Journal of Physical Oceanography, 36, 22–34.

Pawlowicz, R., B. Beardsley, and S. Lentz, 2002: Classical tidal harmonic analysis including error estimates in MATLAB using T TIDE. Computers and Geosciences, 28 (8), 929–937.

Pearson, K., 1905: The problem of the random walk. Nature, 72, 294.

Pereira, A. F., B. M. Castro, L. Calado, , and I. C. A. da Silveira, 2007: Numerical simulation of M2 internal tides in the South Brazil Bight and their interaction with the Brazil Current. Journal of Geophysical Research, 112, C04 009, doi:10.1029/2006JC003673.

Perlin, N., R. M. Samelson, and D. B. Chelton, 2004: Scatterometer and model wind and wind stress in the northern california coastal zone. Monthly Weather Review, 132, 2110–2129.

Petruncio, E. T., L. K. Rosenfeld, and J. D. Paduan (1998), Observations of the internal tide in Monterey Canyon, J. Phys. Oceanogr., 28, 1873–1903.

Pierce, S. D., R. L. Smith, P. M. Kosro, J. A. Barth, and C. D. Wilson, 2000: Continuity of the poleward undercurrent along the eastern boundary of the mid-latitude North Pacific. Deep-Sea Res., 47, 811–829

Pugh, D. T., 1987: Tides, Surges and Mean Sea-Level. John Wiley & Sons Ltd, New York.

Rabinovich, A. B. and R. E. Thomson, 2001: Evidence of diurnal shelf waves in satellite tracked drifter trajectories off the Kuril Islands. J. Phys. Oceanogr., 31, 2650–2668.

Rabinovich, A. B. and A. E. Zhukov, 1984: Tidal oscillations on the shelf of Sakhalin Island. Oceanology, 24, 184–189.

Ramp, S. R. and F. L. Bahr, 2008: Seasonal evolution of the upwelling process south of Cape Blanco. Journal of Physical Oceanography, 38, 3–28.

Samelson, R., et al., 2002: Wind stress forcing of the Oregon coastal ocean during the 1999 upwelling season. Journal of Geophysical Research, 107 (C5), 3034, doi:10.1029/2001JC000900.

Saraceno, M., P. T. Strub, and P. M. Kosro, 2008: Estimates of sea surface height and near surface alongshore coastal currents from combinations of altimeters and tide gauges. Journal of Geophysical Research, 113, C11 013, doi:10.1029/2008JC004756.

Shchepetkin, A. F. and J. C. McWilliams, 2005: The regional oceanic modeling systems (ROMS): a split-explicit, free-surface, topography-following-coordinate oceanic model. Ocean Modelling, 9, 347–404, doi: 10.1016/j.ocemod.2004.08.002.

Signell, R. P. and W. R. Geyer, 1991: Transient eddy formation around headlands. Journal of Geophysical Research, 96 (C2), 2561–2575.

Simmons, H. L., R. W. Hallberg, and B. K. Arbic (2004b), Internal wave generation in a global baroclinic tide model, Deep Sea Res., Part II, 51, 3043–3068.

Smith R.L., 1981) in Coastal Upwelling, A comparison of the structure and variability of the flow fields in three coastal upwelling regions: Oregon, Northwest Africa, and Peru, American Geophysical Union, ed Richards A. E. pp 107–118.

Smith, R. L., A. Huyer, and J. Fleischbein, 2001: The coastal ocean off Oregon from 1961 to 2000: is there evidence of climate change or only of Los Ninos? Progress in Oceanography, 49, 63–93.

Smolarkiewicz, P. K., 1983: A simple positive definite advection scheme with small implicit diffusion, Mon. Wea. Rev. 111, 479.

Smolarkiewicz, P. K., 1984: A fully multidimensional positive definite advection transport algorithm with small implicit diffusion, J. Comput. Phys. 54, 325.

Smolarkiewicz, P. K., 1998: MPDATA: a finite-difference solver for geophysical flows, J. Comput. Phys. 150, 459-480.

Springer, S. R., R. M. Samelson, J. S. Allen, G. D. Egbert, A. L. Kurapov, R. N. Miller, and J. C. Kindle, 2009: A nested grid model of the Oregon Coastal Transition Zone: Simulations and comparisons with obeservations during the 2001 upwelling season. Journal of Geophysical Research, 114, CO2010, doi:10.1029/2008JC004863.

St. Laurent, L., S. Stringer, C. Garrett, and D. Perrault-Joncas, 2003: The generation of internal tides at abrupt topography. Deep-Sea Res, 50, 987–1003.

Staudenmaier, M., 1996: A description of the meso eta model. Technical Attachment 96-06, National Weather Service Western Region Headquarters. Available online at http://www.wrh.noaa.gov/wrh/96TAs/TA9606/ta96-06.html.

Strub, P. T., P. M. Kosro, A. Huyer, and C. Collaborators, 1991: The nature of the cold filaments in the California Current Syste,. Journal of Geophysical Research, 96(C8), 14743–14768, doi:10.1029/91JC01024.

Suanda, S., J. A. Barth, R. A. Holman, and J. Stanley, 2014: Shore-based video observations of nonlinear internal waves across the inner shelf. Journal of Oceanic and Atmospheric Technology.

Swartzman, G., B. Hickey, P. M. Kosro, and C. Wilson, 2005: Poleward and equatorward currents in the Pacific eastern boundary current in summer 1995 and 1998 and their relationship to the distribution of euphausiids. Deep-Sea Res. II, 52, 73–88.

Thomson, R. E., and M. V. Krassovski, 2010: Poleward reach of the California Undercurrent extension. J. Geophys. Res., 115, C09027, doi:10.1029/2010JC006280.

Torgrimson, G. M. and B. M. Hickey, 1979: Barotropic and baroclinic tides over the continental slope and shelf off oregon. Journal of Physical Oceanography, 9 (5), 946–961.

Wunsch, C. H., 1975: Internal tides in the ocean. Reviews of Geophysics and Space Physics, 13, 167–182.

Xing, J. and A. M. Davies, 1997: The influence of wind effects upon internal tides in shelf edge regions. Journal of Physical Oceanography, 27, 2100–2125.

Xing, J. and A. M. Davies, 1998: Influence of stratification upon diurnal tidal currents in shelf edge regions. Journal of Physical Oceanography, 28, 1803–1831.

Xing, J. and A. M. Davies, 2005: Influence of a cold water bottom dome on internal wave trapping. Geophysical Research Letters, 32 (L03601), doi:10.1029/2004GL021833.

Yefimov, V. V. and A. B. Rabinovich, 1980: Resonant tidal currents and their relation to continental shelf waves of the northwestern Pacific Ocean. Izv., Atmos. Oceanic Phys., 16, 805–812.